Multiscale simulation of phase transformation in metals

Tobias Willerding

Multiscale simulation
of phase transformation
in metals

von

Tobias Emanuel Willerding

Multiscale simulation
of phase transformation
in metals

vorgelegt von

Tobias Emanuel Willerding

aus Bonn

Kurzfassung

Diese Arbeit beschäftigt sich mit der Mehrskalensimulation von Phasentransformation in Metallen. Mehrskalensimulation ist die gleichzeitige Verwendung von zwei oder mehr Methoden in einer Simulation, um Effekte verschiedener Größenskalen in Zeit oder Raum in einer Rechnung zu berücksichtigen.

Die Phasentransformation zwischen verschiedenen Gitterstrukturen spielt eine große Rolle in der Herstellung von Metallen, z.B. Eisen. In dieser Arbeit wird eine Mehrskalenmethode entwickelt, um Phasentransformation in Metallen zu simulieren. Kontinuumsmechanik, diskretisiert durch die Finite Elemente (FE)-Methode wird gekoppelt mit Atomistik, repräsentiert durch die Molekulardynamik (MD).

Die Zielsetzung der Arbeit ist es, Phasentransformation zwischen kubisch-raumzentrierter sowie kubisch-flächenzentrierter Struktur und hexagonal dichtester Packung zu simulieren. Da Phasentransformation eine Änderung der internen Gitterstruktur erfordert, sind traditionelle Mehrskalensimulationsmethoden nicht geeignet. Diese setzen meistens eine feste Kopplung am Interface zwischen Fein- und Grobskala voraus. Außerdem wird häufig die Cauchy-Regel benutzt, die keine interne Umstrukturierung/Topologieänderung zulässt.

Um diese Probleme zu lösen, wird eine neue kombinierte hierarchic-partitioned-domain Methode vorgeschlagen, die aus zwei Teilen besteht. Auf der Ebene der finiten Elemente wird eine Methode basierend auf der FE²-Methode von FEYEL (2003) vorgeschlagen, die Molekulardynamiksimulationen als Unterprobleme benutzt, je ein Unterproblem pro Gaußintegrationspunkt. Die Methode ist ähnlich der Methode von ULZ (2015), allerdings gibt es ein paar Unterschiede: im Gegensatz zu Ulz wird kein Kernel für die Mittelung der Spannungen auf der Feinskala verwendet. Des Weiteren wird nichtlineare Dynamik verwendet, um zu einer quasistatischen Lösung zu konvergieren, Ulz benutzt nichtlineare Statik. In der expliziten Dynamik reichen die internen Knotenkräfte der finiten Elemente für die Beschreibung der Verformung aus. Diese können deutlich einfacher berechnet werden als die Steifigkeitsmatrix, die in der Statik erforderlich ist. Da die Molekulardynamikunterprobleme das Materialgesetz der finiten Elemente liefern, ist das Materialverhalten der finiten Elemente identisch zu dem der Molekulardynamik und damit können die finite Elemente die Phasentransformation abbilden. Diese hierarchische Kopplung wird in dieser Arbeit auch vertikale Kopplung genannt.

Für den partitioned-domain Teil der Methode wird das Rechengebiet in zwei Teile aufgeteilt, einen Teil mit Molekulardynamik und einen Teil mit finiten Elementen. Diese Aufteilung wird auch horizontale Kopplung in dieser Arbeit genannt. Die Kopplung am Interface zwischen den beiden Gebieten wird auf zwei unterschiedliche Weisen erreicht. Eine Methode ist ähnlich zu der AtC-Methode von FISH ET AL. (2007), wo die Cauchy-Regel benutzt wird, um die Kopplungsatome an die Bewegung der FE-Knoten zu binden. Die zweite Methode ist neu und beinhaltet, dass die Kopplungsatome sich in einer Box mit periodischen Randbedingungen frei bewegen können. Diese Box hat die Form eines

Parallelepipeds und deformiert sich wie das finite Element. Da die Deformation des finiten Elements beliebig ist, kann nur ein Parallelepiped berechnet werden, welches der Form des finiten Elementes möglichst nahe kommt. Die Kraft, die auf die gebundenen Atome wirkt, wird in beiden Methoden mit modifizierten Formfunktionen auf die FE-Knoten umverteilt. Dabei soll sichergestellt werden, dass die Kraft nur auf diejenigen Knoten wirkt, die auch am Interface zwischen FE & MD liegen.

Im Rahmen dieser Arbeit wird ein Molekulardynamikcode programmiert, der in den bestehenden FE-Löser NumPro, der am Institut für Baustatik und Baudynamik (IBB) der Universität Stuttgart entwickelt wird, eingebettet ist.

Zur Validierung der Methode werden vier Testfälle präsentiert, um die Mehrskalenmethode zu validieren. Ein Zugversuch und ein Biegeversuch werden simuliert, um die prinzipielle Funktionalität der Methode zu verifizieren. Dazu wird zuerst eine Referenzlösung mit Molekulardynamik ausgerechnet. Das Potential von MENDELEV ET AL. (2003) wird für die Berechnung ausgewählt. Unglücklicherweise war es nicht möglich die gewünschten Randbedingungen in einem externen Programm für Molekulardynamiksimulationen (IMD) aufzubringen und zu einer quasi-statischen Lösung zu konvergieren. Daher wird die horizontale Kopplung benutzt, um die Randbedingungen mittels finiten Elementen aufzubringen. Der Zugversuch zeigt gute Resultate und ist in guter Übereinstimmung mit der Molekulardynamiklösung. Der Biegeversuch ist komplexer und liefert durchwachsene Ergebnisse. Die Molekulardynamikverschiebung am Balkenende ist am größten und die FE-Lösung mit der vertikalen Kopplung die steifste. Die horizontalen Kopplungsmethoden liegen dazwischen. Die Resultate weichen von der MD-Lösung um bis zu 35% ab.

Um die Fähigkeit der Methode, Phasentransformation zu simulieren, zu validieren, werden zwei unterschiedliche Testfälle durchgeführt. Der erste Testfall ist für die vertikale Kopplung und der zweite Testfall für sowohl vertikale als auch horizontale Kopplung. Für die Phasentransformation werden zwei Potentiale, basierend auf der Embedded-Atom-Methode (EAM) benutzt. Für die Simulation von Phasentransformation zwischen kubisch-raumzentriertem (BCC) und kubisch-flächenzentriertem (FCC) Eisen wird das Potential von MEYER AND ENTEL (1998) benutzt, da es eines der wenigen EAM-Potentiale ist, das den Phasenübergang in Eisen abbilden kann. Darüber hinaus wird das Potential von MENDELEV ET AL. (2016) benutzt, um den Phasenwechsel in Titan zwischen der hexagonal dichtesten Packung (HCP) und der kubisch-raumzentriertem Packung (BCC) zu simulieren. Für jede Kopplungsmethode werden alle vier Phasenänderungen (BCC↔ FCC und HCP↔ BCC) simuliert. Der erste Testfall, der nur vertikales Koppeln beinhaltet, zeigt bei allen Phasentransformationen sehr gute Ergebnisse. Die Atome in den MD-Unterproblemen an den Integrationspunkten verformen sich wie erwartet und die Deformation der finiten Elemente ist ebenfalls gut, was durch das Längenverhältnis der Kantenlängen des Simulationsquaders vor und nach der Simulation validiert wird.

Im Falle der kombinierten horizontalen und vertikalen Kopplung werden ebenfalls alle vier Phasentransformationen simuliert. Im Fall des Wechsels von BCC↔ FCC zeigt die

Kopplung mit der Cauchy-Regel ebenfalls sehr gute Resultate, da diese Phasentransformation nur eine Skalierung der Achsen beinhaltet. Die vorgeschlagene Methode mit der Box mit periodischen Randbedingungen liefert ebenbürtige Ergebnisse zu der Cauchy-Regel. Im Falle des Phasenübergangs HCP$\leftrightarrow$ BCC sieht die Sache jedoch anders aus. Die neue Methode liefert deutlich bessere Ergebnisse als die Cauchy-Regel, da bei der Cauchy-Regel die Atome ihre Position relativ zueinander nicht ändern können.

Abstract

This thesis is about multiscale simulation of phase transformation in metals. Multiscale simulation is the simultaneous use of two or more models in order to have phenomena of different length or time scale in one simulation.

Phase transformation between different lattice structures plays an important role in the formation of metals, e.g. iron or titanium. It is, therefore, of interest to simulate phase transformation in a multiscale context. In this thesis, a multiscale method for the simulation of phase transformation in metals is developed. Continuum mechanics, represented by the finite element method, is coupled with atomistics, represented by molecular dynamics.

The goal is to simulate phase transformation in metals between different lattice structures such as body-centered cubic, face-centered cubic and hexagonal close-packed structure. As phase transformation requires an internal restructuring of the molecular structure, traditional multiscale methods cannot be used as these require fixed coupling at the interface between coarse scale and fine scale and very often also in the coarse scale by using the Cauchy rule.

In order to overcome these problems, a combined hierarchic-partitioned-domain method is proposed that consists of two parts. On the finite element level, a hierarchic method based on the FE^2-method by FEYEL (2003) is used with molecular dynamics simulations as subproblems, one subproblem at each Gauss integration point. It is similar to the method by ULZ (2015), but with a few differences. In contrast to Ulz, no kernel is used for averaging the stress values at the fine scale and a quasi-static solution is calculated by using non-linear dynamics instead of statics. In explicit dynamics, only the internal nodal forces are necessary for the simulation, which can be calculated much easier than the stiffness matrices of finite elements. With molecular dynamics as material law for the finite elements, the finite elements behave in the same way as atoms for coarse scale deformations. Using this method phase transformation can already be simulated in the coarse scale as small molecular dynamics subproblems are sufficient for phase transformation simulation. This is the hierarchic part of the method and it is denoted as vertical coupling.

The partitioned-domain part of the method consists of dividing the domain into two parts: a molecular dynamics part and a finite element part. This is also denoted as horizontal coupling in this work. The coupling of finite elements and molecular dynamics at the interface is done in two ways. First with a method similar to the AtC-method by FISH ET AL. (2007) using the Cauchy rule, where a part of the atoms is moving according to the deformation of the nodes. Second with a new method, where the coupling atoms are put into a box with periodic boundary conditions. The box has the shape of an parallelepiped and is deformed according to the finite element movement. As the finite element deformation is arbitrary a close-fit parallelepiped is calculated from the nodal positions. The force on the bound atoms are redirected to the finite element nodes

using shape functions of the finite elements in a slightly modified way to ensure that the forces are only enacting on the finite element faces that are on the interface side to the finite elements. The coupling with the periodic boundary condition box provides more freedom to atoms and enables them to change phase.

For basic functionality tests of the method, for time being unrelated to phase transformation an iron potential by Mendelev et al. (2003) is selected. Concerning phase transformation, two potentials based on the Embedded Atom Method (EAM) are selected. The first potential has been developed by Meyer and Entel (1998) and is used to simulate the phase transformation between a body-centered cubic (BCC) and a face-centered cubic (FCC) lattice structure in iron. In addition, the potential by Mendelev et al. (2016) is used to simulate the phase transformation between hexagonal close-packed (HCP) and body-centered cubic lattice structure in titanium. The potentials are implemented into a self-developed molecular dynamics code as part of this thesis. This molecular dynamics code is integrated into the existing finite element solver NumPro, developed at the Institute for Structural Mechanics (IBB) at the University of Stuttgart.

Finally, four test cases are presented to validate the multiscale method. A tensile test and a bending test are simulated to verify the method's basic functionality. First, a reference solution is calculated with mostly molecular dynamics for both test cases. Unfortunately, it was not possible to apply boundary conditions in an external molecular dynamics program and converge to a quasi-static solution. Therefore, the horizontal coupling is used to calculate the reference solution with only the boundary conditions being simulated by finite elements. The tensile test shows good results for all tested methods in agreement with the molecular dynamics solution. The bending test is more complex and gives mixed results. The molecular dynamics displacement of the beam is the highest and the finite element solution with the vertical coupling the stiffest. The horizontal coupling methods are between the molecular dynamics solution and the vertical coupling solution. The bending results differ up to 35% compared to the molecular dynamics solution.

There are two phase transformation test cases performed, the first test case with vertical coupling only and the second test case with both vertical and horizontal coupling. For each of the coupling methods, all four phase transitions (BCC$\leftrightarrow$ FCC and HCP$\leftrightarrow$ BCC) are simulated. The test case using only vertical coupling shows very good results for all four phase transitions. The atoms in the MD subproblems at the integration points move as expected and the coarse-scale deformation is also very good, which has been verified by looking at the length ratios of the simulation cube's axes at the beginning and the end of the simulation.

In the test case for the combined method, all four previous transformations are investigated with a Cauchy coupling and the new proposed subboxes coupling introduced before. In the case of BCC$\leftrightarrow$ FCC phase transformation, the Cauchy type coupling shows good results for the transition because the transition only involves a rescaling of the axes. The newly proposed coupling performs just as well as the Cauchy coupling.

However, it needs more time steps to converge. In the case of the HCP$\leftrightarrow$BCC transition, the newly proposed method performs better than the Cauchy coupling. This is due to the fact that in the case of the Cauchy coupling the coupling atoms are bound by the deformation of the finite element nodes and cannot change their internal structure.

Preface

The following work was written during my time as scientific assistant at the Institute for Structural Mechanics at the University of Stuttgart. My thesis was financially supported by the Cluster of Excellence "SimTech", which is funded by the german research foundation (DFG). In addition, I want to acknowledge the support by the state of of Baden-Württemberg through bwHPC.

I want to thank my doctorial adviser, Prof. Dr.-Ing. habil. Manfred Bischoff, that he made it possible for me to work at the institute and that he supported me in my research. In addition, I also would like to express the other members of the examination committee, Prof. Dr. rer. nat. Dr. h. c. Siegfried Schmauder from the Institute for Materials Testing, Materials Science and Strength of Materials (IMWF, also in Stuttgart) and Prof. Dr.-Ing. Dennis Kochmann from ETH Zürich (previously at Caltech).

Prof. Schmauder also supported me by inviting me to his "Materials Mechanics Seminar", where I was able to present my work and got useful feedback. In 2016 I stayed for two months with Prof. Kochmann at Caltech in Pasadena, CA, where I was able to work on improving my molecular dynamics code and learned more about multiscale simulation.

I want to thank all my colleagues and friends for their support during my stay at the institute. I especially enjoyed the discussions at lunch and the delicious food at the mensa. Moreover, I want to thank Anne-Kathrin Schäuble for the philosophical discussions and Simon Bieber for the fun bicycle rides to the "Forschungstage". In addition, I want to thank Steffen Roth, Alexander Müller for carefully reading my thesis and all other collegues that helped me with my exam presentation. Finally, I want to thank my family for their support during the past years.

Stuttgart, August 2019, Tobias Willerding

Contents

List of Figures

List of Tables

Abbreviations and designations

Abbreviations

BCC .... body-centered cubic

CB .... Cauchy-Born

CML .... cubic material law

EAM .... embedded atom method

FCC .... face-centered cubic

FEM .... finite element method

HCP .... hexagonal close packed

IBB .... Institute for Structural Mechanics, german: Institut für Baustatik und Baudynamik

IMWF .... Institute for Materials Testing, Materials Science and Strength of Materials, german: Institut für Materialprüfung, Werkstoffkunde und Festigkeitslehre

MD .... molecular dynamics

MPI .... message Passing Interface

PBC .... periodic boundary conditions

SB .... subboxes coupling

VC .... vertical coupling

Mathematical notations

$(\bullet)^{-1}$ .... inverse of $(\bullet)$

$\dot{(\bullet)}$ .... time derivative of $(\bullet)$

$\ddot{(\bullet)}$ .... double time derivative of $(\bullet)$

$(\bullet)^{\mathrm{T}}$ .... transpose of $(\bullet)$

$(\bullet)^{-\mathrm{T}}$ .... transpose of the inverse of $(\bullet)$

$|(\bullet)|$ .... length of a vector $(\bullet)$

$\mathrm{DIV}(\bullet)$ ...... divergence of $(\bullet)$ with regard to the reference configuration

$\frac{\mathrm{d}(\bullet)}{\mathrm{d}(\bullet)}$ .... total derivative

$\frac{\partial(\bullet)}{\partial(\bullet)}$ .... partial derivative

Latin letters ..

a .... lattice constant

$\mathbf{a}$ .... acceleration

$\mathbf{A}_r$ .... area element of the reference configuration

$\mathbf{A}_c$ .... area element of the current configuration

Ω .... material body

$\mathbf{C}$ .... material matrix

C_{ij} .... elastic constants

C_{ijkl} .... elasticity tensor

$\mathbf{d}$ .... global vector of displacements

$\mathbf{D}$ .... damping matrix

e .... elementary charge

E .... energy

E .... Young's modulus

E_{pot} .... potential energy

$\mathbf{E}$ .... Green-Lagrange strain tensor

E_{kin} .... kinetic energy

$\mathbf{f}$ .... force

$\mathbf{f}_{\mathrm{int}}, \mathbf{f}_{\mathrm{ext}}$ ...... global vector of internal / external forces

$\mathbf{F}$ .... deformation gradient

Fe .... iron

$\hbar$ .... reduced Planck constant

$\mathbf{H}$ .... deformation state of the box for the periodic boundary conditions

$\mathbf{I}$ .... identity matrix

i .... imaginary unit

J .... Jacobi determinant

$\mathbf{J}$ .... Jacobi-Matrix

k_B .... Boltzmann constant

m	mass
m_e	electron mass
$\mathbf{M}$	mass matrix
n_{ele}	number of finite elements
n_{dof}	number of degree of freedoms
N	shape function
N_{v}	number of valence electrons
N_{s}	number of symmetry electrons
N_{atoms}	number of atoms
$\mathbf{P}$	first Piola-Kirchhoff stress tensor
q	surface load
$\mathbf{r}$	atom position
r	radius
r_{cut}	cutoff radius for molecular dynamics potential
r_{res}	reserve radius for atom neighbour search
$\mathbf{S}$	second Piola-Kirchhoff stress tensor
s	relative atom coordinate in the PBC box
t	time
$\mathbf{t}$	stress vector in the current configuration
t_0	initial time
Ti	titanium
$\mathbf{T}$	stress vector in the reference configuration
$\mathbf{u}$	displacement vector of a material point
$\dot{\mathbf{u}}$	velocity vector of a material point
$\ddot{\mathbf{u}}$	acceleration vector of a material point
W	strain energy function
$\mathbf{x}$	position vector in the current configuration
$\mathbf{X}$	position vector in the reference configuration
$Y(\theta,\phi)$	spherical harmonics function
Z	atomic number

Greek letters .

γ	Nosé-Hoover thermostat constant
δ_{IK}	Kronecker delta

δ .... variational operator

$\partial\Omega$ .... surface of the body

ϵ_0 .... vacuum permittivity

ζ, η, ξ .... natural finite element coordinates

ν .... poisson number

$\boldsymbol{\xi}$ .... position vector in natural element coordinates

∇ .... nabla operator

ρ_{m} .... volumetric mass density

ρ_{el} .... electron density

$\rho_{\mathrm{el, cut}}$ .... electron density cutoff

$\boldsymbol{\sigma}$ .... Cauchy stress tensor

τ .... slater type function

φ_{el} .... electron density pair function

χ .... mapping function between reference and current configuration

ψ .... wave function

$\Psi(\mathbf{C})$ .... strain energy function

Ψ_{4s}, Ψ_{3d} ..... double-ζ functions

ω .... Gauss integration weights

Ω .... Volume of the material body

Unit symbols .

Å .... Angstrom = 10^{-10} m

eV .... electron volt

fs .... femto seconds

GPa .... giga pascal

mm .... milli meter

1

Introduction

1.1 Motivation

Many materials, such as metals, show effects that can be modeled only with limited success on the coarse scale or cannot be modeled at all. These effects – such as crack propagation, plasticity, phase transformation and many others – require microscale modeling, because they are happening on a very fine scale and also in a very short time. This requires different computational methods compared to the methods traditionally used on the coarse scale. Although these effects happen very localized on a very small scale, they can still have a very big impact on the coarse scale. An easy to understand example is the crack. A small crack opening can increase the stress in a small region of a component. This higher stress will cause the crack to grow and may ultimately lead to failure of the component.

In order to have both the coarse scale and the fine scale modeled in one simulation, the concept of multiscale simulation was developed. The Multiscale simulation combines at least two different models in one simulation. Typical examples include the coupling of discrete elements and finite elements or molecular dynamics and finite elements.

An interesting future context, in which multiscale simulation could play an important rule, is the design of new materials without referring to purely phenomenological material laws, but instead creating the material modeling ab initio, starting with molecular dynamics or even quantum physics, working the way up over the length scales to the coarse scale.

In the formation of materials, especially metals, phase transformation plays an important role. Many materials have more than one possible lattice structure. Two interesting materials in this context are iron and titanium, which are shown in Figure 1.1.

Figure 1.1: Left: pure iron in different forms. Right: titanium crystal,
source left author: Alchemist-hp (talk) (www.pse-mendelejew.de), `https://commons.wikimedia.org/wiki/File:Iron_electrolytic_and_1cm3_cube.jpg`, CC BY-NC-ND 3.0
source right author: Alchemist-hp (talk) (www.pse-mendelejew.de), `https://commons.wikimedia.org/wiki/File:Titan-crystal_bar.JPG`, CC BY-NC-ND 3.0

Iron is alloyed with carbon to create steel, which is one of the most important alloys in use today. It is cheap and offers a wide range of possibilities from the construction industry to high-performance applications. Titanium is an expensive but lightweight material that is used e.g. in the aerospace industry or in orthodontics.

Iron has two possible lattice structures, a body-centered cubic structure at room temperature (α-iron) and a face-centered cubic structure above 1184 Kelvin (γ-iron). By using a suitable process, the high-temperature structure of steel can be stabilized at room temperature and is called austenite steel. Austenite steel has different properties compared to steel with a body-centered cubic structure. In the case of titanium, there are also two possible lattice structures: a hexagonal close-packed structure at room temperature and a body-centered cubic structure at high-temperature called beta-titanium. While hexagonal titanium is used in aerospace industry, beta-titanium is used e.g. in orthodontics. As phase transformation plays an important role in the formation of metals, it is of interest to include it in a multiscale simulation with the perspective of material design.

1.2 Goal

The goal of this thesis is to develop a multiscale method, consisting of finite elements and molecular dynamics, that can model phase transition in the finite elements, in the molecular dynamics part and also at the interface, enabling phase transformations throughout the multiscale simulation. The problem is visualized in Figure 1.2.

1. phase change in molecular dynamics	3. phase change at the interface	2. phase change in finite elements
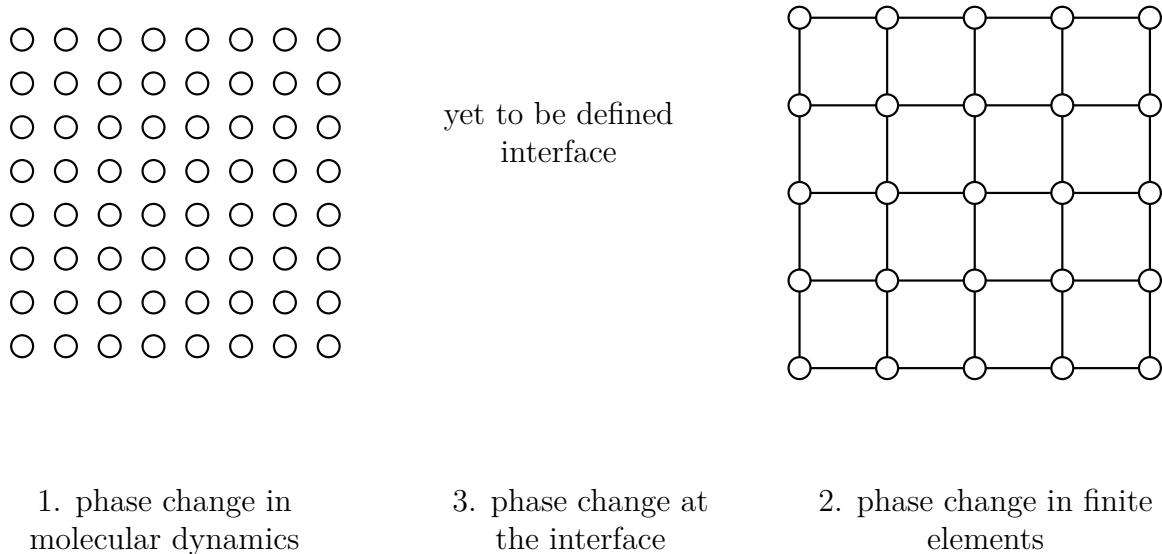
Figure 1.2: The problem to be solved: atoms (left side) are coupled with finite elements (right side) with a yet to be defined interface that can do phase transformation

This requires four steps:

1. Phase transformation in molecular dynamics: identification of molecular dynamics potentials for iron and titanium that are suitable for phase transformation.

2. Phase transformation in finite elements: development of a hierarchic concept for coupling finite elements and molecular dynamics similar to the FE^2-concept.

3. Phase transformation at the interface: development of a partitioned-domain concept for coupling finite elements and molecular dynamics that enables phase transformation at the interface

4. Validation of the concept in a number of test cases.

1.3 Structure of the thesis

The thesis is structured in eight chapters. It starts with Chapter 2, which gives a basic overview of atomic physics with a focus on the current atom model and electron density. In addition, the three different lattice structures – body-centered cubic, face-centered cubic and hexagonal close-packed – are presented and phase transformation between them is explained. In Chapter 3 an overview of molecular dynamics and the Embedded-Atom-Method (EAM) is given. Furthermore, the molecular dynamics potentials for iron and titanium used in this thesis are introduced and their correct implementation is verified. Quantities derived from molecular dynamics are explained and implementation of the molecular dynamics into program code is presented. The thesis continues with Chapter 4, which deals with the introduction to continuum mechanics and the nonlinear dynamic finite element method. From the kinematics, stress measures, balance law and material law a variational formulation is derived and discretized with finite elements. In Chapter 5 an overview of existing multiscale methods is given and advantages and disadvantages of those methods are presented with regard to phase transformation. Chapter 6 presents a hierarchic-partitioned-domain method to simulate phase transformation in a multiscale environment. The hierarchic part – called vertical coupling – and the partitioned domain part – called horizontal coupling – are explained in more detail. After the explanation of the method in Chapter 7 four different test cases are presented to validate the concept. These are a tensile test, a bending test, phase transformation using the hierarchical part only (vertical coupling) and a phase transformation simulation using the combined method. The results are summarized. In the last Chapter 8, conclusions and an outlook for further work are given.

2

Atomic physics

2.1 Atom model

On a fundamental level, every material consists of many atoms. An atom consists of the atomic nucleus and the electrons that surround it. The atomic nucleus is positively charged and is made of protons with a positive charge and neutrons with a neutral charge. Electrons have a negative charge. The number of electrons surrounding the nucleus is equal to the number of protons in the nucleus making the outside atomic charge neutral.
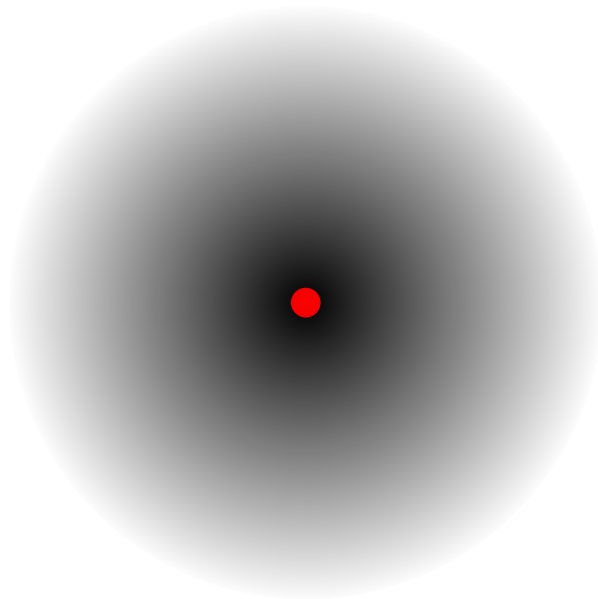
Figure 2.1: Atomic nucleus (red) and electron cloud (grey)

Of the two materials used in this thesis, iron has 26 protons and the most common isotope has 30 neutrons bringing the atomic mass to 56. Titanium has 22 protons and the most common isotope has 26 neutrons bringing the atomic mass to 48.

The electrons surrounding the nucleus are today interpreted as quantum objects with wave-like characteristics. Due to its wave-like nature, it is only possible to determine probabilities of finding an electron at a specific point around the nucleus. Zones with the same probability are called atom orbitals and are important for defining the electron density that is essential for the simulation of metals. Figure 2.1 shows the red nucleus in the center with grey symbolizing the electron cloud. The grey factor shows the integral of the probability function of the 1s-orbital schematically.

2.1.1 Wave function

The electron density used later in the molecular dynamics simulation (see Chapter 3) is based on the wave function. The wave function of an atom is given by the Schrödinger equation by SCHRÖDINGER (1926). The general time-independent Schrödinger equation is

$$\left[\frac{-\hbar^2}{2\mu} \nabla^2 + V(\mathbf{r}) \right] \Psi(\mathbf{r}) = E\Psi(\mathbf{r}). \tag{2.1}$$

Here $\mathbf{r}$ is the distance from the atomic nucleus, $\Psi(\mathbf{r},t)$ is the wave function, $\hbar$ the reduced Planck constant, μ the reduced mass, $V(\mathbf{r})$ the potential field and E the constant energy. ∇ is the nabla-differential operator. The solutions to the Schrödinger equation are the wave functions. Analytical solutions of the Schrödinger equation do only exist for simple cases like a single hydrogen atom.

We now look at a simple hydrogen atom. The potential $V(\mathbf{r})$ simplifies to the Coulomb force, with both the hydrogen nucleus and the electron having a single e-charge, just with opposing signs.

$$V(\mathbf{r}) = -\frac{e^2}{4\pi\epsilon_0} \frac{1}{|\mathbf{r}|} \tag{2.2}$$

$e = 1.6021766208(98) \cdot 10^{-19} \mathrm{C}$ is the elementary charge and $\epsilon_0 = 8.854187817 \cdot 10^{-12} \frac{\mathrm{F}}{\mathrm{m}}$ is the vacuum permittivity. The Schrödinger equation in this case is

$$\left[\frac{-\hbar^2}{2m_e} \nabla^2 - \frac{e^2}{4\pi\epsilon_0} \frac{1}{|\mathbf{r}|} \right] \Psi(\mathbf{r}) = E\Psi(\mathbf{r}). \tag{2.3}$$

The solution to the Schrödinger equation represented by the funtion $\varphi_{nlm}(r,\theta,\phi)$ in the spherical coordinate system is

$$\Psi(\mathbf{r}) \doteq \varphi_{nlm}(r,\theta,\phi) = \left(\frac{r}{nr_0}\right)^l \exp(im\phi) \exp\left(-\frac{r}{nr_0}\right) L_{n-l-1}^{2l+1}\left(\frac{2r}{nr_0}\right) P_{lm}(\cos\theta). \quad (2.4)$$

with $r_0 = \frac{4\pi\epsilon\hbar^2}{m_e e^2}$ being the Bohr atom radius. The functions $L_i^j(x)$ are the associated Laguerre polynomials and $P_{lm}(x)$ are the associated Legendre polynomials. The three integers n, l and m are introduced to characterize the wave function and called quantum numbers. The principal quantum number n identifies the permissible energy levels

$$E = -\frac{m_e e^4}{32\pi^2 \epsilon_0^2 \hbar^2 n^2} \quad (2.5)$$

with m_e being the mass of a single electron. l is the azimuthal quantum number and m the magnetic quantum number. They describe the orientation and shape of the solution. The wave function can be used to estimate the probability density of the hydrogen electron being in a specific space also called the electron density. The electron density of a specific orbital is defined as the product of the wave funtion and with its complex conjugate:

$$\rho_{\text{el},nlm}(r,\theta,\phi) = \varphi_{nlm}^*(r,\theta,\phi)\varphi_{nlm}(r,\theta,\phi) \quad (2.6)$$

Two examples of $\rho_{\text{el}} = 0.05$ can be seen in Figure 2.2 with $\varphi_{310}(r,\theta,\phi)$ (left)) and $\varphi_{320}(r,\theta,\phi)$ (right).
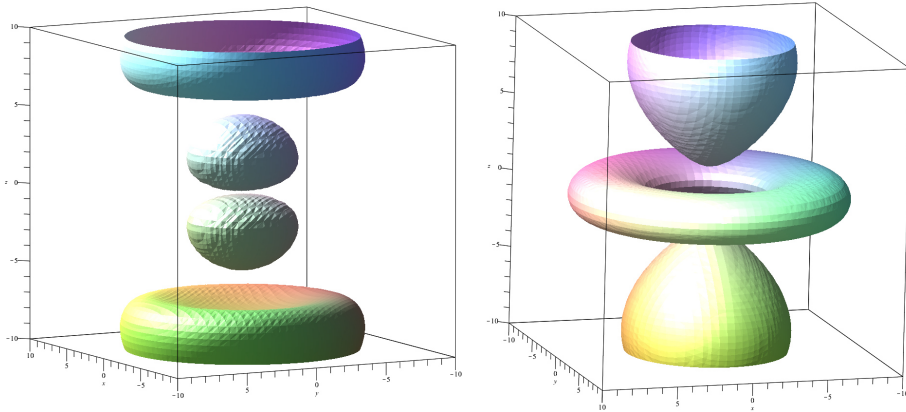
Figure 2.2: Orbitals of a single hydrogen atom, φ_{310} (left) and φ_{320} (right)

2.1.2 Electron density

The electron density for more complex atoms can be modeled with some approximations using the Hartree-Fock method (see HARTREE (1928), FOCK (1930)). This method can then describe the electron density as

$$\rho_{\mathrm{el}}(r) = \sum_{k=1}^{N_{\mathrm{orbital}}} n_k |\varphi_k(r)|^2, \tag{2.7}$$

where N_{orbital} is the number of orbitals, n_k is the number of atoms in the orbital and $\varphi_k(r)$ is the wave function of the orbital. This method is used for the electron density in the embedded atom method see e.g. the Meyer-Entel potential in Section 3.1.2. For a more detailed explanation of the electron density, see the book by TADMOR AND MILLER (2011).

2.2 Atomic lattice structures

Metals in a solid state have a periodic atomic lattice structure. An example of a perfect atomic lattice can be seen in Figure 2.3. Materials, in which the lattice is without defects as in Figure 2.3 are called single crystals. However, these ideal structures do only happen in rare cases. In reality, most metals consist of multiple crystals (or grains) in different orientations. The transition area between two crystal structures is called a grain boundary. Each crystal can have its own defects like single point defects, e.g. missing atoms, or line defects like dislocations.
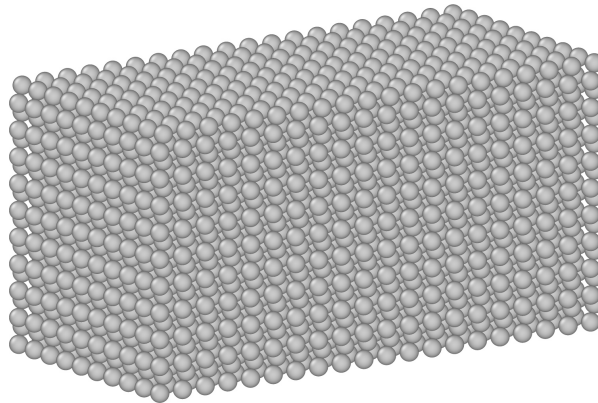
Figure 2.3: Atomic lattice of iron (body-centered cubic)

This thesis is limited to perfect single crystal only because phase transformation happens also in single crystals and the problem is much easier compared to polycrystals.

The three lattice structures investigated in this work are body-centered cubic, face-centered cubic and hexagonal close-packed.

2.2.1 Body-centered cubic

The body-centered cubic (BCC) lattice structure is seen in Figure 2.4. The atoms are sitting at the corners and in the center of the cube. The size of the lattice is defined by the lattice constant a. On average there are two full atoms in the unit cell of the BCC lattice. One full atom is in the center and eight 1/8 atoms are at the corners. The density of the system can then be easily computed by

$$\rho_{\mathrm{m, \, BCC}} = \frac{2m_{\mathrm{atom}}}{a_{\mathrm{BCC}}^3}. \tag{2.8}$$
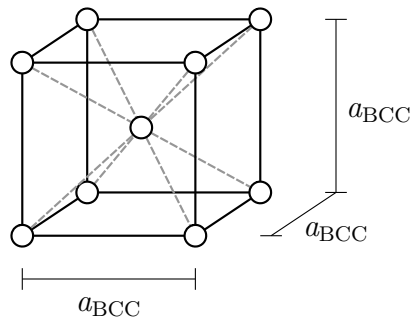
Figure 2.4: Body-centered cubic lattice

2.2.2 Face-centered cubic

Very similar to the body-centered cubic lattice structure is the face-centered cubic (FCC) lattice structure, as seen in Figure 2.5. In this case the atoms are sitting in the center of the surrounding surfaces and in the center of the cube.

The size of the lattice is also defined by the lattice constant a. On average there are four full atoms in the unit cell of the FCC lattice. One full atom is in the center and 6 1/2 atoms are at the center of the surfaces of the cube. The density of the system can then be easily computed by

$$\rho_{\mathrm{m, \, FCC}} = \frac{4m_{\mathrm{atom}}}{a_{\mathrm{FCC}}^3}. \tag{2.9}$$
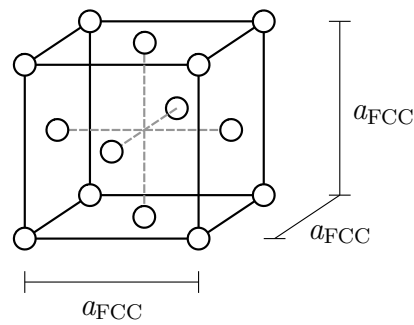
Figure 2.5: Face-centered cubic lattice

2.2.3 Hexagonal close-packed

The hexagonal close-packed structure is seen in Figure 2.6. The atoms are sitting at the corners of a hexagonal prism plus three atoms in the middle of the prism. The size of the lattice is defined by the lattice constants a_{HCP} and c_{HCP}. On average there are six full atoms in the unit cell of the HCP lattice. The density of the unit cell can then be easily computed by

$$\rho_{\text{m, HCP}} = \frac{4}{3}\sqrt{3}\frac{m_{\text{atom}}}{a_{\text{HCP}}^2 c_{\text{HCP}}}. \tag{2.10}$$
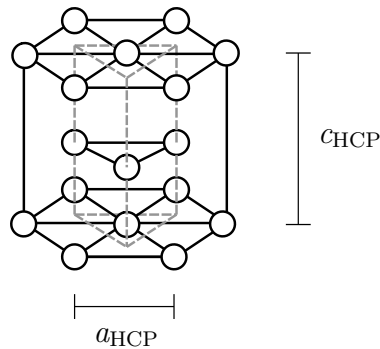
Figure 2.6: Hexagonal close-packed lattice

The FCC and HCP lattice are very similar to each other. As can be seen in Figure 2.6 the hcp has a ABABAB layer pattern. The FCC structure is almost identical, it only has a different arrangement of the layers in an ABCABC pattern. This is illustrated in Figure 2.7 .
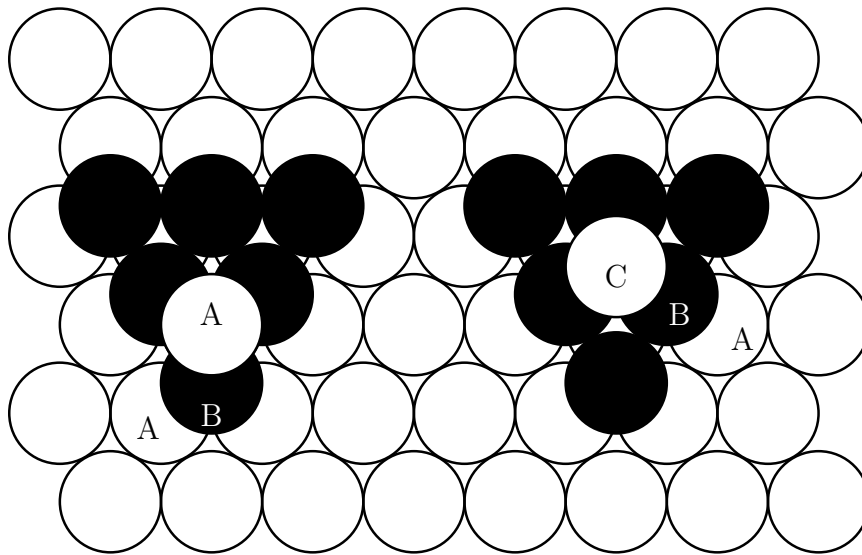
Figure 2.7: HCP lattice (left) and FCC lattice (right) comparison. HCP has ABAB structure, while FCC has ABCABC

2.3 Phase transformation

Phase transformation is a term to describe the transition from one material state to another. Often it is associated with the change of liquid water to water ice (freezing) or to water vapor (evaporation). However it can also be used to describe phase transition in solids from one solid phase to another solid phase. One famous transition is the change of graphite to diamond under high pressure and temperature. In this work the focus is on the transition between the body-centered cubic (BCC) and the face-centered cubic (FCC) lattice structure in iron and between hexagonal close-packed (HCP) and body-centered cubic lattice structure in titanium. Figure 2.8 shows the possible lattice structures of iron and titanium.
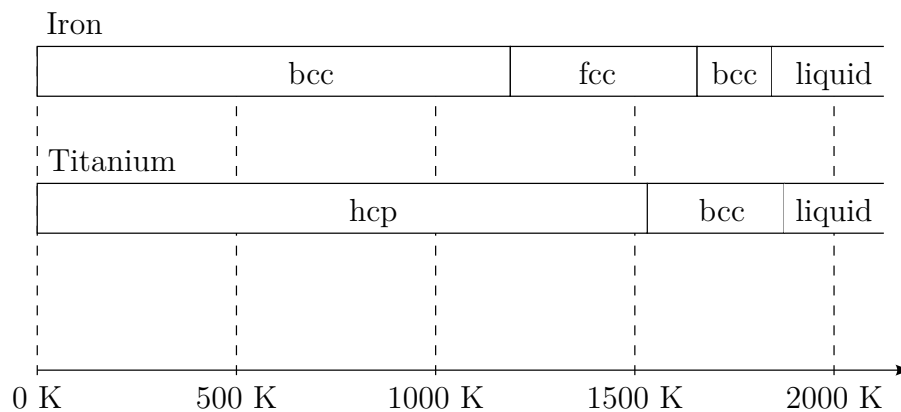
Figure 2.8: Solid phases of iron and titanium

Iron is often alloyed with carbon to create steel. If the carbon portion is close to zero, three typical structures can be observed in iron: ferrite (α-iron) between 0 K and 1184 K, austenite (γ-iron) between 1184 K and 1667 K and ferrite again, also called δ-iron, bewteen 1667 K and 1811 K. Above 1811 iron is in the liquid phase. α-iron and δ-iron have a body-centered cubic (BCC) lattice while γ-iron has a face-centered cubic phase (FCC).

Titanium is a metal that was discovered in 1791 by William Gregor. It also can appear in two stable lattice structures, hcp below 1155 K and bcc above 1155 K. It melts at 1941 Kelvin.

In the following, the transition from BCC to FCC and from FCC to FCC shall be looked at from a theoretical point of view.

2.3.1 Transition between BCC and FCC

The transition from BCC to FCC is quite simple from a theoretical point of view as it can be done by a simple scaling of the axis. In Figure 2.9 the transition is visible. On the left side, a BCC lattice is visible. The middle picture shows the lattice scaled by a factor of $\sqrt{2}$. On the right side, the lattice has been expanded to 2x2. The red lines show that a FCC structure can be discovered in the lattice. Therefore, BCC can be transformed into FCC simply by changing the ratio of the axes by a factor of $\sqrt{2}$. This transformation is known as the Bain transformation (EDGAR (1924)).
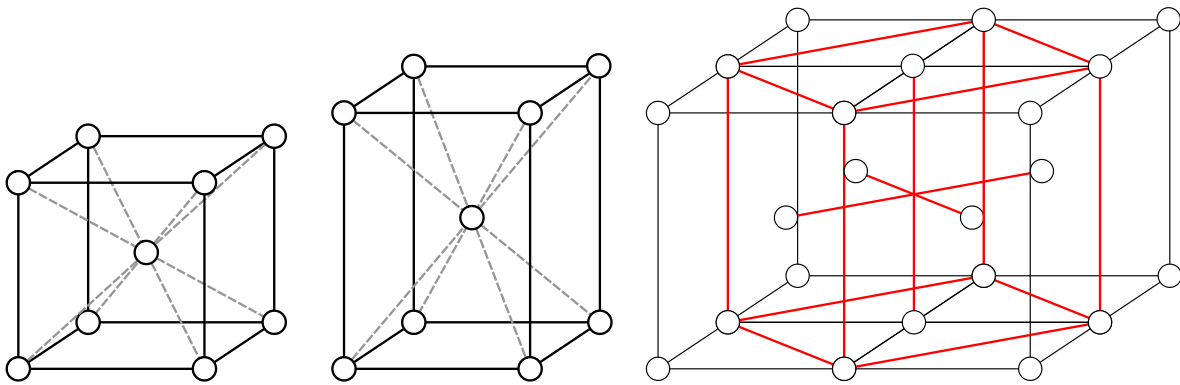
Figure 2.9: Transition from BCC to FCC

An experimental transformation can be seen in Figure 2.10, published by LU (2016). The figure shows the transition from BCC to FCC structure in the metal molybdenum. The shots are taken with a high-resolution transmission microscope (HRTEM). The lattice constant in the BCC phase is 0.31 nm = 3.1 Å. In the FCC phase the dimensions are 0.2 nm = 2 Å and 0.29 nm = 2.9 Å. Taking the ratio of the lengths

$$\frac{0.29 \text{ nm}}{2 \cdot 0.2 \text{ nm}}\sqrt{2} = 1.025 \approx 1, \tag{2.11}$$

it can be observed that it is very close to the factor of $\sqrt{2}$.
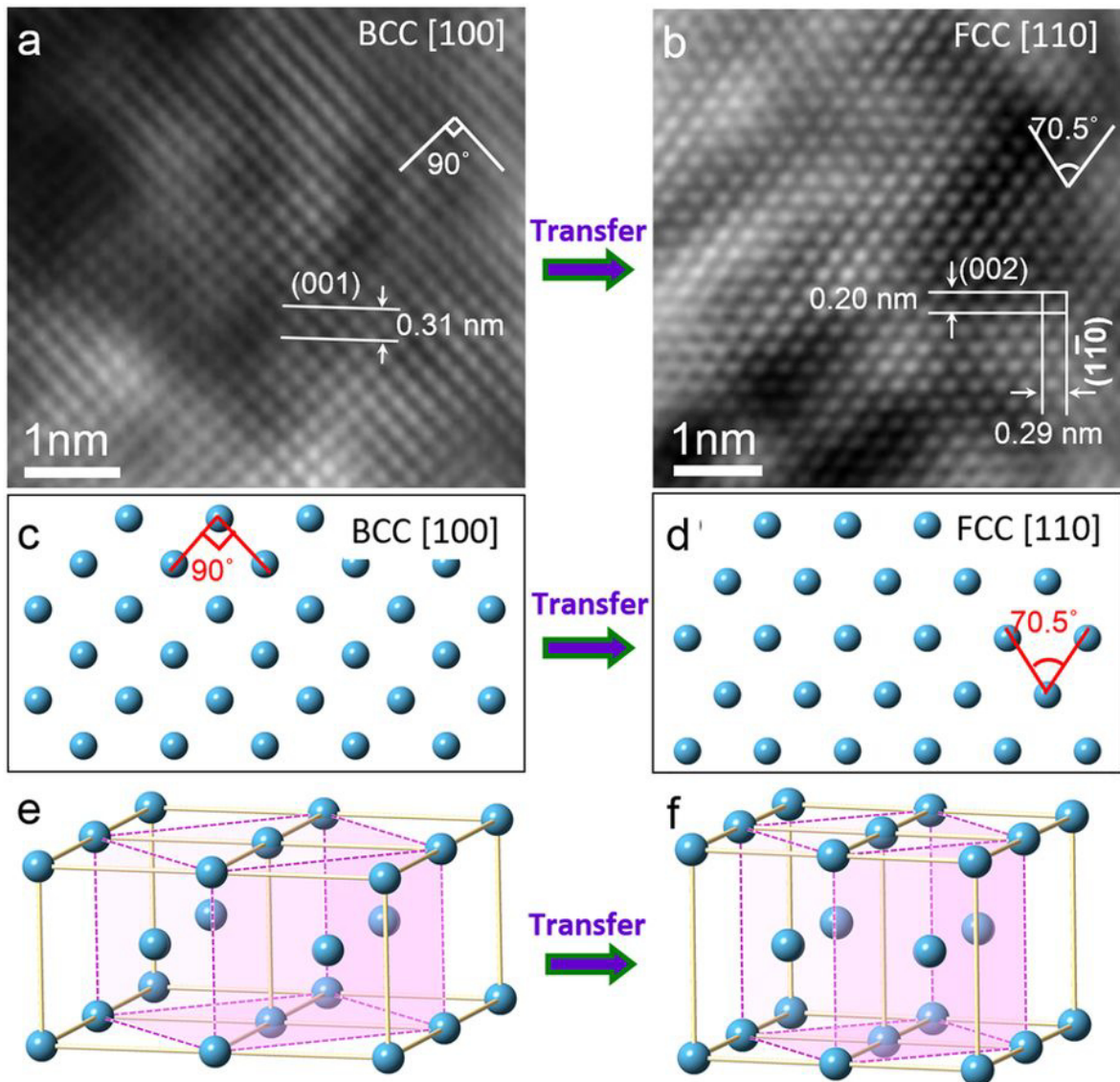
Figure 2.10: Original caption:"(a) HRTEM (High resolution transmission electron microscope) image of a Mo nanowire that was captured along the [100] direction; it shows a typical bcc lattice. (b) HRTEM image of Mo nanowire that was taken along the [100] direction; it shows typical fcc lattice features. (c) Atomic model of bcc Mo that project along the [100] direction. (d) Atomic model of the fcc Mo that project along the [110] direction. (e,f) 3D atomic structure show the transformation path from bcc Mo to fcc Mo." IMAGE SOURCE: Super-plastic Elongation of Body-centred Cubic Single Crystalline Molybdenum - Scientific Figure on ResearchGate from LU (2016). Available from: `https://www.researchgate.net/figure/Bcc-structure-to-fcc-structure-transformation-a-HRTEM-image-of-a-Mo-nanowire-that-was_fig6_297727984`, accessed 5 Feb, 2019, CC BY-4.0

2.3.2 Transition between FCC and HCP

The transition from FCC to HCP is more complex compared to the transition between BCC and FCC and is shown in Figure 2.11. First, it is important to discover the hexagonal structure in the FCC lattice. The lattice can also be interpreted as a number of hexagonal layers above each other. The layers are arranged in an ABCABC pattern, meaning the layers in A arrangement are always exactly on top of each other. The same is true for the B and C layers. If the layers are moved to change the arrangement to ABABAB, an HCP lattice is created. See also Figure 2.7.
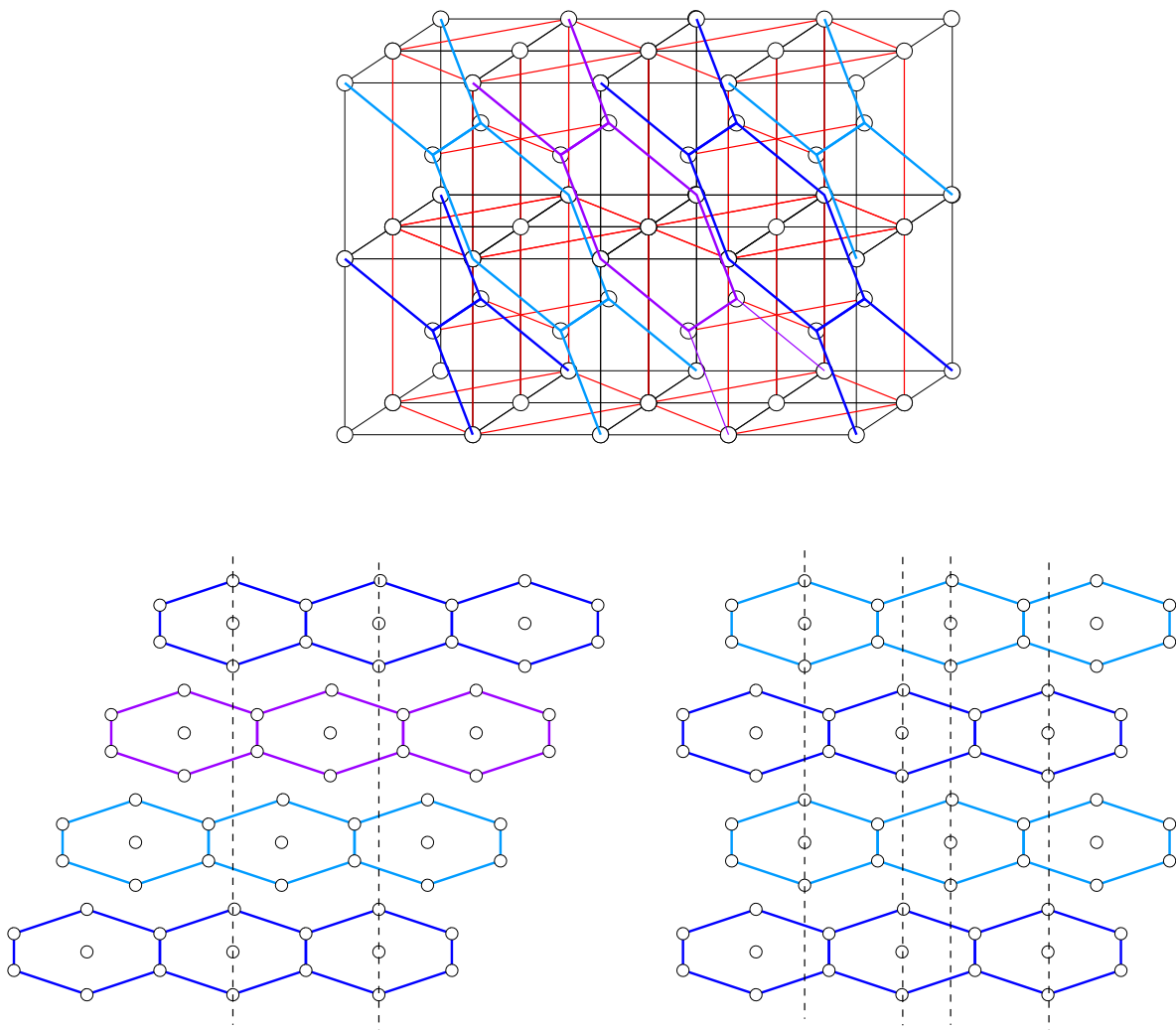
Figure 2.11: Transition from FCC to HCP, change of structure from ABCABC to ABABAB

<div align="right">

3

</div>

Molecular dynamics

3.1 Embedded-Atom-Method

Molecular dynamics is a computer simulation method to study atomistics. Molecules, which are two or more atoms that are chemically bound together, are assumed to be point masses, which interact with other molecules due to a potential. A lot of different types of potentials have been developed in the past to adjust simulations to a specific problem. The basic equation of motion of an individual molecule a is straightforward. The total potential energy of the system is derived with respect to the position of the atom $\mathbf{r}_a$.

$$\mathbf{f}_a = m\ddot{\mathbf{r}}_a = -\frac{\partial E_{\text{pot}}}{\partial \mathbf{r}_a} \tag{3.1}$$

In this thesis, the considered materials shall be limited to pure metals, so that each molecule consists of exactly one atom. However, by the definition above a molecule consists of at least two atoms so that the name "molecular dynamics" is a bit misleading.

The embedded atom method (EAM), presented by DAW AND BASKES (1984), is one method of molecular dynamics and it is used in this work. The EAM offers a good representation of the characteristics of metals. It consists of a pair potential term $V(r)$ and an embedding function $F(\rho_i)$ that depends on the electron density ρ_i. The pair potential term represents the repelling forces while the embedding function represents the attractive forces. The functions $F(\rho_i)$ and $V(r)$ are semi-empirical, while the electron density is a simplified solution of the Schrödinger equation using the Hartree-Fock-simplification.

The potential energy for the EAM has the following form:

$$E_{\text{pot}} = \sum_i F(\rho_i) + \frac{1}{2} \sum_{i \neq j} V(r_{ij}).$$

(3.2)

The electron density is described with a pair term different from the pair potential.

$$\rho_i = \sum_{j, j \neq i} \phi(r_{ij})$$

(3.3)

Both $F(\rho)$ and $\phi(r)$ consist of one function each, because only pure single crystal metals are considered in this work.

From the EAM potential, the force $\mathbf{f}_a$ on atom a can be derived and it is computed as follows:

$$\mathbf{f}_a = m\ddot{\mathbf{r}}_a = -\frac{\partial E_{\text{pot}}}{\partial \mathbf{r}_a} = -\sum_{i, i \neq a} \left[\left(\frac{\partial F(\rho_a)}{\partial \rho_a} + \frac{\partial F(\rho_i)}{\partial \rho_i} \right) \frac{\partial \phi(r_{ai})}{\partial \mathbf{r}_a} + \frac{\partial V(r_{ai})}{\partial \mathbf{r}_a} \right]$$

(3.4)

However, as the potential data is implemented as a tabulated format (see also section about Implementation), it makes more sense to formulate the potential as a function of r^2 instead of r. This avoids the time-consuming calculation of the length of vector $\mathbf{r}$.

In the following three EAM potentials are presented that are used in this work. The iron potential by MENDELEV ET AL. (2003) is used for basic functionality tests of the multiscale method that are unrelated to phase transformation. The iron potential by MEYER AND ENTEL (1998) is used for simulating phase transformation in iron. Finally, the potential by MENDELEV ET AL. (2016) is used for the phase transformation simulation in titanium.

3.1.1 Iron potential by Mendelev et al

The potential by MENDELEV ET AL. (2003) is a recently developed potential for iron. It shows good elastic mechanical stress. The functions $\phi_{\text{el}}(r)$, $F(\rho)$ and $V(r)$ can be seen in Figures 3.1 and 3.2. The potential files were provided by the Institute for Materials Testing, Materials Science and Strength of Materials (IMWF).

As can be seen from good agreement of the elastic constants in Table 3.1, the potential has been implemented in the molecular dynamics code in an accurate way.
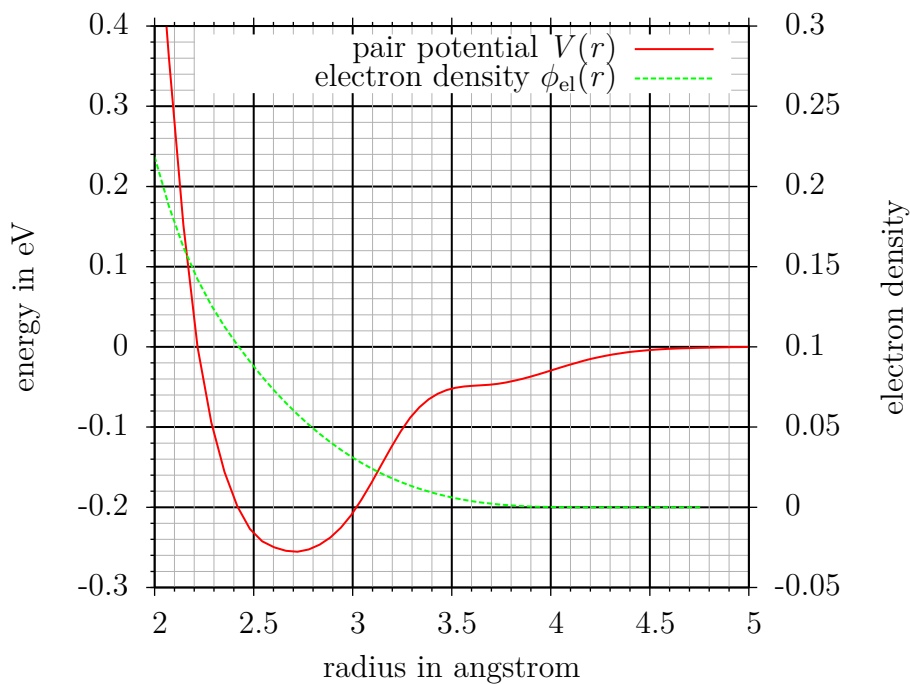
Figure 3.1: Electron density and pair potential function of the iron potential by Mendelev
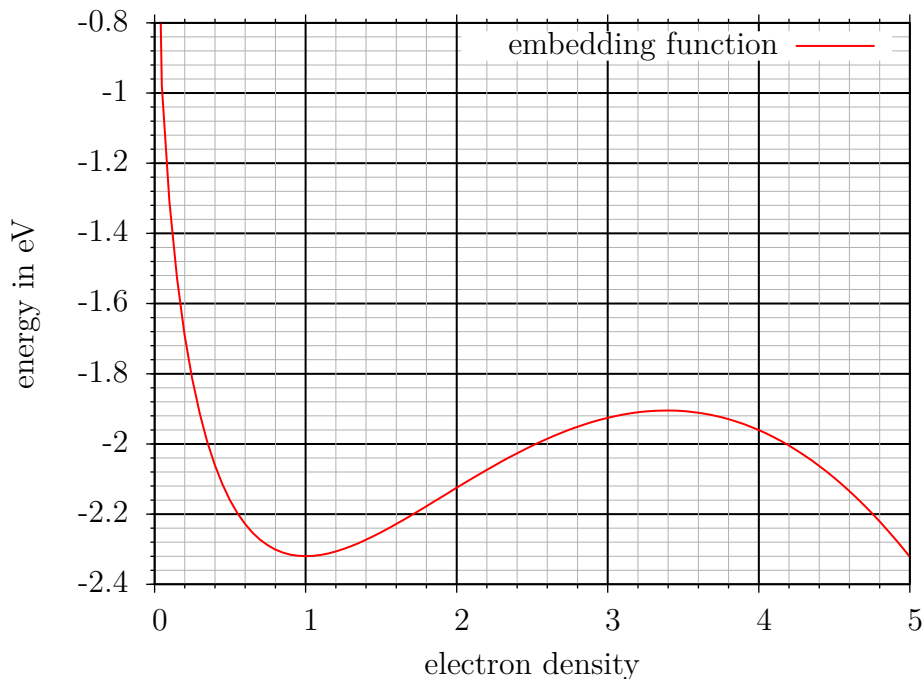
Figure 3.2: Embedding function $F(\rho)$ of the iron potential by Mendelev

Constant	Results	Reference Mendelev et al. (2003)
$C_{11}/$ GPa	243.7	242.4
$C_{12}/$ GPa	143.5	145.0
$C_{44}/$ GPa	115.9	116.0

Table 3.1: Comparison of calculated potential values compared to reference at zero Kelvin

3.1.2 Iron potential by Meyer-Entel

The EAM potential by MEYER AND ENTEL (1998) is one of the few potentials that can be used to simulate phase transformationWANG AND URBASSEK (2013). This potential uses double ζ-wave functions from CLEMENTI AND ROETTI (1974) for the calculation of the electron density. The potential was constructed from the paper by MEYER AND ENTEL (1998) and was not acquired in tabulated format.

Pair potential function

The function $V(r)$ in the EAM is composed as follows

$$V(r) = \frac{1}{4\pi\epsilon_0} \frac{Z^2(r)}{r},$$ (3.5)

with $\epsilon_0 = 5.3396 \cdot 10^{-3} \frac{e}{V\text{Å}}$. The function $Z(r)$ is the coulomb force and represented by a cubic spline interpolation with parameters as in Table 3.2.

r/a	0	0.7	0.87	0.94	1.0	1.2
Z in eV	26	1.4403	0.25452	0.1491	0.0734	0
Z' in eV/Å	0					0

Table 3.2: Coefficients for pair potential with $a = 2.8665\text{Å}$

The pair potential can be seen in Figure 3.3.

Electron density

MEYER AND ENTEL (1998) use the following ansatz for the electron density.

$$\rho_{el}(r) = N_{4s}|\varphi_{4s}(r)|^2 + (N_v - N_{4s})|\varphi_{3d}(r)|^2 - \rho_c.$$ (3.6)

N_v is the number of valence electrons, iron has 8. And N_{4s} is the number of s symmetry atoms, iron has 0.57. The functions $\varphi_{4s}(r)$ and $\varphi_{3d}(r)$ are double-ζ functions and can be gained from CLEMENTI AND ROETTI (1974). They are a linear combination of slater-type functions.

$$\varphi_{4s}(r) = \sum_{i=1}^{8} c_{i,4s}\tau_{i,4s}(r)$$ (3.7)

$$\varphi_{3d}(r) = \sum_{i=1}^{2} c_{i,3d}\tau_{i,3d}(r) \tag{3.8}$$

In Table 3.3 the coefficients for $\varphi_{4s}(r)$ and $\varphi_{3d}(r)$ are given.

index	1	2	3	4	5	6	7	8
$c_{i,4s}$	-0.00392	-0.03027	-0.02829	0.15090	-0.21377	-0.05096	0.50156	0.60709
$c_{i,3d}$	0.40379	0.71984						
$n_{i,4s}$	1	1	2	2	3	3	4	4
$n_{i,3d}$	3	3						
$\zeta_{i,4s}$	27.0335	19.0104	13.51700	10.1305	5.2166	3.47616	1.92517	1.07742
$\zeta_{i,3d}$	6.06828	2.61836						

Table 3.3: Coefficients for electron density of Meyer-Entel potential

The functions τ_i are slater type functions of the form

$$\tau_i = (2\zeta_i)^{n_i}\sqrt{\frac{2\zeta_i}{(2n_i)!}}\, r^{n_i-1} \exp(-\zeta_i r)\, Y_{lm}(\theta,\phi) \tag{3.9}$$

with $Y_{lm}(\theta,\phi)$ being spherical harmonics defined as

$$Y_{lm}(\theta,\phi) = (-1)^m \sqrt{\frac{(2\ell+1)}{4\pi}\frac{(\ell-m)!}{(\ell+m)!}}\, P_{lm}(\cos\theta)\, e^{im\phi}. \tag{3.10}$$

The functions $P_{lm}(x)$ are the associated Legendre polynomials. However, the EAM potential does only depend on interatomic distances and not on angles. It is unclear how the $Y_{lm}(\theta,\phi)$ was dealt with in the paper by MEYER AND ENTEL (1998). It could have been simply left out or averaged over the domain. In this work $Y_{lm}(\theta,\phi) = Y_{00}(\theta,\phi) = \frac{1}{\sqrt{4\pi}}$. The same assumption has been used by DAW AND BASKES (1984).

The electron density function can be seen in Figure 3.3.

Embedding function

The embedding function is a function described by cubic spline interpolation. The interpolation points are given in Table 3.4.

The embedding function can be seen in Figure 3.4.
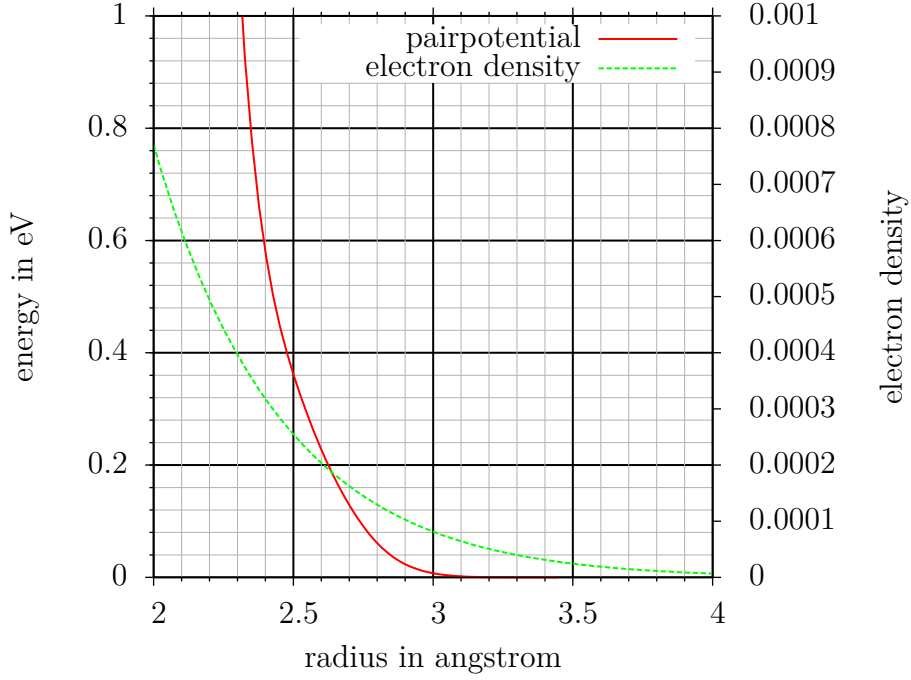
Figure 3.3: Electron density and pair potential function of the iron potential by Meyer-Entel

ρ/ρ_0	0	0.5	1.0	2.0	2.3
F in Ry	0	-0.2823	-0.4276	-0.3030	0
F in eV	0	-3.841	-5.818	-4.123	0
F'' in eV/Å^2	0				0

Table 3.4: Coefficients for embedding function with $\rho_0 = 2.776 \cdot 10^{-3}$

Validation

As can be seen in Table 3.5, the computed values for the potential show in general a good agreement compared to the reference. However, there are some differences in C_{44} that may be related to the choice of $Y_{lm}(\theta,\phi)$.

Constant	Results	Reference MEYER AND ENTEL (1998)
C_{11}/ GPa	256.8	251.0
C_{12}/ GPa	134.8	130.4
C_{44}/ GPa	106.9	118.7
lattice constant BCC / Å	2.888	2.866
lattice constant FCC / Å	3.708	3.751

Table 3.5: Comparison of calculated potential values compared to reference at zero Kelvin
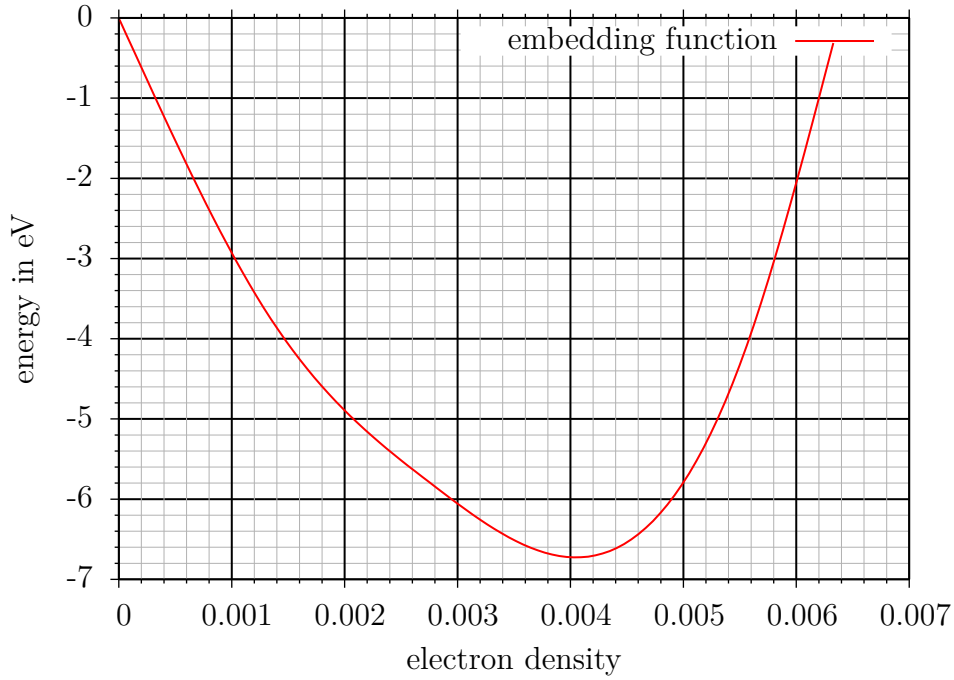
Figure 3.4: Embedding function of the iron potential by Meyer-Entel

3.1.3 Titanium potential by Mendelev et al

The paper by MENDELEV ET AL. (2016) provides three different titanium potentials. According to the authors, the first potential is most suited for phase transformation simulation. Therefore, this potential is used in this thesis for simulation of the transition between HCP and BCC. The potential files were provided with the paper. The electron density and pair potential function can be seen in Figure 3.5 and the embedding function in Figure 3.6.

Constant	Results	Reference MENDELEV ET AL. (2016)
lattice constant HCP a / Å	2.96	2.947
c/a (HCP)	1.596	1.597
lattice constant BCC / Å	3.29	3.251

Table 3.6: Elastic constants for the Titanium potential from MENDELEV ET AL. (2016)

The lattice constants do fit with the reference as seen in Table 3.6.
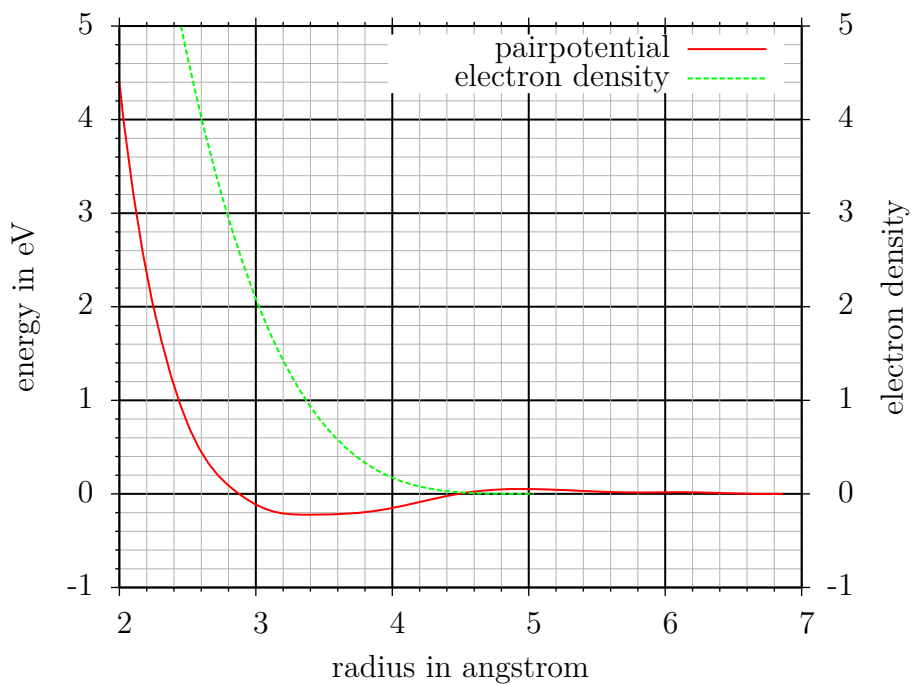
Figure 3.5: Electron density and pair potential function of the titanium potential
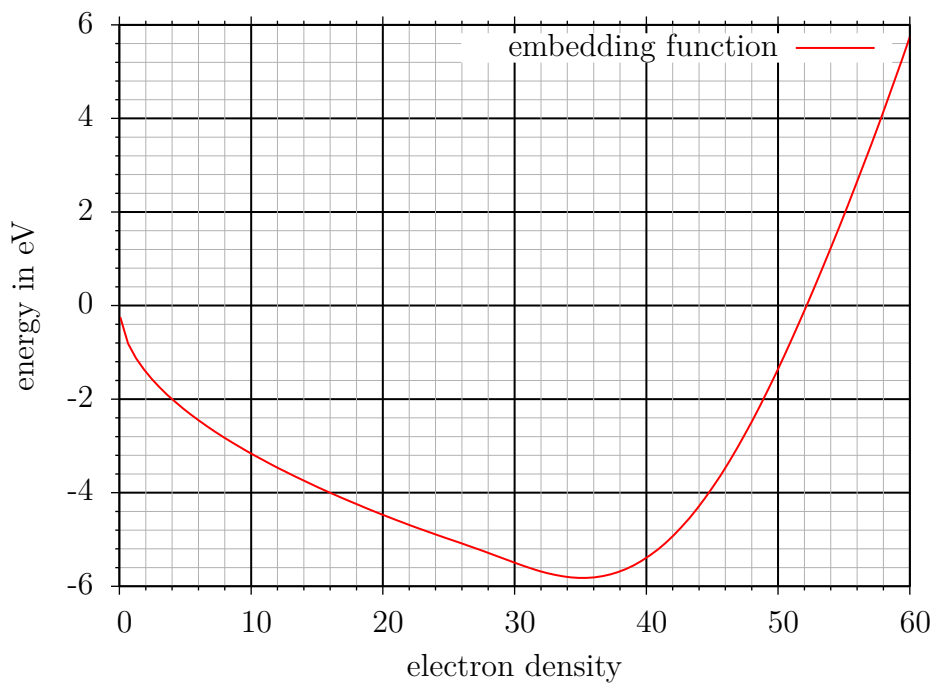
Figure 3.6: Embedding function of the titanium potential

3.2 Canonical ensemble

A canonical ensemble is a system consisting of a number of particles N and a volume V at temperature T. The kinetic energy of the atoms is equivalent to the temperature. The system is in contact with a heat bath, that can add or remove energy from the system to maintain a constant temperature T. The particles – or atoms in the case of molecular dynamics – move according to the following equation

$$m\ddot{\mathbf{r}}_i = -\frac{\partial E_{\text{pot}}}{\partial \mathbf{r}_i}. \tag{3.11}$$

The potential energy is represented by the EAM potential, see equation (3.2). The particles have a kinetic energy

$$E_{\text{kin}} = \sum_{i=1}^{N} \frac{1}{2} m_i \mathbf{v}_i^2. \tag{3.12}$$

The heat bath can add or remove energy to keep the kinetic energy constant. The total energy $E_{\text{tot}} = E_{\text{pot}} + E_{\text{kin}}$ is, therefore, not constant in this ensemble.

3.2.1 Time integration

Time integration of the molecular dynamics code is done with the Verlet time integration method VERLET (1967). The second derivative with central differences is:

$$\ddot{\mathbf{r}}_t = \frac{\mathbf{r}_{t+1} - 2\mathbf{r}_t + \mathbf{r}_{t-1}}{\Delta t^2}. \tag{3.13}$$

This can be rearranged to

$$\mathbf{r}_{t+1} = 2\mathbf{r}_t - \mathbf{r}_{t-1} + \Delta t^2 \ddot{\mathbf{r}}_t. \tag{3.14}$$

The velocities can be calculated only for the current and not for the next time step

$$\dot{\mathbf{r}}_t = \frac{\mathbf{r}_{t+1} - \mathbf{r}_{t-1}}{2\Delta t}. \tag{3.15}$$

3.2.2 Velocity distribution

The velocities of the atoms are distributed according to the Maxwell-Boltzmann distribution. An atom has three degrees of freedom, the positions x, y and z with the according

velocities v_x, v_y and v_z. Each velocity component follows a normal distribution around the average velocity $\mu = 0$ m/s.

$$f(v \mid \mu = 0, p) = \frac{1}{\sqrt{2\pi p^2}} e^{-\frac{(v-\mu)^2}{2p^2}} \tag{3.16}$$

$$= \frac{1}{\sqrt{2\pi p^2}} e^{-\frac{v^2}{2p^2}} \tag{3.17}$$

with the scaling factor $p = \sqrt{\frac{kT}{m}}$ with $k = 8.6173303 \cdot 10^{-5} \frac{\text{eV}}{\text{K}}$ being the Boltzmann-constant, T the temperature and m the mass of the atom.

The absolute velocity

$$|\mathbf{v}| = \sqrt{v_x^2 + v_y^2 + v_z^2} \tag{3.18}$$

follows the Maxwell-Boltzmann distribution

$$f(v) = \sqrt{\frac{2}{\pi}} \frac{v^2 e^{-v^2/(2p^2)}}{p^3}. \tag{3.19}$$

The kinetic energy of the atoms can be calculated according to

$$E_{\text{kin}} = \frac{1}{2} \sum_{i=1}^{N} m_i |\mathbf{v}_i|^2. \tag{3.20}$$

Assuming the mass m_i to be the same for all atoms and using the average squared speed of the Maxwell-Boltzmann distribution $\langle v^2 \rangle = 3p^2$, the kinetic energy becomes

$$E_{\text{kin}} = \frac{3}{2} N m p^2 \tag{3.21}$$

$$= \frac{3}{2} N k T. \tag{3.22}$$

The Boltzmann distribution for iron at 300 K can be seen in Figure 3.7.
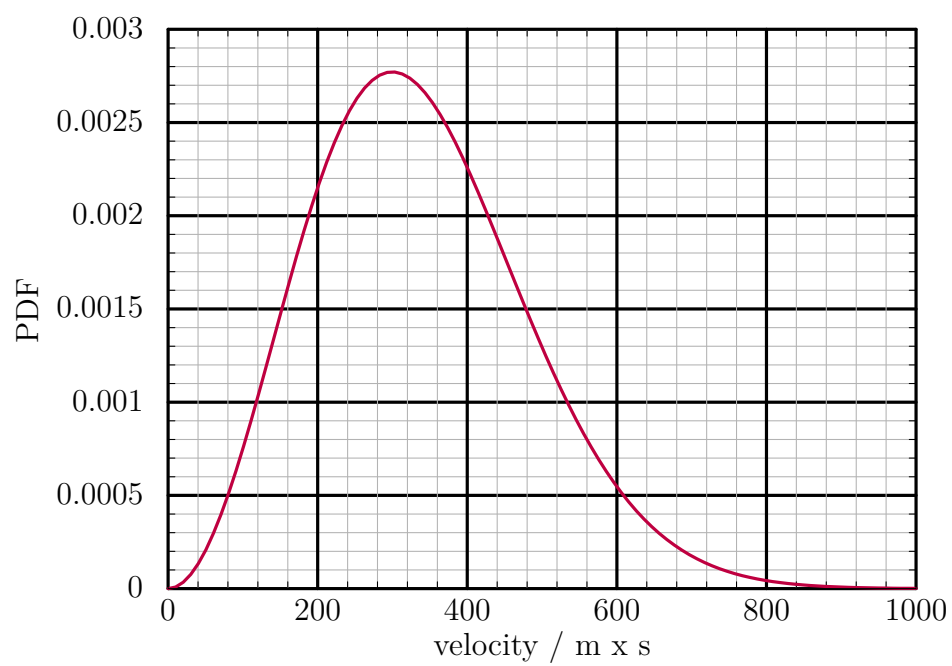
Figure 3.7: Probability density function (PDF) of the Maxwell-Boltzmann distribution

3.3 Constraints

3.3.1 Starting configuration

In order to define the starting configuration of a molecular dynamics simulation, the positions $\mathbf{r}_0$ and the velocities $\dot{\mathbf{r}}_0$ of all atoms must be defined.

The initial positions are defined by the initial crystal structure and are loaded from a data file. For possible configurations see Section 2.3.

According to Boltzmann the initial velocity distribution of the atoms represents a specific temperature. The three velocity components are initialized with a random generator following a normal distribution as in equation (3.17).

3.3.2 Periodic boundary conditions

It is often the case that the behavior of atoms can be reduced to a representative volume element consisting of a small number of atoms representing a field of an infinite number of atoms. This can be done with periodic boundary conditions (PBC). This representative volume element has the shape of a parallelepiped.

PBC means that atoms close to the boundary of the box can see atoms at the other side of the box. Furthermore, if the atoms leave the box, they just move in from the other side of the box, keeping the number of atoms inside the box constant.

A molecular dynamics problem with periodic boundary conditions (PBC) can be seen in Figure 3.8. The box has the form of a parallelepiped, it is defined by the span of the three vectors $\mathbf{a}$, $\mathbf{b}$ and $\mathbf{c}$.
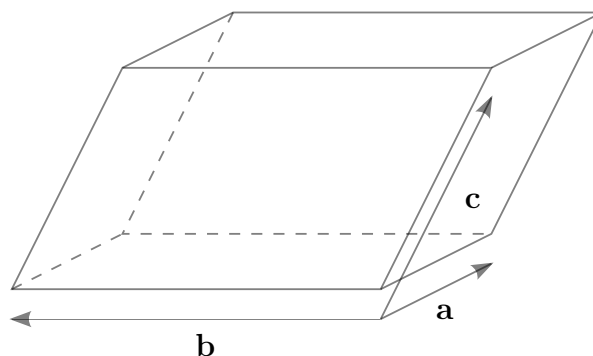
Figure 3.8: Parallelepiped defined by the vectors $\mathbf{a}$, $\mathbf{b}$ and $\mathbf{c}$

It is then possible to describe the deformation of the parallelepiped with the matrix $\mathbf{H}$.

$$\mathbf{H} = \begin{bmatrix} \mathbf{a} & \mathbf{b} & \mathbf{c} \end{bmatrix} \tag{3.23}$$

The current state $\mathbf{H}$ can be described with a deformation gradient $\mathbf{F}$, with $\mathbf{H}_0$ being the reference state. For a definition of the deformation gradient, see equation (4.6) in Chapter 4.

$$\mathbf{H} = \mathbf{F}\mathbf{H}_0 \tag{3.24}$$

From the position $\mathbf{r}$ of an atom, the position can be recalculated into the PBC-box coordinate system by defining

$$\mathbf{r} = \mathbf{H}\mathbf{s} + \mathbf{r}_0 \tag{3.25}$$

It is then possible to calculate the relative coordinate $\mathbf{s}$ by evaluating

$$\mathbf{s} = \mathbf{H}^{-1}(\mathbf{r} - \mathbf{r}_0). \tag{3.26}$$

For the atom to be in the PBC-box all three $\mathbf{s}$ values s_1, s_2 and s_3 must be between

$$0 \leq s_i \leq 1. \tag{3.27}$$

If the value of s_i is below 0, the minimum necessary integer will be added to raise the value back to the range between 0 and 1. If the value is above 1, the minimum necessary integer will be subtracted accordingly. After correction, the new $\mathbf{x}$-coordinate can be calculated according to equation (3.25).

3.3.3 Thermostat

The Nosé-Hoover thermostat (see EVANS AND HOLIAN (1985)) will be used for temperature control. This thermostat can keep a canonical ensemble at constant temperature. It modifies the acceleration of the particles in the following way

$$m\ddot{\mathbf{r}}_i = -\frac{\partial E_{\mathrm{pot}}}{\partial \mathbf{r}_i} - \gamma m\dot{\mathbf{r}}_i. \tag{3.28}$$

γ is a friction term that initializes at $\gamma_0 = 0$ and evolves according to the equation

$$\dot{\gamma} = c_\gamma(E_{\mathrm{kin, \, target}} - E_{\mathrm{kin, \, current}}) \tag{3.29}$$

where $E_{\text{kin, target}} = \frac{3}{2}NkT$ and $E_{\text{kin, current}} = \frac{1}{2}\sum_{i=1}^{N} m_i|\mathbf{v}_i|^2$. c_γ is a constant that describes the convergence behavior to the target temperature.

3.3.4 Barostat

Parrinello and Rahman (1981) proposed a method to keep a molecular dynamics simulation with periodic boundary conditions at a desired stress state. For example, it could be desirable to analyze a phenomenon at constant zero stress. In order to achieve this, the periodic boundary condition box is deformed in such a way that the calculated virial stress (see Section 3.4.1) is converging to the desired value. A detailed discussion of barostat (in combination with thermostat) can be found in Ray and Rahman (1985).

In this work a slightly different formulation from Parrinello-Rahman is used. The deformation gradient of the periodic boundary condition box is defined as $\mathbf{H} = \mathbf{F}\mathbf{H}_0$ (equation 3.24). The evolution of $\mathbf{F}$ can be described by

$$M\ddot{\mathbf{F}} = \Omega\left(\frac{\mathbf{F}\mathbf{S}\mathbf{F}^{\text{T}}}{J} - \boldsymbol{\sigma} - \gamma_{\text{damping}}\dot{\mathbf{F}}\right)\mathbf{F} \tag{3.30}$$

as described in Tadmor and Miller (2011), equations (9.70) and (9.71). It is called the finite strain $\text{N}\sigma\text{E}$ ensemble by the authors.

3.4 Derived Quantities

3.4.1 Stress

The stress-tensor of atoms can be calculated by using the virial stress, which is based on the virial theorem by Clausius (1870). The virial stress is defined as

$$\boldsymbol{\sigma} = \frac{1}{\Omega}\left(\underbrace{-\sum_i m_i\mathbf{v}_i\otimes\mathbf{v}_i}_{\text{kinetic part}} + \underbrace{\sum_{i,j<i}\mathbf{r}_{ij}\otimes\mathbf{f}_{ij}}_{\text{force part}}\right). \tag{3.31}$$

The stress is composed of a kinetic part and a force part. The kinetic part depends on the velocities $\mathbf{v}_i$ and masses m_i of the atoms and reduces the stress with increasing velocity. As the velocity is related to temperature, this can be interpreted as pressure due to inhibited thermal strain. The force part relates to the interatomic distances

$\mathbf{r}_{ij}$ and forces $\mathbf{f}_{ij}$. Ω is the volume of the space containing the atoms. If the space is small enough, even the stress of a single atom can be calculated. However, often the averaged stress of a parallelepiped with periodic boundary conditions is of interest. The virial stress is equivalent to the Cauchy stress, as shown by SUBRAMANIYAN AND SUN (2008).
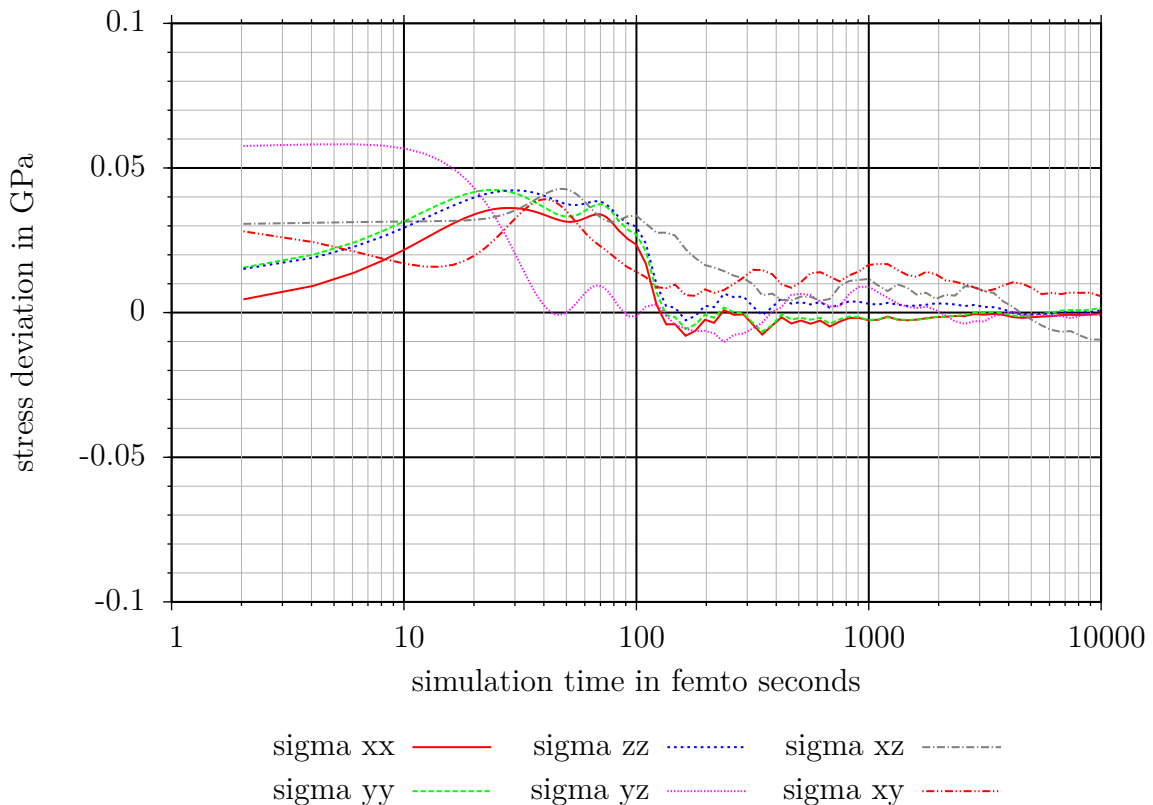
Figure 3.9: Convergence behavior stresses in molecular dynamics subproblem with periodic boundary conditions

The stress in a molecular dynamics simulation is fluctuating around the mean value. In order to demonstrate this, a simple molecular dynamics problem with fixed periodic boundary conditions and constant temperature at $T = 300$ K is simulated. The Meyer-Entel potential is used. As can be seen in Figure 3.9, all six stress converge to a value. The normal stresses have a better convergence than the shear stresses.

3.4.2 Elastic constants

In a perfect crystal the material matrix of a cubic lattice consists of three independent values C_{11}, C_{12} and C_{44}.

$$
\mathbf{C} = \begin{bmatrix}
C_{11} & C_{12} & C_{12} & 0 & 0 & 0 \\
C_{12} & C_{11} & C_{12} & 0 & 0 & 0 \\
C_{12} & C_{12} & C_{11} & 0 & 0 & 0 \\
0 & 0 & 0 & C_{44} & 0 & 0 \\
0 & 0 & 0 & 0 & C_{44} & 0 \\
0 & 0 & 0 & 0 & 0 & C_{44}
\end{bmatrix}
\tag{3.32}
$$

According to DAW AND BASKES (1984) the elastic constants can be calculated with the following expresson:

$$
C_{ijkl} = \langle C_{ijkl}^{\text{Born}} \rangle - \frac{V}{k_B T} \left(\langle \sigma_{ij} \sigma_{kl} \rangle - \langle \sigma_{ij} \rangle \langle \sigma_{kl} \rangle \right) + \frac{2 N k_B T}{V} \left(\delta_{ik} \delta_{jl} + \delta_{il} \delta_{jk} \right).
\tag{3.33}
$$

The expression consists of the Born term (BORN AND HUANG (1954)) and temperature related corrections. Here V is the volume, T the temperature, k the Boltzmann constant, σ the stress tensor, N the number of atoms and δ_{ij} the Kronecker-delta. The brackets $\langle \rangle$ symbolize averaging over time. If the temperature is zero, then the temperature term is omitted and an average over time is not necessary. The born term is a sum of three terms:

$$
C_{ijkl}^{\text{Born}} = B1_{ijkl} + B2_{ijkl} + B3_{ijkl}.
\tag{3.34}
$$

The three terms are given by the following three equations. The term r_{abi} is the i-entry of the vector $\mathbf{r}_{ab} = \mathbf{r}_b - \mathbf{r}_a$.

$$
B1_{ijkl} = \frac{1}{\Omega} \sum_{\substack{a,b=1 \\ a \neq b}}^{N} \left[\frac{\partial^2 V}{\partial r_{ab}^2} - \frac{1}{r_{ab}} \frac{\partial V}{\partial r_{ab}} \right] \frac{r_{abi} r_{abj} r_{abk} r_{abl}}{r_{ab}^2}
\tag{3.35}
$$

$$
B2_{ijkl} = \frac{1}{\Omega} \sum_{a,b=1}^{N} \frac{\partial F_a}{\partial \rho} \left(\frac{\partial^2 \rho}{\partial r_{ab}^2} - \frac{1}{r_{ab}} \frac{\partial \rho}{\partial r_{ab}} \right) \frac{r_{abi} r_{abj} r_{abk} r_{abl}}{r_{ab}^2}
\tag{3.36}
$$

$$
B3_{ijkl} = \frac{1}{\Omega} \sum_{a=1}^{N} \frac{\partial^2 F_a}{\partial \rho^2} g_{aij} g_{akl}
\tag{3.37}
$$

The term g_{aij} is equal to

$$g_{aij} = \sum_{b=1, b \neq a} \frac{r_{abi} r_{abj}}{r_{ab}} \frac{\partial \rho}{\partial r_{ab}} = 2 \sum_{b=1, b \neq a} r_{abi} r_{abj} \frac{\partial \rho}{\partial (r_{ab}^2)}. \tag{3.38}$$

Equation (3.38) can be simplified by changing $\rho(r)$ to $\rho(r^2)$. The change in the derivative and the length r cancel.

$$\frac{\partial}{\partial r} = \frac{\partial}{\partial (r^2)} 2r \tag{3.39}$$

This avoids the time-consuming calculation of the length of a vector. The expressions for $B1_{ijkl}$ and $B2_{ijkl}$ are also changed to

$$B1_{ijkl} = \frac{4}{\Omega} \sum_{\substack{a,b=1 \\ a<b}} \frac{\partial^2 V}{\partial (r_{ab}^2)^2} r_{abi} r_{abj} r_{abk} r_{abl} \tag{3.40}$$

and

$$B2_{ijkl} = \frac{4}{\Omega} \sum_{a,b=1} \frac{\partial F_a}{\partial \rho} \frac{\partial^2 \rho}{\partial (r_{ab}^2)^2} r_{abi} r_{abj} r_{abk} r_{abl}. \tag{3.41}$$

3.5 Implementation

As part of this thesis a molecular dynamics code has been programmed from scratch. It is using the C++ programming language.

3.5.1 Tabulated data format in r^2

The molecular dynamics code runs much faster, when the radius-dependent functions are changed from a function of r to a function r^2. The reason is as follows. The functions $V(r)$ and $\rho(r)$ require the calculation of the length $r = \sqrt{x^2 + y^2 + z^2}$ of the vector $\mathbf{r}$, this requires more computation time than the squared length $r^2 = x^2 + y^2 + z^2$.

The force on atom a

$$\mathbf{f}_a = m\ddot{\mathbf{r}}_a = -\frac{\partial E_{\text{tot}}}{\partial \mathbf{r}_a} = -\sum_{i, i \neq a} \left[\left(\frac{\partial F(\rho_a)}{\partial \rho_a} + \frac{\partial F(\rho_i)}{\partial \rho_i} \right) \frac{\partial \phi(r_{ai})}{\partial \mathbf{r}_a} + \frac{\partial V(r_{ai})}{\partial \mathbf{r}_a} \right] \quad (3.42)$$

then simplifies to

$$m\ddot{\mathbf{r}}_a = 2 \sum_{i, i \neq a} \left\{ \left[\frac{\partial F(\rho_a)}{\partial \rho_a} + \frac{\partial F(\rho_i)}{\partial \rho_i} \right] \frac{\partial \rho(r_{ai}^2)}{\partial (r_{ai}^2)} + \frac{\partial V(r_{ai}^2)}{\partial (r_{ai}^2)} \right\} \mathbf{r}_{ai}. \quad (3.43)$$

The potential files for $\rho(r^2)$, $F(\rho)$ and $V(r^2)$ are used in a tabulated format, the square root calculation can, therefore, be moved into the pre-processed tabulated potential data file.

3.5.2 Atom force calculation

In order to speed up the calculation of the force on atom a, only the atoms in the close neighborhood of atom a are considered for force calculation. Each atom has a list of its atom neighbors that is updated every n-th time step. Only atoms that are closer than the cutoff-distance r_{cut} of the potential plus a reserve r_{res} are added to the list. The more often the neighbor list is updated the smaller r_{res} can be.

$$r_{ab} < r_{\text{cut}} + r_{\text{res}} \quad (3.44)$$

In order to accelerate the recalculation of the neighbor lists, the domain of each processor is subdivided into subdomain boxes with a length of a few r_{cut}. Each atom registers with

one of the subdomains. This enables a faster recalculation of the neighbor list, as only the atoms in the boxes around the box where the atom is positioned must be checked. For example, in a 2D case, 9 subdomains must be checked, as seen in Figure 3.10. In the case of a 3D problem 27 subdomains boxes must be searched for neighbors.
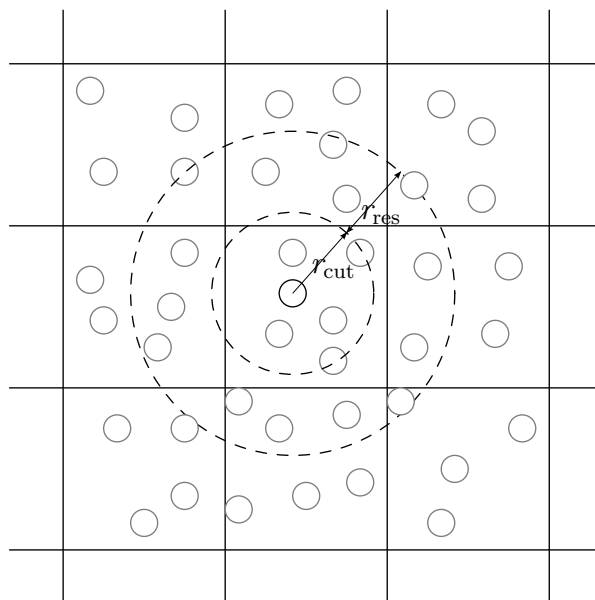
Figure 3.10: Strategy to find atom neighbors

3.5.3 Parallel programming

In order to speed up the molecular dynamics code, OpenMPI was used to enable parallel execution of the code. OpenMPI is an open library implementing the Message Passing Interface (MPI) standard for parallel computing.

The problem space is partitioned into different domains as seen in Figure 3.11. The center domain Ω_9 in the figure is surounded by the domains Ω_1 to Ω_8. The atoms at the domain boundary of Ω_9 (light gray in the figure) are also interacting with the atoms in the boundary of the neighboring domain (dark grey). In order to achieve this, all eight surrounding domains need to pass information about the atoms to the center domain. For the EAM potential this is a two-step synchronization process. First, the atom positions need to be exchanged. The atom positions enable the calculation of the electron density. In a second step, the electron densities are exchanged between the domains. Only with the electron density information, the forces can be calculated. PLIMPTON (1995) outlines an approach with only 4 data exchanges in 2D (6 exchanges in 3D), however, in this work spatial decomposition is implemented with 8 exchanges in 2D (26 in 3D). The reason is simpler programming.
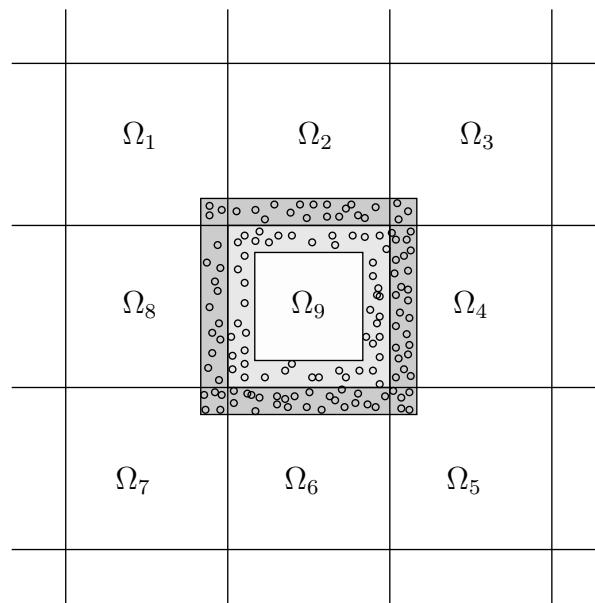
Figure 3.11: MPI data exchange in molecular dynamics

In Figure 3.12 the strong scaling of the code on two different clusters can be seen. The first is an Intel 12 core processor called DaVinci at Caltech and the second is the high performing cluster (HPC) bwUniCluster used by universities in Baden-Württemberg. On both clusters the scaling is very good. With 256 processors on the bwUniCluster the speedup is still around 200.
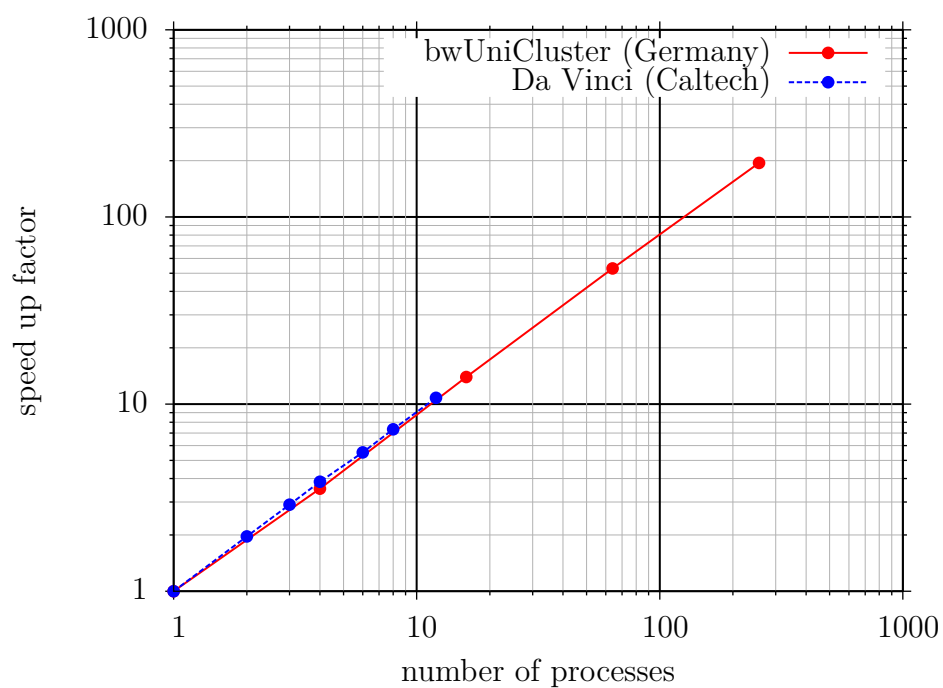
Figure 3.12: Performance of MD code with 2,000,000 atoms on Da Vinci Cluster (Caltech) using up to 12 cores and bwUniCluster (Germany) using up to 256 cores. Strong scaling, 200 time steps. Performance excludes setup time.

4

Continuum mechanics

4.1 From fine scale to coarse scale

As outlined in the previous chapter, matter consists of molecules with empty space between them. However, when simulating a sufficient number of molecules, matter can be treated as a continuum.

Continuum mechanics assumes that material completely fills the space the material occupies. An infinitesimal small space is, therefore, representative of the material at this point. Mechanical problems with a problem size greater than a micrometer can, therefore, be modeled with continuum mechanics. Continuum mechanics is mainly used to fluids and solids. Only solid mechanics will be considered in the following.

The finite element method (FEM) is one method that can be used to discretize the continuum equations. Other methods are for example the finite volume method or the finite difference method. The finite element method was pioneered by M. J. TURNER AND TOPP (1956) and ARGYRIS (1960). A non-linear dynamic finite element formulation is used. For a detailed explanation of the non-linear finite element method, see the book by BELYTSCHKO ET AL. (2000).

4.2 Kinematics

In this work, the total Lagrangian formulation is used, meaning that all calculations are done in a non-moving reference configuration.

A material point P at position $\mathbf{X}$ of the reference configuration is transformed by a function $\chi(\mathbf{X},t)$ to the current configuration

$$\mathbf{x} = \chi(\mathbf{X},t). \tag{4.1}$$

The mapping $\chi(\mathbf{X},t)$ is assumed to be bijective and piecewise continuously differentiable in space at least once and two times differentiable in time. The difference $\mathbf{x}-\mathbf{X}$ is defined as $\mathbf{u}$ as seen in equation 4.2 and visualized in Figure 4.1.

$$\mathbf{x} = \mathbf{X} + \mathbf{u} \tag{4.2}$$
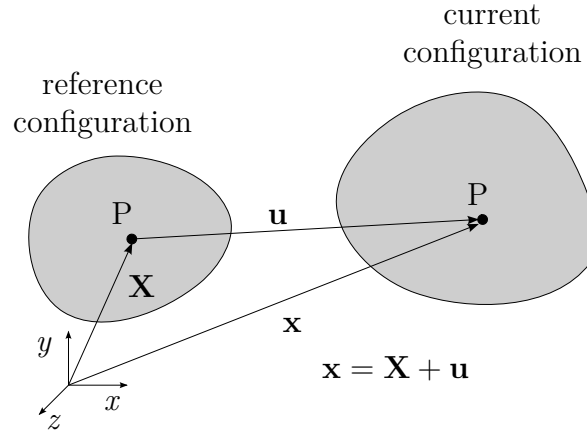
Figure 4.1: Definition of reference and current configuration

The velocity can, therefore, be defined as

$$\mathbf{v} = \dot{\mathbf{x}} = \frac{\partial \mathbf{x}(\mathbf{X},t))}{\partial t} = \frac{\partial(\mathbf{X} + \mathbf{u})}{\partial t} = \frac{\partial \mathbf{u}}{\partial t} = \dot{\mathbf{u}}. \tag{4.3}$$

The definition of the acceleration is analogous.

$$\mathbf{a} = \ddot{\mathbf{u}}. \tag{4.4}$$

An infinitesimal line element $\mathrm{d}\mathbf{X}$ transforms to $\mathrm{d}\mathbf{x}$:

$$\mathrm{d}\mathbf{x} = \underbrace{\frac{\mathrm{d}\mathbf{x}}{\mathrm{d}\mathbf{X}}}_{\mathbf{F}} \mathrm{d}\mathbf{X} \tag{4.5}$$

with $\mathbf{F}$ being the deformation gradient:

$$\mathbf{F} = \frac{d\mathbf{x}}{d\mathbf{X}} = \frac{d(\mathbf{X} + \mathbf{u})}{d\mathbf{X}} = \mathbf{I} + \frac{d\mathbf{u}}{d\mathbf{X}}. \tag{4.6}$$

With the definition of infinitesimal lengths $d\mathbf{X}$, it is possible to define an infinitesimal area $d\mathbf{A}$ as the cross product of two vectors. The area $d\mathbf{A}$ transforms to $d\mathbf{a}$ according to Nanson's formula

$$d\mathbf{a} = \det(\mathbf{F})\mathbf{F}^{-T}d\mathbf{A}. \tag{4.7}$$

The Green Lagrange strain used in this work is defined as

$$\mathbf{E} = \frac{1}{2}(\mathbf{F}^{T}\mathbf{F} - \mathbf{I}). \tag{4.8}$$

4.3 Stress measures

The Cauchy stress or true stress is the relation between the stress vector $\mathbf{t}$ and the normal vector $\mathbf{n}_c$, both of the current configuration.

$$\mathbf{t} = \boldsymbol{\sigma}\mathbf{n}_c. \tag{4.9}$$

Using Nanson's formula, it is possible to define the first Piola-Kirchoff stress tensor $\mathbf{P}$. It relates the true stress vector with the normal vector of the reference configuration $\mathbf{n}_r$:

$$\mathbf{t} = \mathbf{P}\mathbf{n}_r \tag{4.10}$$

with $\mathbf{P} = \det(\mathbf{F})\sigma\mathbf{F}^{-T}$.

The second Piola-Kirchhoff stress is defined as

$$\mathbf{S} = \det(\mathbf{F})\mathbf{F}^{-1}\boldsymbol{\sigma}\mathbf{F}^{-T} \tag{4.11}$$

relating the stress vector of the reference configuration with the normal vector of the reference configuration.

$$\mathbf{T} = \mathbf{S}\mathbf{n}_r \tag{4.12}$$

4.4 Material law

The second Piola-Kirchhoff stress $\mathbf{S}$ is given by a material law that can depend on the Green-Lagrange strain $\mathbf{E}$ and other variables, like the strain-history, temperature or other factors. However, the stress will be limited to a function of strain.

$$\mathbf{S} = \mathbf{S}(\mathbf{E}) \tag{4.13}$$

The material law is non-linear in general. However, often it can be simplified to a linear equation with the material constant $\mathbf{C}$ as linear factor

$$\mathbf{S} = \mathbf{C} \cdot \mathbf{E}. \tag{4.14}$$

In this thesis, the material law at finite element level will be non-linear and the stiffness matrix will not be calculated as it is not necessary for an explicit dynamic simulation. The derivative

$$\mathbf{C} = \frac{\partial \mathbf{S}}{\partial \mathbf{E}} \tag{4.15}$$

at $\mathbf{u} = \mathbf{0}$ will be used later on in this thesis.

In Section 3.4.2, the elasticity tensor is introduced. This elasticity matrix $\mathbf{C}$, being defined by three independent constants C_{11}, C_{12} and C_{44}, is called a cubic material law (CML). Other material laws (e.g. an isotropic material with two independent constants) are not used in this work.

4.5 Balance laws

The continuum momentum balance equation is

$$\rho_m \ddot{\mathbf{u}} - \mathrm{Div}(\mathbf{P}) - \mathbf{b} = 0. \tag{4.16}$$

Here ρ_m is the volumetric mass density, $\mathbf{b}$ is a volumetric force and $\mathbf{P}$ the first Piola-Kirchhoff stress as defined above. This equation is formulated in the reference system. Using the calculus of variations, it is possible to transfer the strong form of this differential equation to its weak form by multiplying it with a test function $\delta \mathbf{u}^{\mathrm{T}}$ and integration over the domain. The variation of the energy of a dynamic system can then be described

according to the following equation

$$\delta\Pi = \int\limits_{\Omega_0} \delta\mathbf{u}^{\mathrm{T}} \left(\rho_m\ddot{\mathbf{u}} - \mathrm{Div}(\mathbf{P}) - \mathbf{b}\right) \mathrm{d}\Omega = 0. \tag{4.17}$$

After partial integration $\delta\Pi$ can be transformed to

$$\delta\Pi = \int\limits_{\Omega_0} \left(\delta\mathbf{u}^{\mathrm{T}}\rho_m\ddot{\mathbf{u}} + \mathrm{Div}(\delta\mathbf{u}^{\mathrm{T}}) - \delta\mathbf{u}^{\mathrm{T}}\mathbf{b}\right)\mathrm{d}\Omega - \int\limits_{\partial\Omega_0} \delta\mathbf{u}^{\mathrm{T}}\mathbf{P}\mathbf{n}_r\mathrm{d}\partial\Omega. \tag{4.18}$$

4.6 Discretization in space

The displacement field is approximated by a different field $\mathbf{u} \approx \mathbf{u}_h$. It is now possible to express the displacement field $\mathbf{u}_h$ as a product of the matrix of shape functions $\mathbf{N}$ and the nodal displacement vector $\mathbf{d}$. For more Details about the matrix $\mathbf{N}$ see Section 4.6.1.

$$\mathbf{u} \approx \mathbf{u}_h = \mathbf{N}\mathbf{d} \tag{4.19}$$

The same is true for the velocity field and the acceleration field

$$\dot{\mathbf{u}} \approx \dot{\mathbf{u}}_h = \mathbf{N}\dot{\mathbf{d}} \tag{4.20}$$

$$\ddot{\mathbf{u}} \approx \ddot{\mathbf{u}}_h = \mathbf{N}\ddot{\mathbf{d}}. \tag{4.21}$$

As the nodal displacement values $\mathbf{d}$ are discrete values, they do not depend on $\mathbf{x}$. $\mathrm{Div}(\delta\mathbf{u}^{\mathrm{T}})$ then is simplified to $\delta\mathbf{d}^{\mathrm{T}}\mathbf{B}_0^{\mathrm{T}}$ with $\mathbf{B}_0 = \mathrm{Div}(\mathbf{N})$. Because in linear FEM the strain is a derivative of the displacements, this $\mathbf{B}_0$ is also called the strain-displacement matrix. However, with the Green-Lagrange strain in nonlinear finite elements, this is not true.

$$\delta\Pi = \int\limits_{\Omega_0} \left(\delta\mathbf{d}^{\mathrm{T}}\mathbf{N}^{\mathrm{T}}\rho_m\mathbf{N}\ddot{\mathbf{d}} + \delta\mathbf{d}^{\mathrm{T}}\mathbf{B}_0^{\mathrm{T}}\mathbf{P}\right)\mathrm{d}\Omega = \int\limits_{\Omega_0} \delta\mathbf{d}^{\mathrm{T}}\mathbf{N}^{\mathrm{T}}\mathbf{b}\mathrm{d}\Omega + \int\limits_{\partial\Omega_0} \delta\mathbf{d}^{\mathrm{T}}\mathbf{N}^{\mathrm{T}}\mathbf{P}\mathbf{n}_r\mathrm{d}\partial\Omega \tag{4.22}$$

Because $\delta\mathbf{d}^{\mathrm{T}}$ is arbitrary, the equation can be simplified to

$$\int\limits_{\Omega_0} \left(\mathbf{N}^{\mathrm{T}}\rho_m\mathbf{N}\ddot{\mathbf{d}} + \mathbf{B}_0^{\mathrm{T}}\mathbf{P}\right)\mathrm{d}\Omega = \int\limits_{\Omega_0} \mathbf{N}^{\mathrm{T}}\mathbf{b}\mathrm{d}\Omega + \int\limits_{\partial\Omega_0} \mathbf{N}^{\mathrm{T}}\mathbf{P}\mathbf{n}_r\mathrm{d}\partial\Omega \tag{4.23}$$

The integrals can then be named as

$$\underbrace{\int\limits_{\Omega_0} \mathbf{N}^{\mathrm{T}} \rho_m \mathbf{N} \mathrm{d}\Omega}_{\mathbf{M}} \ddot{\mathbf{d}} + \underbrace{\int\limits_{\Omega_0} \mathbf{B}_0^{\mathrm{T}} \mathbf{P} \mathrm{d}\Omega}_{\mathbf{f}_{\mathrm{int}}} = \underbrace{\int\limits_{\Omega_0} \mathbf{N}^{\mathrm{T}} \mathbf{b} \mathrm{d}\Omega + \int\limits_{\partial\Omega_0} \mathbf{N}^{\mathrm{T}} \mathbf{P} \mathbf{n}_{\mathrm{r}} \mathrm{d}\partial\Omega}_{\mathbf{f}_{\mathrm{ext}}}. \tag{4.24}$$

$\mathbf{f}_{\mathrm{int}}$ and $\mathbf{f}_{\mathrm{ext}}$ are the internal and external nodal forces, respectively. In addition to these terms, a damping matrix $\mathbf{D}$ is introduced. The damping is a linear combination of the stiffness matrix and the mass matrix

$$\mathbf{D} = c_0 \mathbf{M} + c_1 \mathbf{K}. \tag{4.25}$$

This is also known as Rayleigh damping. Then the equation of motion becomes

$$\mathbf{M}\ddot{\mathbf{d}} = \mathbf{f}_{\mathrm{ext}} - \mathbf{f}_{\mathrm{int}} - \mathbf{D}\dot{\mathbf{d}}. \tag{4.26}$$

The mass matrix $\mathbf{M}$ is a lumped mass matrix, so that the inverse $\mathbf{M}^{-1}$ is just inverting every main diagonal entry.

$$\ddot{\mathbf{d}} = \mathbf{M}^{-1} \left(\mathbf{f}_{\mathrm{ext}} - \mathbf{f}_{\mathrm{int}} - \mathbf{D}\dot{\mathbf{d}} \right) \tag{4.27}$$

4.6.1 Hexahedron element

In the following, we limit ourselves to the hexahedron element with trilinear shape functions as this is the only finite element used in this work. The element has eight nodes and is shown in Figure 4.2. The displacement vector $\mathbf{u}$ is interpolated from the nodal displacements $\mathbf{d}$ with the help of shape functions in the matrix $\mathbf{N}$.

$$\mathbf{u}_h = \mathbf{N}\mathbf{d} \tag{4.28}$$

The matrix $\mathbf{N}$ has the dimensions 3x24 and consists of the shape functions

$$\mathbf{N} = \begin{bmatrix} N_1 & 0 & 0 & N_2 & 0 & 0 & \cdots & N_8 & 0 & 0 \\ 0 & N_1 & 0 & 0 & N_2 & 0 & \cdots & 0 & N_8 & 0 \\ 0 & 0 & N_1 & 0 & 0 & N_2 & \cdots & 0 & 0 & N_8 \end{bmatrix} \tag{4.29}$$

The shape functions for a trilinear hexahedron element are

$$N_i(\xi,\eta,\zeta) = \frac{1}{8}(1 \pm \xi)(1 \pm \eta)(1 \pm \zeta) \tag{4.30}$$

The shape functions are not defined in the real coordinate system but in the element coordinate system in the (ξ,η,ζ)-space. Each shape functions is equal to one in one of the eight corners $(\pm 1,\pm 1,\pm 1)$ and zero in all the other corners. The nodal numbering and the nodal coordinates can be seen in Figure 4.2.
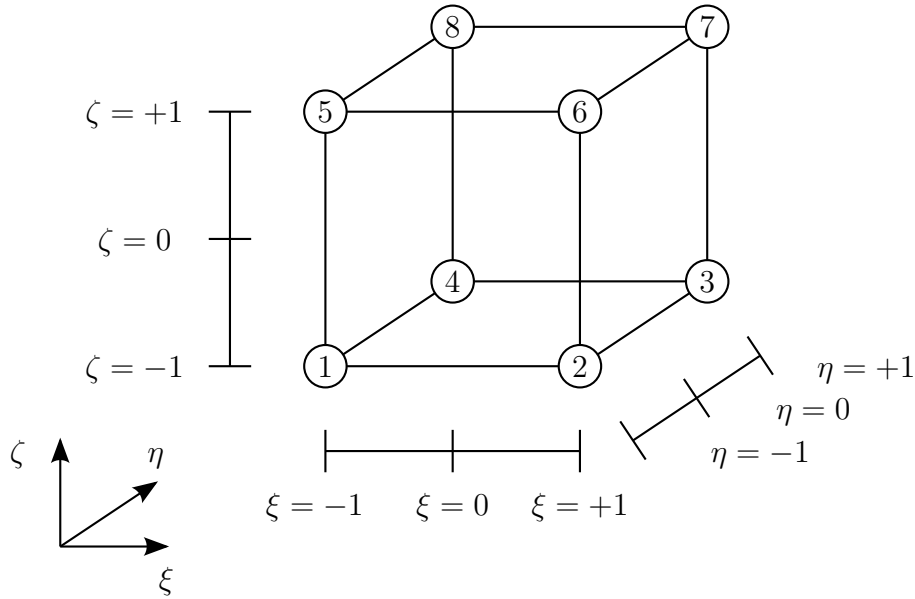
Figure 4.2: Node numbering of a hexahedron element

The Jacobian is

$$\mathbf{J} = \begin{bmatrix} \frac{\partial x}{\partial \xi} & \frac{\partial x}{\partial \eta} & \frac{\partial x}{\partial \zeta} \\ \frac{\partial y}{\partial \xi} & \frac{\partial y}{\partial \eta} & \frac{\partial y}{\partial \zeta} \\ \frac{\partial z}{\partial \xi} & \frac{\partial z}{\partial \eta} & \frac{\partial z}{\partial \zeta} \end{bmatrix}. \tag{4.31}$$

The matrix $\mathbf{B}_0$ is the matrix product of the differential operator $\mathbf{L_X}$ and the matrix of shape functions $\mathbf{N}$.

$$\mathbf{B}_0 = \mathbf{L_X N} \tag{4.32}$$

The matrix $\mathbf{B}_0$ contains the derivatives of the shape function with respect to the reference coordinate system $\mathbf{X}$ as seen in equation (4.33).

$$\mathbf{B}_0 = \begin{bmatrix} N_{1,\mathbf{X}} & 0 & 0 & N_{2,\mathbf{X}} & 0 & 0 & \ldots & N_{8,\mathbf{X}} & 0 & 0 \\ 0 & N_{1,\mathbf{Y}} & 0 & 0 & N_{2,\mathbf{Y}} & 0 & \ldots & 0 & N_{8,\mathbf{Y}} & 0 \\ 0 & 0 & N_{1,\mathbf{Z}} & 0 & 0 & N_{2,\mathbf{Z}} & \ldots & 0 & 0 & N_{8,\mathbf{Z}} \\ 0 & N_{1,\mathbf{Z}} & N_{1,\mathbf{Y}} & 0 & N_{2,\mathbf{Z}} & N_{2,\mathbf{Y}} & \ldots & 0 & N_{8,\mathbf{Z}} & N_{8,\mathbf{Y}} \\ N_{1,\mathbf{Z}} & 0 & N_{1,\mathbf{X}} & N_{2,\mathbf{Z}} & 0 & N_{2,\mathbf{X}} & \ldots & N_{8,\mathbf{Z}} & 0 & N_{8,\mathbf{X}} \\ N_{1,\mathbf{Y}} & N_{1,\mathbf{X}} & 0 & N_{2,\mathbf{Y}} & N_{2,\mathbf{X}} & 0 & \ldots & N_{8,\mathbf{Y}} & N_{8,\mathbf{X}} & 0 \end{bmatrix} \tag{4.33}$$

However, the shape functions are functions of (ξ, η, ζ), so the derivatives need to be expanded

$$N_{1,\mathbf{X}} = \frac{\partial N_1}{\partial \xi} \frac{\partial \xi}{\partial X} + \frac{\partial N_1}{\partial \eta} \frac{\partial \eta}{\partial X} + \frac{\partial N_1}{\partial \zeta} \frac{\partial \zeta}{\partial X} \tag{4.34}$$

The inverse derivate at a specific point can be obtained by inverting the Jacobian $\mathbf{J}$ at this point.

$$\mathbf{J}^{-1} = \begin{bmatrix} \frac{\partial \xi}{\partial x} & \frac{\partial \xi}{\partial y} & \frac{\partial \xi}{\partial z} \\ \frac{\eta}{\partial x} & \frac{\partial \eta}{\partial y} & \frac{\eta}{\partial z} \\ \frac{\partial \zeta}{\partial x} & \frac{\partial \zeta}{\partial y} & \frac{\partial \zeta}{\partial z} \end{bmatrix}. \tag{4.35}$$

The integral to calculate the internal nodal forces can then be transformed to

$$\mathbf{f}_{\text{int}} = \int\limits_{-1}^{1} \int\limits_{-1}^{1} \int\limits_{-1}^{1} \mathbf{B}_0^{\mathrm{T}} \mathbf{P} |\mathbf{J}| \mathrm{d}\xi \mathrm{d}\eta \mathrm{d}\zeta = \Omega_0 \sum_{i=1}^{8} \omega_i \mathbf{B}_0^{\mathrm{T}} \mathbf{P} |\mathbf{J}|. \tag{4.36}$$

4.6.2 Selective reduced integration of internal nodal forces

In order to reduce shear locking the internal nodal forces are separated into four different integrals. Reduced integration has been pioneered by ZIENKIEWICZ ET AL. (1971).

$$\mathbf{f}_{\text{int}} = \int\limits_{\Omega_0} \mathbf{B}_0^{\mathrm{T}} \mathbf{P} \mathrm{d}\Omega = \underbrace{\int\limits_{\Omega_0} \mathbf{B}_{01}^{\mathrm{T}} \mathbf{P} \mathrm{d}\Omega}_{\mathbf{f}_{\text{int},1}} + \underbrace{\int\limits_{\Omega_0} \mathbf{B}_{02}^{\mathrm{T}} \mathbf{P} \mathrm{d}\Omega}_{\mathbf{f}_{\text{int},2}} + \underbrace{\int\limits_{\Omega_0} \mathbf{B}_{03}^{\mathrm{T}} \mathbf{P} \mathrm{d}\Omega}_{\mathbf{f}_{\text{int},3}} + \underbrace{\int\limits_{\Omega_0} \mathbf{B}_{04}^{\mathrm{T}} \mathbf{P} \mathrm{d}\Omega}_{\mathbf{f}_{\text{int},4}} \tag{4.37}$$

With the **B**-Operator

$$\mathbf{B} = \begin{bmatrix} \mathbf{B}_1 \\ \mathbf{B}_2 \\ \mathbf{B}_3 \\ \mathbf{B}_4 \\ \mathbf{B}_5 \\ \mathbf{B}_6 \end{bmatrix} = \underbrace{\begin{bmatrix} \mathbf{B}_1 \\ \mathbf{B}_2 \\ \mathbf{B}_3 \\ 0 \\ 0 \\ 0 \end{bmatrix}}_{\mathbf{B}_{01}} + \underbrace{\begin{bmatrix} \mathbf{B}_1 \\ \mathbf{B}_2 \\ \mathbf{B}_3 \\ \mathbf{B}_4 \\ 0 \\ 0 \end{bmatrix}}_{\mathbf{B}_{02}} + \underbrace{\begin{bmatrix} 0 \\ 0 \\ 0 \\ 0 \\ \mathbf{B}_5 \\ 0 \end{bmatrix}}_{\mathbf{B}_{03}} + \underbrace{\begin{bmatrix} 0 \\ 0 \\ 0 \\ 0 \\ 0 \\ \mathbf{B}_6 \end{bmatrix}}_{\mathbf{B}_{04}} \tag{4.38}$$

The normal part $\mathbf{f}_{\text{int},1}$ is integrated with 2x2x2 Gauss points at $(\xi = \pm\sqrt{\frac{1}{3}}, \eta = \pm\sqrt{\frac{1}{3}}, \zeta = \pm\sqrt{\frac{1}{3}})$, the shear parts with two Gauss points each. $\mathbf{f}_{\text{int},2}$ is integrated at $(\xi = \pm\sqrt{\frac{1}{3}}, \eta = 0, \zeta = 0)$, $\mathbf{f}_{\text{int},3}$ is integrated at $(\xi = 0, \eta = \pm\sqrt{\frac{1}{3}}, \zeta = 0)$ and $\mathbf{f}_{\text{int},4}$ is integrated at $(\xi = 0, \eta = 0, \zeta = \pm\sqrt{\frac{1}{3}})$. The Gauss points are illustrated in Figure 4.3 for better understanding.
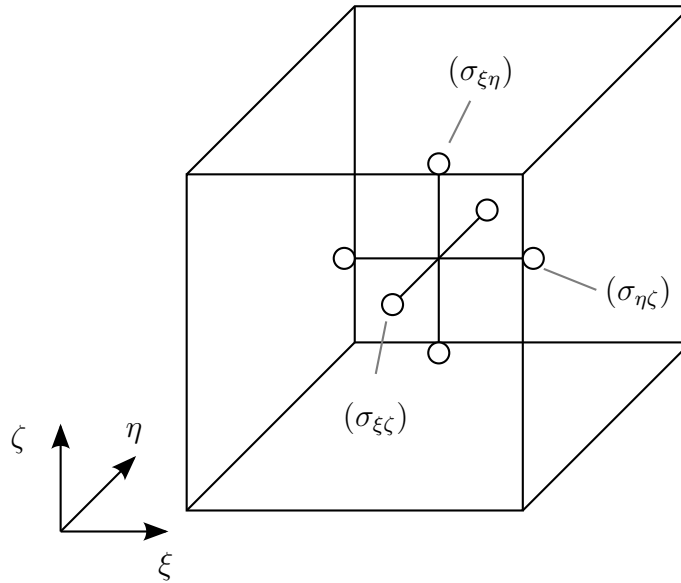
Figure 4.3: Gauss points for the integration of shear forces

4.7 Discretization in time

A typical second-order differential equation of a dynamic system is given in equation.

$$\mathbf{M}\ddot{\mathbf{d}} + \mathbf{D}\dot{\mathbf{d}} + \mathbf{f}_{\text{int}} - \mathbf{f}_{\text{ext}} = 0. \tag{4.39}$$

$$\mathbf{M}\ddot{\mathbf{d}} = \mathbf{f}_{\text{ext}} - \mathbf{D}\dot{\mathbf{d}} - \mathbf{f}_{\text{int}} = \mathbf{f}_{\text{tot}}. \tag{4.40}$$

In explicit dynamic computation the calculation of the stiffness matrix is not necessary as the internal nodal forces $\mathbf{f}_{\text{int}}(\mathbf{d})$ are sufficient, which depend on the displacement $\mathbf{d}$ of the nodes. In this work, the stiffness matrix is only necessary for the estimation of the critical finite element time step and not for the simulation itself. The calculation of the maximum possible time step is left to the literature, see e.g. the book by BELYTSCHKO ET AL. (2000).

Time integration is done with the central difference method, which is a well-known method for time integration. The flow chart can be seen in Figure 4.4 and is taken from BELYTSCHKO ET AL. (2000).

1. $\mathbf{d} = \mathbf{d}_0$, $\dot{\mathbf{d}} = \dot{\mathbf{d}}_0$, $t = t_0$

2. Calculate $\mathbf{f}_{\text{tot,n}}$

3. Compute acceleration $\ddot{\mathbf{d}}_n = \mathbf{M}^{-1}\mathbf{f}_{\text{tot,n}}$

4. time update $t_{n+1} = t_n + \Delta t$

5. update velocity $\dot{\mathbf{d}}_{n+1/2} = \dot{\mathbf{d}}_n + \frac{\Delta t}{2}\ddot{\mathbf{d}}_n$

6. update displacement vector $\mathbf{d}_{n+1} = \mathbf{d}_n + \Delta t \dot{\mathbf{d}}_{n+1/2}$

7. Calculate $\mathbf{f}_{\text{tot,n+1}}$

8. Compute acceleration $\ddot{\mathbf{d}}_{n+1} = \mathbf{M}^{-1}\mathbf{f}_{\text{tot,n+1}}$

9. update velocity $\dot{\mathbf{d}}_{n+1} = \dot{\mathbf{d}}_{n+1/2} + \frac{\Delta t}{2}\ddot{\mathbf{d}}_{n+1}$

10. Update time step counter to $n + 1$

11. Output

12. if $t_{n+1} < t_{\text{end}}$ goto step 4

Figure 4.4: Flowchart for time integration with the central difference method

5

Multiscale simulation

5.1 General overview

The term "multiscale" implies that a physical phenomenon is influenced by different scales in space and/or time. The phenomenon cannot be described accurately by just using one scale in time and space. The number of different scales is in general not limited, but often only two scales are of interest, which in general are referred to as fine scale and coarse scale. The advantage of the coarse scale is that problems with big time scales or large sizes can be simulated with less effort than on the fine scale. However, on the fine scale a specific physical behavior may be more correctly modeled with a first principles approach instead of using fitted parameters.

There are two ways to look at multiscale methods. The sequential approach and the concurrent approach. The sequential approach means, that the different methods are done in sequence, so the fine scale simulation results are used as input for the coarse scale simulation. There is no feedback to the fine scale. A very simple example is 1D-elasticity. The Young's modulus of a metal can be derived from molecular dynamics or another simulation method. The derived material law

$$\sigma = E\varepsilon \tag{5.1}$$

can then be applied to finite element simulation of large steel bridges or other parts of different length scale. From this example it is easy to see that sequential multiscale simulation has been done for decades.

Concurrent multiscale modelling means that fine and coarse scale are simulated at the same time. Information is passed from one scale to another. These methods are almost exclusively to be used on a computer because the computational power and memory

requirements are high. In many cases, even parallel computing on supercomputers is required to achieve a reasonable run time.

Within the concurrent multiscale modeling, there is a further subdivision into two categories, referring to the spatial breakdown of the scales. The fine scale and the coarse scale can be simulated on the same domain in a hierarchical way or the domain is split into two domains, where one part is the fine scale, while the other is the coarse scale, see also Figure 5.1.
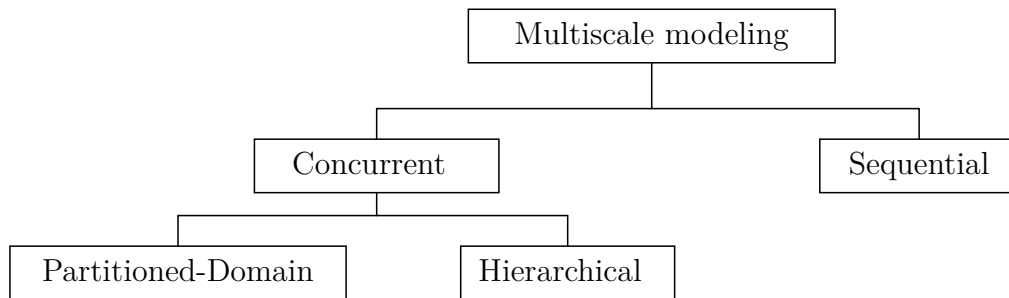
Figure 5.1: General overview multiscale modeling, as seen by Tadmor and Miller (2011), page 540

Sequential multiscale modeling is not a topic of this thesis, for further information see the book by Schmauder and Schäfer (2016) or by Phillips (2001).

5.2 Hierarchical methods

Hierarchical methods typically make use of a fine scale model and a coarse scale model. The fine scale model typically uses a representative volume element (RVE) with periodic boundary conditions. In addition, the fine scale and coarse scale are also not in the same time scale. It is assumed that the fine scale converges to changes in the coarse scale almost instantaneously. The fine scale solution does not depend for example on the rate of deformation on the coarse scale. It is, therefore, possible to run the fine scale model for a limited amount of steps to average state parameters at fine scale level. During this averaging process the coarse scale time is frozen. The derived quantities (e.g. stress, elastic constants) are then transferred to the coarse scale. In most cases, this procedure, which is also called homogenization, is used in a continuum-to-continuum coupling, see e.g. Geers et al. (2010), Feyel (2003). The hierarchical coupling of continuum mechanics and atomistics is rare in literature although a few examples exist.

A very old hierarchical method – that is coupling atomistics and continuum theory – is the Cauchy-Born method. It is based on ideas from Cauchy (see Cauchy (1828b), Cauchy (1828a)) and was later modified by Born (see Born (1923) and Born and

HUANG (1954)). It was developed before the word "multiscale" was adopted. It assumes that the movement of atoms in a solid can be derived from a macroscale material point: the deformation of the atoms is the same as the macroscopic deformation. The material properties can then be calculated at the fine scale and used for the macroscale simulation. Born included sublattice shifts and temperature effects into the model by Cauchy. The position of an atom a is described by

$$\mathbf{r}_a = \mathbf{FR}_a + \mathbf{s} + \mathbf{w}(t). \tag{5.2}$$

r_a is the current position of the atom, $\mathbf{F}$ is the coarse scale deformation gradient, R_a is the initial atom position, $\mathbf{s}$ is the sublattice shift and $\mathbf{w}(t)$ are the time-dependent thermal fluctuations. The Cauchy rule is only the first part, namely $\mathbf{r}_a = \mathbf{FR}_a$.

The first multiscale methods, that called themselves multiscale, were used in the context of simulation of the atmospheres of stars and later the Earth, see e.g. GRABOWSKI AND SMOLARKIEWICZ (2002). The coarse scale in this method is the atmospheric flow, while the fine scale are individual clouds.

Another recent hierarchical multiscale methods deals with electron transport in molecular dynamics. Because electrons are not modeled explicitly, rapid heat transfer in e.g. laser ablation cannot be modeled accurately. WAGNER ET AL. (2008) have developed a method, that superimposes a finite element mesh over the molecular dynamics region that takes care of heat transfer.

A well known hierarchical method is the heterogeneous multiscale method (HMM), see E AND ENGQUIST (2003) or the FE²-method (FEYEL (2003)). Both methods are similar to each other. The FE²-method obviously refers to finite element squared, meaning that there are finite elements below the finite elements. A coarse scale finite element mesh is extended by several submeshes with periodic boundary conditions. These submeshes are evaluated at several points in the coarse scale mesh to deliver additional constitutive information. The evaluation points can for example be Gauss points as these points are needed anyways for integration of the stiffness matrix.

Another hierarchical method has been presented by TADMOR ET AL. (2000) to develop a model of plasticity using atomic-scale simulation, dislocation dynamics and crystal plasticity theory.

ULZ (2015) presented a way to couple finite elements and molecular dynamic using the heterogeneous multiscale method, which is similar to the FE²-concept. He used a kernel by CANCÈS ET AL. (2004) of the form

$$K(t) = \alpha_k t^{k-1}(1-t)^k \tag{5.3}$$

for the averaging of the microscale data. The kernel weights in the middle of the interval higher than at the boundaries. On the macroscale, the problem was solved with the non-linear static finite element method. It is not specified in the paper whether any locking-free formulations in the finite element method have been used.

In this work, a method similar to the method used by Ulz will be used – motivated by the FE^2 concept. This concept is then used to integrate phase transformation into the finite element method.

Disadvantages of the hierarchical approach are the high computational cost due to the many subproblems and/or the statistical error at the fine scale. As the parameters at the fine scale need to be averaged over a time frame, the signal-to-noise ratio needs to be high for fast computation of the essential parameters.

5.3 Partitioned-domain methods

Partitioned domain methods are more widely in use than hierarchic methods. The domain/space is divided into different areas where different theories are used. For example one region could be using molecular dynamics while another region could use continuum mechanics. The big question with partitioned-domain multiscale simulation is how to manage the transition from one domain to another.

The first partitioned-domain method was the FEAt model by Kohlhoff et al. (1991). In the last decades many methods have been developed. They can be separated into energy-based methods and force-based methods.

5.3.1 Energy-based methods

Energy-based multiscale methods are derived from a single potential energy function that is composed of the sum of the three individual energies

$$\Pi_{\text{tot}} = \Pi_{\text{coarse}} + \Pi_{\text{fine}} + \Pi_{\text{handshake}}. \tag{5.4}$$

The three sums are the energy of the coarse scale region Π_{coarse}, the energy of the fine scale region Π_{fine} and the energy of the handshake region $\Pi_{\text{handshake}}$ (if present).

In the following four methods shall be explained in more detail.

Quasicontinuum method

The quasicontinuum method by TADMOR ET AL. (1996) divides the domain into two parts. One part is the fine scale with atoms called "local" repatoms (representative atoms). The other part is the coarse scale with atoms called "nonlocal" repatoms and atoms that move according to the nonlocal repatoms. The expression "local" repatoms is used for atoms that are treated in a molecular way and "nonlocal" repatoms are selected atoms in the coarse scale area, which define the motion of the remaining atoms in the coarsefield according to the Cauchy rule. In the next step triangles are constructed from the repatoms. These triangles control the motion of the atoms within. For a visual description see Figure 5.2.
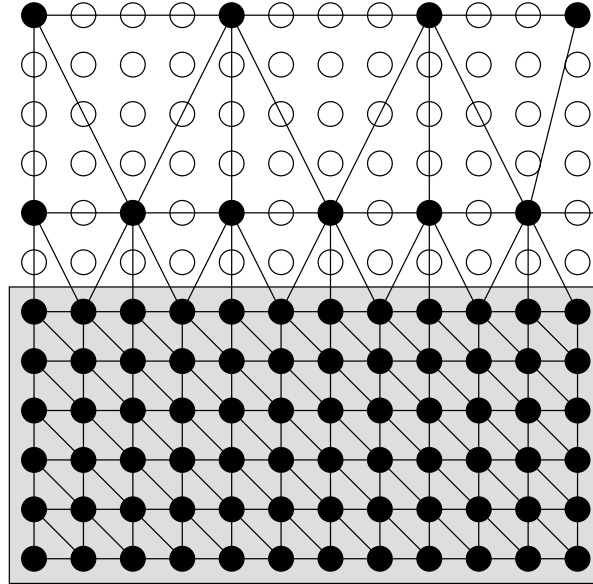
Figure 5.2: General overview of the quasicontinuum method. Repatoms in black, other atoms in white. The shaded region is the atomistic part and the unshaded region is the continuum region

The internal energy of the quasicontinuum is

$$\Pi_{\text{int}}(\mathbf{u}) = \sum_{a \in \text{all atoms}} \Pi_a(\mathbf{u}) = \sum_{a \in \text{atom region}} \Pi_a(\mathbf{u}) + \sum_{a \in \text{ coarse scale}} \Pi_a(\mathbf{u}). \tag{5.5}$$

The second sum can be replaced by a sum over all finite elements

$$\sum_{a \in \text{ coarse scale}} \Pi_a(\mathbf{u}) = \sum_{e \in \text{ coarse scale}} \nu_e \Omega_0 \, W(\mathbf{F}(\mathbf{u})) \tag{5.6}$$

where ν_e is the number of atoms in the finite element, Ω_0 is the Wigner-Seitz volume (the volume associated with an atom) in the reference configuration and W is the strain energy function.

The QC method is often used in literature and has been used with an adaptive mesh refining technique (K. DATTA ET AL. (2004), ARNDT AND LUSKIN (2008)).

Cluster-based quasicontinuum method

The cluster-based quasicontinuum method (CQC-E) (see e.g. EIDEL AND STUKOWSKI (2009)) is a method that builds on the quasicontinuum method. The idea is to only use the atoms surrounding the repatoms to calculate the energy of the triangle as seen in Figure 5.3. The energy of the atoms that are not close to the repatoms is approximated with information from those atoms close to the repatoms. These cluster surrounding the repatoms can differ in size, with bigger clusters resulting in a higher accuracy but also higher computational effort.
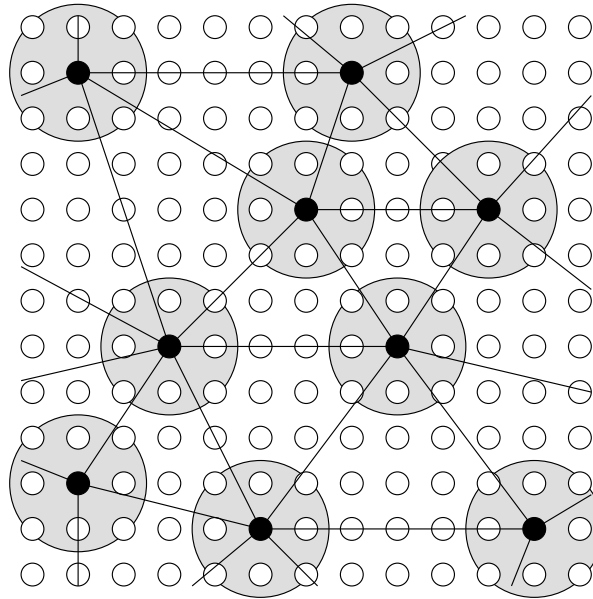
Figure 5.3: Overview cluster-based quasicontinuum method method

Bridging domain method

The bridging domain method (XIAO AND BELYTSCHKO (2004)) introduces a handshake region B_H that smoothes the transition from the fine scale to the coarse scale. This is

achieved by a blended energy potential, where in the handshake region the potential Π_H is blended from one potential to another by the following equation

$$\Pi_H = \sum_{a \in B_H} (1 - \Phi(\mathbf{x}))\Pi_a(\mathbf{u}) + \sum_{e \in B_H} \nu_e \Omega_0 \, W(\mathbf{F}(\mathbf{u}))\Phi(\mathbf{x}). \tag{5.7}$$

It is based on the Arlequin method (BAUMAN ET AL. (2008)).

Bridging scale method

The bridging scale method (see WAGNER AND LIU (2003), QIAN ET AL. (2004)) is different from the previous methods and separates the displacement field $\mathbf{u}$ in two contributions

$$\mathbf{u} = \mathbf{u}' + \mathbf{u}''. \tag{5.8}$$

$\mathbf{u}'$ is the coarse field displacement and $\mathbf{u}''$ the fine scale displacement. The two displacement fields exist in the whole domain. However, the fine scale displacements are assumed to be zero everywhere except for the atomistic region. The reason is that the zero Kelvin atom position is assumed to be homogeneous and defined by the coarse scale. Figure 5.4 shows the domain of the method.
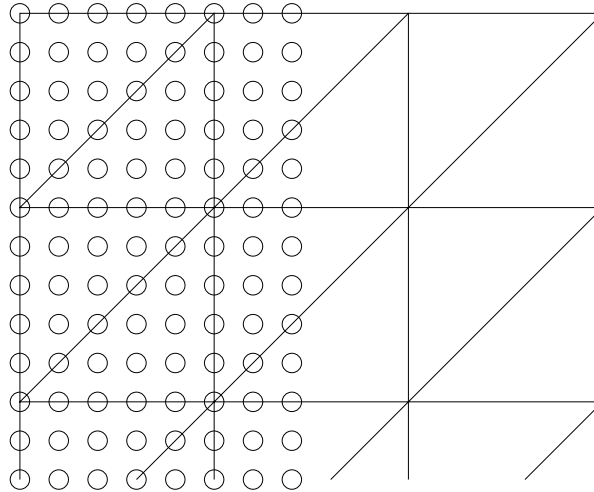
Figure 5.4: Overview bridging scale method

5.3.2 Ghost forces

A problem with energy-based methods is that most energy-based methods – or maybe even all as claimed by TADMOR AND MILLER (2011) pp. 621 – suffer from ghost

forces. Ghost forces arise from the conflict between the nonlocal molecular dynamics and the local continuum mechanics. An atom does interact with all other atoms, while a premise of continuum mechanics is that the state of a material point is fully defined by the deformation at that point. Therefore, in the finite element method, the finite elements only interact with their surrounding neighbor elements.

A simple example can be seen in Figure 5.5. On the left there are four black atoms, with the center atom being a finite element node at the same time. The energy of the system can be written as the sum of the atomic energy and the continuum energy.

$$\Pi_{\text{int}}(\mathbf{u}) = \sum_{a \in \text{all atoms}} \Pi_a(\mathbf{u}) = \sum_{a \in \text{atom region}} \Pi_a(\mathbf{u}) + \sum_{a \in \text{ coarse scale}} \Pi_a(\mathbf{u}). \tag{5.9}$$

From the energy, the forces on the individual atoms can be derived. The force derived from the total energy on the atom to the left of the center is non-zero, even in equilibrium position. In order to deal with this problem, a number of ghost force correction methods have been developed. This is explained in more detail in TADMOR AND MILLER (2011). Another way to deal with ghost forces is discussed in AMELANG ET AL. (2015).

atoms   finite element nodes

interface
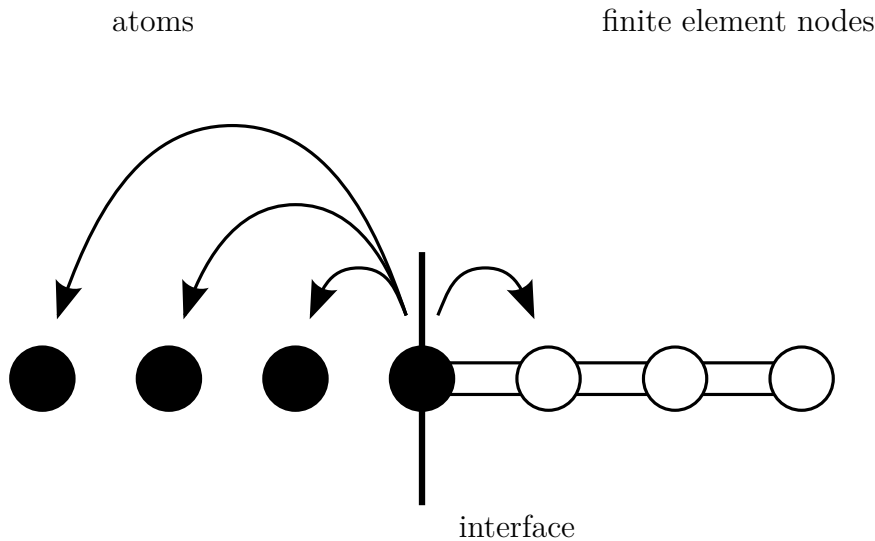
Figure 5.5: Explanation of ghost forces. The black sphere in the center is both a finite element node and an atom. To the left it interacts with three atoms, while on the right it interacts only with the nearest finite element node

If forces are not derived from an energy potential, the forces can be designed to be zero in equilibrium position. These are called force-based methods and are outlined in section 5.3.3.

5.3.3 Force-based methods

Force-based methods directly use the force equilibrium to construct a way to calculate the forces on atoms and finite element nodes. The forces are not derived from a single energy potential. However, this method is not without disadvantage. As the forces are not derived from an energy potential, it is not known whether the solution is actually physically correct and it is unknown which energy function is actually minimized.

Force-based methods eliminate ghost forces by enforcing that the forces are all zero in the equilibrium state. In order to achieve this, two independent potentials Π_1 and Π_2 are used. The force on the atoms is then defined as

$$\mathbf{f}_a = -\frac{\partial \Pi_1}{\partial \mathbf{r}_a} \tag{5.10}$$

and the force on finite element node I is

$$\mathbf{f}_I = -\frac{\partial \Pi_2}{\partial \mathbf{u}_I}. \tag{5.11}$$

This is not the same as minimizing the combined potential $\Pi_1 + \Pi_2$. However, when not in equilibrium, there are still spurious forces present in force-based methods similar to ghost forces in energy-based methods.

Atomistic-to-continuum method

One method is the Atomistic-to-continuum method (AtC, see e.g. FISH ET AL. (2007) or BADIA ET AL. (2007)). It is a force-based version of the bridging domain method. This method starts with the assumption that atoms and nodes are completely uncoupled and the forces on the atoms and finite elements are as in the standard formulation of each theory

$$\mathbf{f}_a = -\frac{\partial \Pi_{\text{atoms}}}{\partial \mathbf{r}_a} \tag{5.12}$$

and the force on finite element node I

$$\mathbf{f}_I = -\sum_{e=1}^{n_{\text{ele}}} \int_{\Omega_0} \mathbf{B}_0^{\text{T}} \mathbf{P} \mathrm{d}\Omega. \tag{5.13}$$

It is then assumed that the atoms in the finite elements are constrained to follow the displacements of the finite element nodes. Their position is interpolated with the finite element shape functions. In addition, the forces on the atoms inside the handshake

region are projected to the finite element nodes. The AtC method is in a variation later used in the horizontal coupling (see Chapter 6.3).

Further reading

There are other methods that are only mentioned by name here. The reader is referred to additional literature for more information. One method is the Coupled Atom Discrete Dislocation Dynamics (CADD) method used by SHILKROT ET AL. (2002) and SHILKROT ET AL. (2004) to simulate plasticity in a multiscale environment. It is based on the FEAt-method (KOHLHOFF ET AL. (1991)). Other method include the hybrid simulation method (LUAN ET AL. (2006)) or the cluster based-quasicontinuum, which was originally force-based (KNAP AND ORTIZ (2001)).

TADMOR AND MILLER (2011) did a comparison of multiple multiscale methods and found that the quasicontinuum method (with ghost force correction) and the hybrid simulation method offered the highest accuracy at the lowest computational cost.

In general the benchmarking, validation and reproducibility of concurrent multiscale methods is still lacking as stated by TADMOR AND MILLER (2017). The results depend a lot on the implementation in actual program code.

5.3.4 Finite temperature

An important challenge is the modelling of materials at non-zero / finite temperature. Vibration of the atoms around the equilibrium position represents a specific temperature. The dynamics of an atomistic system is, therefore, composed of the dynamic nature of the atomic vibration and the movement and vibration at lower frequencies. The continuum region, however, does not know temperature related vibration; temperature is simply a material state parameter. This fundamental difference results in a number of challenges related to finite temperature multiscale simulation. The temperature vibrations are supposed to stay in the atomic region, but in reality will excite the continuum region. Another challenge are wave reflections at the atomistic-continuum interface.

Multiscale simulation at finite temperature can be separated into two problem groups

1. Problem to find the equilibrium of a system at finite temperature

2. Study of dynamic phenomena at finite temperature

The first problem is easier than the second problem. For the first problem the Hot-Quasicontinuum method (DUPUY et al. (2005), KNAP AND ORTIZ (2001)) has been developed. However, the Hot-QC does not resolve atomic vibrations but instead uses statistical methods to estimate temperature related effects like thermal strain.

5.4 Investigation of existing methods regarding phase transformation

What are the requirements of a method that can simulate phase transformation? If we look back at Section 2.3, we can summarize it as follows

1. Phase transformation is a temperature related phenomenon. The method must be able to deal with temperature.

2. Phase transformation is a change in the lattice structure. Molecular dynamics will be able to simulate this, if the potential supports it.

3. The rearrangement of the lattice structure should not be constrained in the interface area.

4. Phase transformation should also be supported by the coarse scale with the same deformation behavior as in the fine scale. Otherwise, all areas that are supposed to change phase have to be adaptively modified to be atoms.

5. Phase transformation is a dynamic phenomenon.

We now take another look at the existing methods regarding phase transformation. In the case of the hierarchical concept, the phase transformation can be easily implemented in a molecular dynamics subproblem as it can be modeled with only a small number of atoms. It is, therefore, suitable for phase transformation. The quasicontinuum and cluster-based methods constrain the movement of the atoms to the movement of the repatoms with the Cauchy rule. However, the Cauchy method assumes that the coarse scale deformation is equal to the fine scale deformation. There is no additional degree of freedom that allows for the possibility of a topology change regarding the atoms bound by the Cauchy rule. Therefore, the state parameters derived from the atomic structure cannot take phase transformation into account. The same is true for the bridging domain and the bridging scale method. The atomistic-to-continuum method is a force-based method and, therefore, the separation of atomistic and finite element modeling with different potentials enables the method to include the hierarchical concept in the coarse scale part (that can do phase transformation). In the interface region a new concept must be developed. Moreover, most multiscale methods for finite temperature ignore

the dynamic nature of temperature related vibrations and use a statistical approach to treat it – if at all. This is another problem with many existing methods.

In this thesis a hierarchical method (called "vertical coupling") and a domain partitioning method similar to the AtC-method (called "horizontal coupling") will be used to create a hierarchic-partitioned-domain method. This is described in the next chapter.

<div align="right">

6

</div>

A combined hierarchic-partitioned-domain method

6.1 Overview

As a starting point we recap the last chapter. A multiscale method for phase transformation has a number of requirements, namely phase transformation in the continuum region and in the atomistic region and at the interface. For the coarse scale (in this case the finite element method) this means, that the material law must be able to change phase, which is not an easy requirement. While there have been material laws developed that can do phase transformation (see e.g. GOVINDJEE AND MIEHE (2001)), the material law must also show the same behavior as the atomistic part of the domain (molecular dynamics). It is, therefore, prudent to use molecular dynamics not only in the atomistic domain but also in a hierarchical way – similar to the FE²-method or HMM – as a material law for the finite elements. Small subproblems consisting of a few hundred atoms – enough to simulate phase transformation – are used as finite element material law. This method is called vertical coupling in this thesis. The transition area is modeled with the AtC method without handshake for reference and with a new idea, where the coupling atoms are not strongly bound to the finite element nodal movement but have additional freedom as outlined in Section 6.3. This is called horizontal coupling in this thesis.

The overall concept can be seen in Figure 6.1, for simplicity reasons the illustration is limited to 2D. The figure shows two quadrilateral finite elements (red) with four Gauss integration points in each element. In addition, on the right side a number of atoms (blue) can be seen. Some atoms are overlapping with the finite elements, these atoms are somehow bound to the finite element movement as explained later in Section 6.3. The other atoms are moving freely and interact with all other atoms. Not visible in the
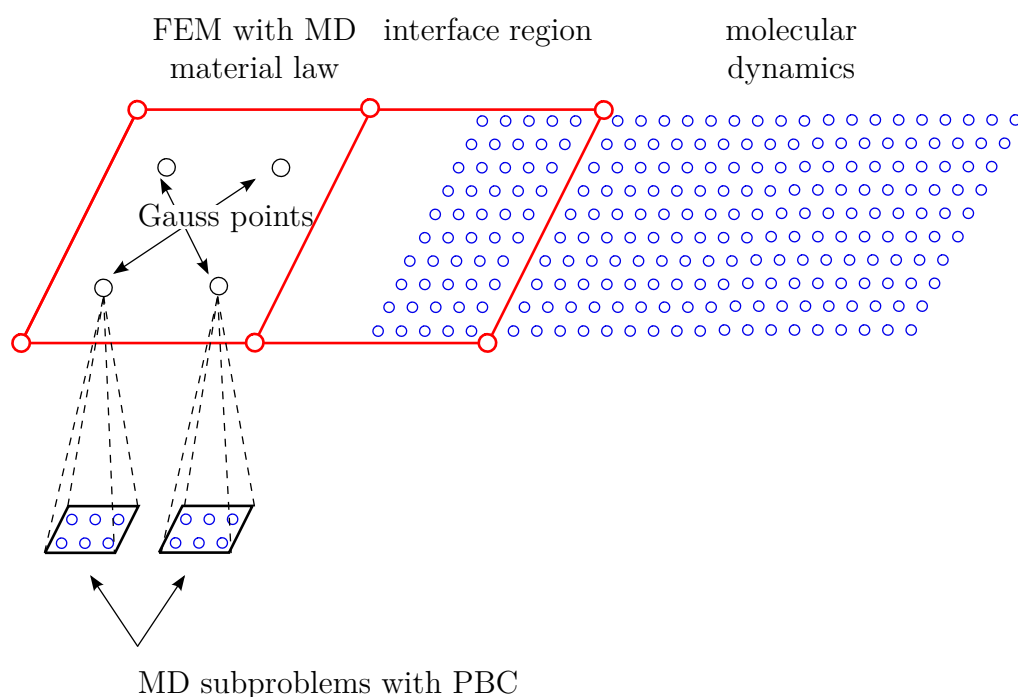
Figure 6.1: Overview multiscale concept

figure are boundary conditions that can be applied to the finite element level or to the molecular dynamics level.

Below the left finite element, subproblems can be seen. These molecular dynamics subproblems have periodic boundary conditions and can be interpreted as a material law. The time scale of the subproblem is decoupled from the time scale of the finite elements and the other atoms. As the subproblems represent a material law, they must only converge to a quasistatic solution.

In the next two sections, the vertical coupling and the horizontal coupling are explained in more detail. The interatomic potential to simulate phase transformation is the potential by MEYER AND ENTEL (1998) for iron and the potential by MENDELEV ET AL. (2016) for titanium.

6.2 Vertical coupling

6.2.1 Global problem

The vertical coupling performs multiscale simulation in a hierarchical way. Finite elements use a molecular dynamics subproblem as material law, similar to the FE^2 method

by FEYEL (2003) or the heterogeneous multiscale method by E AND ENGQUIST (2003). In this work, this method shall be called vertical coupling. This method, coupling finite elements and molecular dynamics, has already been presented in literature, see e.g. ULZ (2015). However, in this work, there are some differences compared to ULZ (2015). The main difference is that in this work explicit non-linear dynamics are used to converge to a quasistatic solution instead of a non-linear static approach. This approach avoids the computation of the stiffness matrix and issues with convergence due to stress oscillations.

finite element mesh   one quad element, 4 Gauss   small representative
                          integration points   subproblem
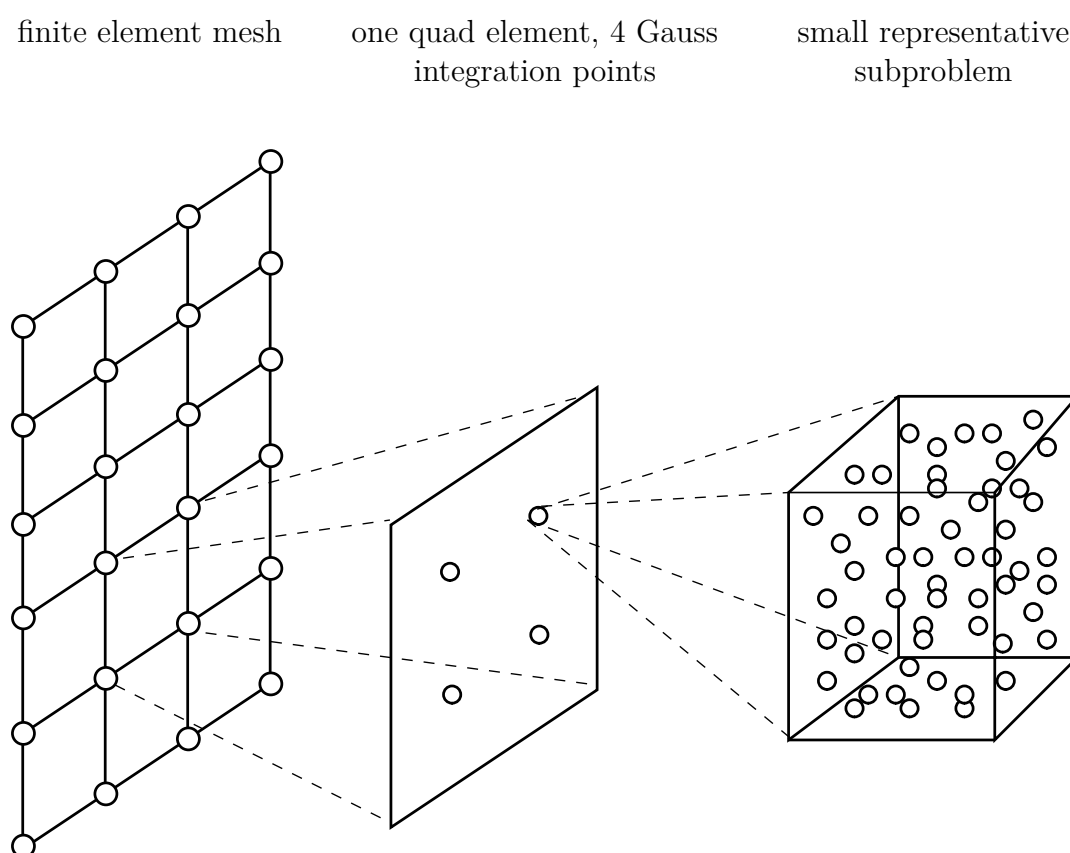
Figure 6.2: Overview vertical coupling

Figure 6.2 shows the basic concept of the vertical coupling. On the left side, a finite element mesh is shown. In the middle, one finite element is shown together with four Gauss integration points. At each Gauss point, there is a molecular dynamics (MD) subproblem. The MD subproblem can be seen as a part of the finite element, symbolizing the hierarchic nature of the method.

According to equation (4.24), the internal nodal forces of a finite element can be calculated as

$$\mathbf{f}_{\text{int}} = \int_{\Omega_0} \mathbf{B}_0^{\text{T}} \mathbf{P} \mathrm{d}\Omega. \tag{6.1}$$

Using the rules for the Gauss quadrature the integral can be transformed into a sum of evaluations of the integrand at specific points.

$$\mathbf{f}_{\text{int}} = \int_{\Omega_0} \mathbf{B}_0^{\text{T}} \mathbf{P} \mathrm{d}\Omega = \Omega_0 \sum_i \omega_i \mathbf{B}_0^{\text{T}} \mathbf{P} \tag{6.2}$$

For a trilinear hexahedron element, eight Gauss points are commonly used.

A typical material law expresses the second Piola-Kirchhoff stress $\mathbf{S}$ and/or the material matrix $\mathbf{C}$ as a function of the strain $\mathbf{E}$ or the deformation gradient $\mathbf{F}$ as expressed in the following equation

$$\mathbf{C} = \mathbf{C}(\mathbf{F}) \tag{6.3}$$

$$\mathbf{S} = \mathbf{S}(\mathbf{F}). \tag{6.4}$$

As the deformation gradient $\mathbf{F}$ is different for each Gauss point, the stress is also different for each Gauss point. Therefore, there must be a representative molecular dynamics problem at each Gauss point that evaluates the stress $\mathbf{S}$ as a function of the deformation gradient $\mathbf{F}$. The first Piola-Kirchhoff stress $\mathbf{P}$ can be calculated from the stress $\mathbf{S}$ by using the deformation gradient $\mathbf{F}$.

The stress at molecular dynamics level is calculated as the virial stress

$$\boldsymbol{\sigma} = \frac{1}{\Omega} \left(-\sum_i m_i \mathbf{v}_i \otimes \mathbf{v}_i + \sum_{i,j<i} \mathbf{r}_{ij} \otimes \mathbf{f}_{ij} \right) \tag{6.5}$$

which is equivalent to the Cauchy stress (SUBRAMANIYAN AND SUN (2008)). A number of time steps are performed at the molecular dynamics level to reduce fluctuations. Alternatively, a kernel can be used to enforce faster convergence to a – not necessarily correct – value as presented by ULZ (2015). The higher the number of time steps, the higher the accuracy. The Cauchy stress is then transformed to the second Piola-Kirchhoff stress $\mathbf{S}$.

The hexahedron element is integrated with 8 Gauss points for the normal part and 2 Gauss points for each shear part as described in Section 4.6.2. This is called selective reduced integration and is used to avoid shear locking. Each of the three shear stresses is integrated with two Gauss points. The integration points for the shear part are at

different locations compared to the integration points of the normal part. However, the stress values at the shear integration points can be calculated from the stress at the 8 standard Gauss integration points. This can be seen in Figure 6.3. The value of the stress at Gauss point (A) can be calculated by taking the average of the Gauss points (G1), (G2), (G3) and (G4). The rest of the points can be calculated accordingly.
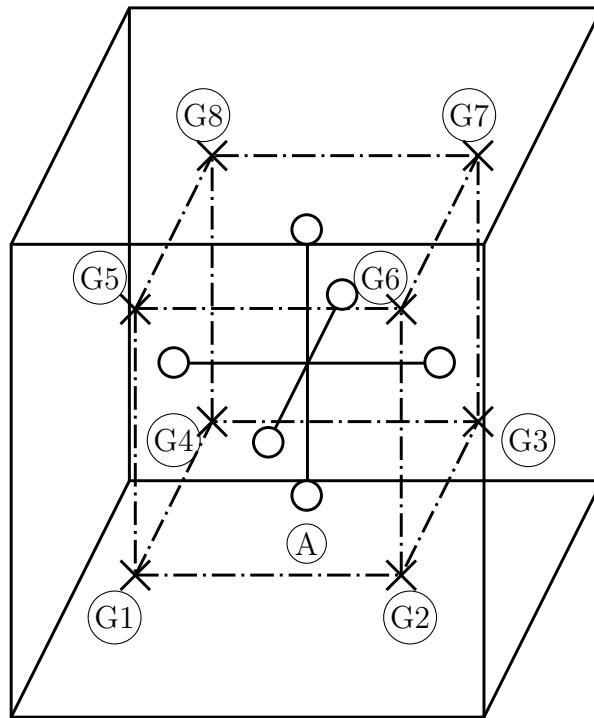
Figure 6.3: Stress calculation, reduced integration

6.2.2 Damping of temperature vibrations

The second order differential equation from Chapter 4, defining the finite element nodal movement is again shown in equation (6.6).

$$\mathbf{M}\ddot{\mathbf{d}} + \mathbf{D}\dot{\mathbf{d}} + \mathbf{f}_{\text{int}}(\mathbf{d}) - \mathbf{f}_{\text{ext}}(\mathbf{d}) = 0 \tag{6.6}$$

The stress calculated from molecular dynamics is fluctuating as already shown in Section 3.4.1. The time steps of the finite elements and molecular dynamics are completely independent of each other, meaning that there is also multiscale in time and not only in space. However, as the frequencies are transferred in a discrete way, the frequency of the stress changes from the fine scale to coarse scale. If the time step of the finite elements is Δt, the highest possible frequency stimulation by the MD material law is $f_{\text{max, FE}} = \frac{1}{2\Delta t}$. Therefore, a damping matrix is necessary to avoid the transfer of vibration energy to the finite elements.

The damping matrix $\mathbf{D}$ is a linear combination of the stiffness matrix and the mass matrix, which is also called Rayleigh-damping (RAYLEIGH, L. (1877)).

$$\mathbf{D} = c_{\text{M}}\mathbf{M} + c_{\text{K}}\mathbf{K} \tag{6.7}$$

Mass proportional damping (constant c_{M}) damps low-frequency modes, while stiffness proportional damping (constant c_{K}) damps high-frequency modes. As the atomic vibration has a very high frequency, stiffness proportional damping is the important factor for the damping of thermal vibrations on the finite element level. However, the damping must not be too strong as in this case the quasistatic solution is not reached. Therefore, it is important to identify dominant frequencies (in most cases the lowest frequencies) of the simulation that must remain underdamped. In the case of Rayleigh-damping, the damping ratio is defined as

$$\zeta_i = \frac{1}{2\omega_i}c_{\text{M}} + \frac{\omega_i}{2}c_{\text{K}}. \tag{6.8}$$

This specific mode will be underdamped, if $\zeta_i < 1$.

Another way to get rid of high-frequency modes in the stress is to perform more MD time steps per FE time step. This is not without disadvantage, as each subproblem consists of at least 128 atoms. The material behavior of one hexahedron element with 8 Gauss points is, therefore, simulated with at least 1024 atoms. If there are 100 hexahedron elements in the simulation, more than 100,000 atoms need to be simulated in each FE time step. Therefore, it makes sense to reduce the number of time steps on the molecular dynamics level per finite element time step to a minimum. The time used to calculate

the finite element movement is much smaller than the computational time for the MD subproblems ($t_{\mathrm{comput,\ FE}} \ll t_{\mathrm{comput,\ MD}}$). Consequently, the total computation time is proportional to the number of time steps selected at MD level.

As a result, the test cases in Chapter 7 use only one MD time step per FE time step. This can be justified for a number of reasons. First, the high damping assures that the rate of deformation is very small, so that the MD subproblem can follow the deformation gradient at the coarse scale. Second, in the case of phase transformation simulation, it is foremost of interest, whether the transformation happens at all in the proposed method. Other questions, like whether the transformation happens on the right time scale, in the right order or how it is influenced by boundary conditions, are beyond the scope of this work and will be left to future work. Only the quasistatic solution after the transition is of interest in this work.

6.2.3 Implementation

In Figure 6.4 a flowchart of the method is shown. There is a finite element level for the coarse scale and a molecular dynamics level for the fine scale.

The starting configuration of the molecular dynamics subproblems is not necessarily at zero stress at the desired temperature. Therefore, before starting the simulation, it might be desirable to do a stress-controlled run of the MD subproblems with the barostat and the thermostat to reset the periodic boundary condition box to a zero stress state. However, this is not without disadvantage. If the velocity distribution of the subproblems has been initiated with a random generator, the velocity distribution in all MD subproblems will be slightly different. This results in the zero stress state in all MD subproblems to be slightly different and creates internal stress in the finite element. Moreover, it will create incompatibility with the horizontal coupling (see Section 6.3), if the lattices do not have the same lattice constants at simulation start.

The simulation is initiated at $\mathbf{F} = \mathbf{I}$. Next, the stress is calculated at the Gauss points. In order to calculate the stress, the MD simulation at Gauss point level is calculated for a few time steps. During this MD run, the PBC box is kept constant. It is ensured that the periodic boundary conditions are enforced and that the temperature is kept at the desired value. The stress is then transferred to the finite element level, where the internal nodal forces are calculated. The internal nodal forces are used to calculate the acceleration of the nodes. Next, the nodal positions and velocities are updated as shown in Figure 4.4. Using the updated nodal positions new deformation gradients at the Gauss points can be calculated and be used for new MD simulations.
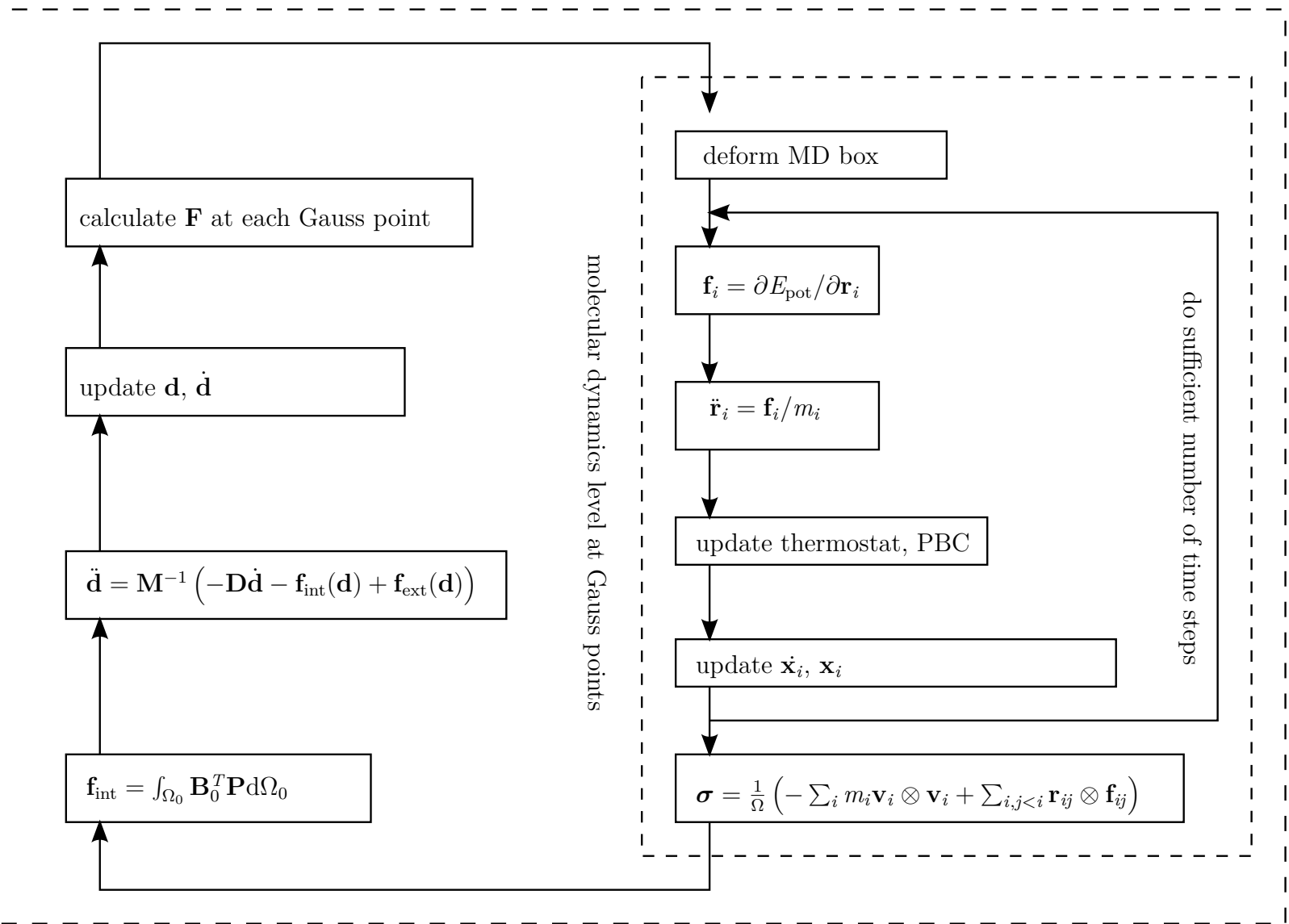
Figure 6.4: Flow chart vertical coupling

6.3 Horizontal coupling

Horizontal coupling means that the atoms and the finite elements are spatially separated into different domains with some kind of interface between the domains. At the interface, an interaction is necessary to couple both methods. In this thesis, a coupling method similar to the AtC method shall be selected.

A part of the atoms is coupled with the finite element movement. Here, two methods are used: the Cauchy rule, as described in Section 6.3.2, and atoms in a PBC box as described in Section 6.3.3. The first method is very similar to the AtC-method, described in Section 5.3.3. The proposed method is, therefore, a force-based method.

As mentioned in Section 5.3.3, force-based methods make use of two independent potentials Π_{atoms} and Π_{FE}. The force on the atoms is then defined as

$$\mathbf{f}_a = -\frac{\partial \Pi_{\text{atoms}}}{\partial \mathbf{r}_a} \tag{6.9}$$

and the force on finite element node I

$$\mathbf{f}_I = -\frac{\partial \Pi_{\text{FE}}}{\partial \mathbf{u}_I}. \tag{6.10}$$

The coupling is achieved by applying a force boundary condition onto the finite element mesh, which is derived from molecular dynamics, and a Dirichlet boundary condition onto the atoms, which is derived from the finite element movement.

6.3.1 Energy of the atoms

In order to understand the coupling, we first divide the atoms into two groups, the free atoms (FA) and the bound atoms (BA). This can be seen in Figure 6.5.

The energy of the atoms can, therefore, be split into three terms.

$$\Pi_{\text{atoms}} = \Pi_{\text{FA-FA}} + \Pi_{\text{FA-BA}} + \Pi_{\text{BA-BA}} \tag{6.11}$$

The three terms can be replaced by sums of the potential function. It is assumed here that the potential energy V only depends on the radial distance between two atoms
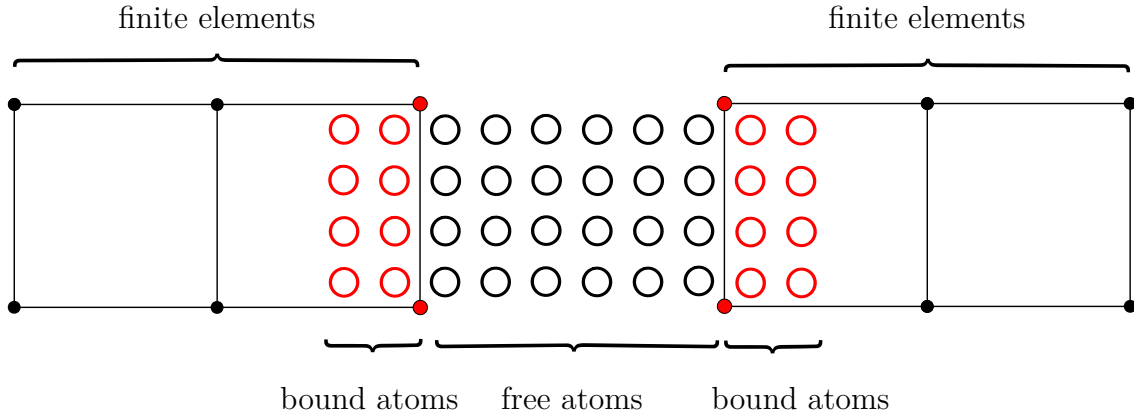
Figure 6.5: Overview horizontal coupling

(like a pair potential) and the electron density is ignored for simplicity reasons.

$$\Pi_{\text{atoms}} = \underbrace{\frac{1}{2} \sum_{\substack{i \in \text{FA} \\ j \in \text{FA} \\ i \neq j}} V(r_{ij})}_{\text{term I}} + \underbrace{\sum_{\substack{i \in \text{FA} \\ a \in \text{BA}}} V(r_{ia})}_{\text{term II}} + \underbrace{\frac{1}{2} \sum_{\substack{a \in \text{BA} \\ b \in \text{BA} \\ a \neq b}} V(r_{ab})}_{\text{term III}} \tag{6.12}$$

r_{ij} is defined as the length of the vector $\mathbf{r}_{ij}$. Furthermore, the vector $\mathbf{r}_{ij}$ is the difference between the positions of atoms i and j.

$$\mathbf{r}_{ij} = \mathbf{r}_j - \mathbf{r}_i. \tag{6.13}$$

Next, we take a closer look at term II. The first variation of the term looks like this:

$$\sum_{\substack{i \in \text{FA} \\ a \in \text{BA}}} \delta V(r_{ia}) = \sum_{\substack{i \in \text{FA} \\ a \in \text{BA}}} \left(\delta \mathbf{r}_i^{\text{T}} \frac{\partial V(r_{ia})}{\partial \mathbf{r}_i} + \delta \mathbf{r}_a^{\text{T}} \frac{\partial V(r_{ia})}{\partial \mathbf{r}_a} \right) \tag{6.14}$$

Expanding the variation with derivatives, we arrive at:

$$\sum_{\substack{i \in \text{FA} \\ a \in \text{BA}}} \delta V(r_{ia}) = \sum_{\substack{i \in \text{FA} \\ a \in \text{BA}}} \left(\delta \mathbf{r}_i^{\text{T}} \frac{\partial V(r_{ia})}{\partial r_{ia}} \frac{\partial r_{ia}}{\partial \mathbf{r}_{ia}} \frac{\partial \mathbf{r}_{ia}}{\partial \mathbf{r}_i} + \delta \mathbf{r}_a^{\text{T}} \frac{\partial V(r_{ia})}{\partial r_{ia}} \frac{\partial r_{ia}}{\partial \mathbf{r}_{ia}} \frac{\partial \mathbf{r}_{ia}}{\partial \mathbf{r}_a} \right) \tag{6.15}$$

Simplifying the system, we obtain

$$\sum_{\substack{i \in \text{FA} \\ a \in \text{BA}}} \delta V(r_{ia}) = \sum_{\substack{i \in \text{FA} \\ a \in \text{BA}}} \left(\delta \mathbf{r}_i^{\text{T}} \frac{\partial V(r_{ia})}{\partial r_{ia}} \frac{\mathbf{r}_{ia}}{r_{ia}} (-1) + \delta \mathbf{r}_a^{\text{T}} \frac{\partial V(r_{ia})}{\partial r_{ia}} \frac{\mathbf{r}_{ia}}{r_{ia}} (+1) \right) \tag{6.16}$$

With the definition

$$\mathbf{f}_{ia} = \frac{\partial V(r_{ia})}{\partial r_{ia}} \frac{\mathbf{r}_{ia}}{r_{ia}} \tag{6.17}$$

the equation system can be simplified to

$$\sum_{\substack{i \epsilon \mathrm{FA} \\ a \epsilon \mathrm{BA}}} \delta V(r_{ia}) = \sum_{\substack{i \epsilon \mathrm{FA} \\ a \epsilon \mathrm{BA}}} \left(-\delta \mathbf{r}_i^{\mathrm{T}} \mathbf{f}_{ia} + \delta \mathbf{r}_a^{\mathrm{T}} \mathbf{f}_{ia} \right). \tag{6.18}$$

The force between two atoms is acting on the two atoms with opposite signs, respectively. Now two question arise: first, how to distribute the forces acting on the bound atoms to the finite element nodes and second, how are the bound atoms moved. In Sections 6.3.2 and 6.3.3 the question of the movement of bound atoms shall be discussed. The forces on the bound atoms are projected to the finite element nodes. These forces are just a force boundary condition to the finite elements. This is discussed in more detail in Section 6.3.5.

6.3.2 Cauchy rule

The Cauchy rule assumes that the displacement of the atoms follows the deformation of continuum mechanics or more specifically – in this case – the finite element nodal movement. Therefore, it is possible to define the position of atom a as an interpolation of the finite element nodal position vector $\mathbf{d}$ with an atom-specific matrix $\mathbf{N}_a$

$$\mathbf{r}_a = \mathbf{N}_a\mathbf{d}. \tag{6.19}$$

The matrix $\mathbf{N}_a$ has the dimensions $3 \times n_{\text{DOF finite element}}$. The coefficients of the matrix can be set to be the shape functions evaluated at the initial coordinates of the atoms.

$$\mathbf{N}_a^{\mathrm{T}} = \begin{bmatrix} N_1(\xi_a,\eta_a,\zeta_a) & 0 & 0 \\ 0 & N_1(\xi_i,\eta_i,\zeta_a) & 0 \\ 0 & 0 & N_1(\xi_a,\eta_a,\zeta_a) \\ N_2(\xi_a,\eta_a,\zeta_a) & 0 & 0 \\ 0 & N_2(\xi_a,\eta_a,\zeta_a) & 0 \\ 0 & 0 & N_2(\xi_a,\eta_a,\zeta_a) \\ N_3(\xi_a,\eta_a,\zeta_a) & 0 & 0 \\ 0 & N_3(\xi_a,\eta_a,\zeta_a) & 0 \\ 0 & 0 & N_3(\xi_a,\eta_a,\zeta_a) \\ \vdots & \vdots & \vdots \\ N_{n_{\text{nodes}}}(\xi_a,\eta_a,\zeta_a) & 0 & 0 \\ 0 & N_{n_{\text{nodes}}}(\xi_a,\eta_a,\zeta_a) & 0 \\ 0 & 0 & N_{n_{\text{nodes}}}(\xi_a,\eta_a,\zeta_a) \end{bmatrix} \tag{6.20}$$

The coordinates ξ_a,η_a and ζ_a are the initial coordinates of the atoms at the start of the simulation in the local coordinate system of the corresponding finite element.

The variation of $V(r_{ia})$ then becomes

$$\sum_{\substack{i\epsilon\text{FA} \\ a\epsilon\text{BA}}} \delta V(r_{ia}) = \sum_{\substack{i\epsilon\text{FA} \\ a\epsilon\text{BA}}} \left(-\delta\mathbf{r}_i^{\mathrm{T}}\mathbf{f}_{ia} + \delta\mathbf{d}^{\mathrm{T}}\mathbf{N}_a^{\mathrm{T}}\mathbf{f}_{ia}\right). \tag{6.21}$$

6.3.3 Subboxes as interface

The subbox idea is inspired by the vertical coupling of the molecular dynamic subboxes and transfers it to the horizontal coupling. The idea is that the bound atoms do not move according to the deformation gradient, but that they are in a box with periodic boundary conditions. This coupling is less constraining for the bound atoms and allows for more degrees of freedoms, which makes internal restructuring of the atoms possible

(like e.g. phase transformation). It also comes along with a few challenges as a box with periodic boundary conditions can only assume a constant stress state, which might make the coupling less accurate in e.g. bending problems.

The periodic boundary conditions box is moving according to the finite element movement. However, the box must be a parallelepiped/parallelogram, while the deformed finite element is not. It follows that the subproblem can only make a "fit" to the deformed finite element as can be seen in Figure 6.6. The illustration is shown in 2D for simplicity, but is analogous in 3D. On the left side finite elements, atoms and PBC box are shown in an undeformed configuration. In the middle, the finite element has been deformed. The PBC box cannot match a deformation, where two opposing sides are not parallel to each other. Therefore, on the right side a fit was made to the finite element deformation.
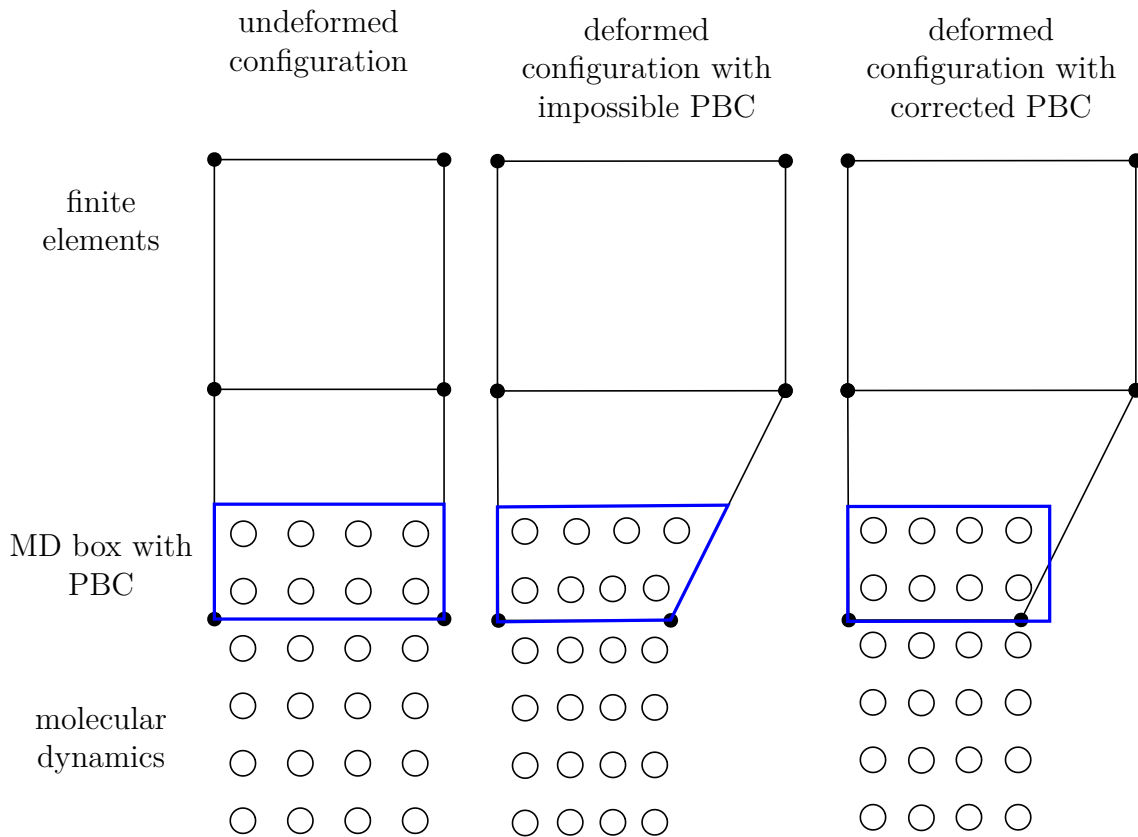
Figure 6.6: Concept of coupling with subboxes

6.3.4 Equivalent parallelepiped

A method to determinate a good fit of a parallelepiped to a deformed finite element will be investigated in this subsection. For reasons of simplicity, only a 2D-example is

presented. However, in 3D the approach is the same. Figure 6.7 shows an arbitrary quadrilateral in red with a parallelogram in black. The derivation of the parallelepiped shall be discussed in the following.
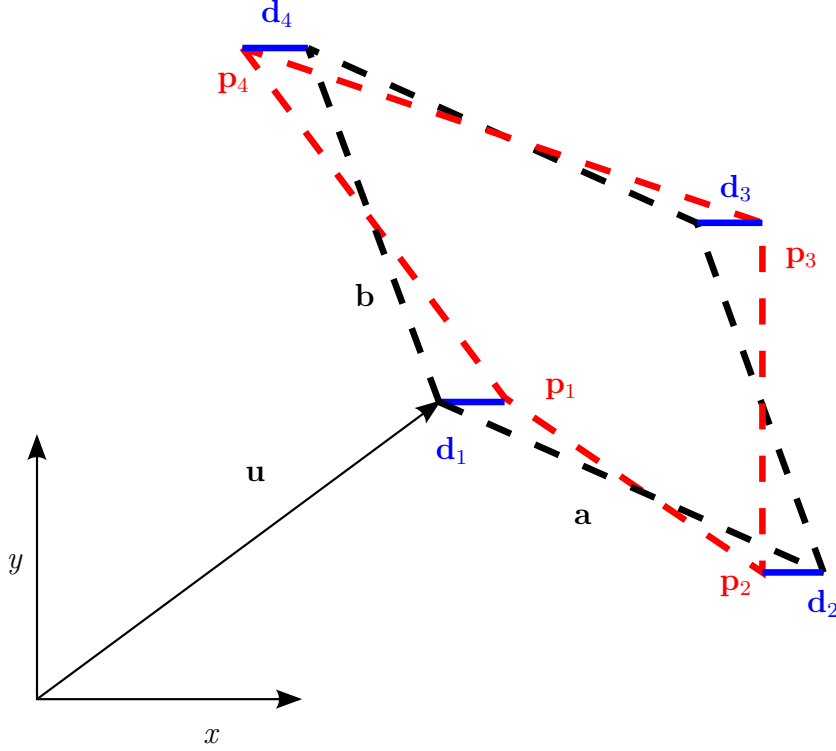
Figure 6.7: Fitting a parallelepiped to an arbitrary quadrilateral

In order to make a good fit, we want to minimize the sum of the squares of the nodal distances between the finite element (red) and the parallelepiped (black) as in equation (6.22). The quadrilateral is defined by the four corner points $\mathbf{p}_1$, $\mathbf{p}_2$, $\mathbf{p}_3$ and $\mathbf{p}_4$. The parallelogram is defined by the displacement vector $\mathbf{u}$ and the vectors $\mathbf{a}$ and $\mathbf{b}$ that form the parallelogram. Taking the difference between the corner points, the following equations can be derived:

$$\Psi = d_1^2 + d_2^2 + d_3^2 + d_4^2 \tag{6.22}$$

$$\Psi = |\mathbf{p}_1 - \mathbf{u}|^2 + |\mathbf{p}_2 - \mathbf{u} - \mathbf{a}|^2 + |\mathbf{p}_3 - \mathbf{u} - \mathbf{a} - \mathbf{b}|^2 + |\mathbf{p}_4 - \mathbf{u} - \mathbf{b}|^2 \tag{6.23}$$

Next, we take the derivative of the equation with respect to the six unknowns to be zero. This results in six equations for six unknows.

$$\frac{\partial \Psi}{\partial u_x} = \frac{\partial \Psi}{\partial u_y} = \frac{\partial \Psi}{\partial a_x} = \frac{\partial \Psi}{\partial a_y} = \frac{\partial \Psi}{\partial b_x} = \frac{\partial \Psi}{\partial b_y} = 0 \tag{6.24}$$

The result is

$$\mathbf{a} = \frac{1}{2}(\mathbf{p}_3 + \mathbf{p}_2 - \mathbf{p}_1 - \mathbf{p}_4) \tag{6.25}$$

$$\mathbf{b} = \frac{1}{2}(\mathbf{p}_3 + \mathbf{p}_4 - \mathbf{p}_1 - \mathbf{p}_2) \tag{6.26}$$

$$\mathbf{u} = \frac{1}{4}(3\mathbf{p}_1 - \mathbf{p}_3 + \mathbf{p}_2 + \mathbf{p}_4) \tag{6.27}$$

The calculation is similar for a 8-node hexahedron. In this case, the parallelepiped is defined by three vectors $\mathbf{a}$, $\mathbf{b}$ and $\mathbf{c}$.

$$\mathbf{a} = \frac{1}{4}(\mathbf{p}_2 + \mathbf{p}_3 + \mathbf{p}_6 + \mathbf{p}_7 - \mathbf{p}_1 - \mathbf{p}_4 - \mathbf{p}_5 - \mathbf{p}_8) \tag{6.28}$$

$$\mathbf{b} = \frac{1}{4}(\mathbf{x}_3 + \mathbf{p}_4 + \mathbf{p}_7 + \mathbf{p}_8 - \mathbf{p}_1 - \mathbf{p}_2 - \mathbf{p}_5 - \mathbf{p}_6) \tag{6.29}$$

$$\mathbf{c} = \frac{1}{4}(\mathbf{x}_5 + \mathbf{p}_6 + \mathbf{p}_7 + \mathbf{p}_8 - \mathbf{p}_1 - \mathbf{p}_2 - \mathbf{p}_3 - \mathbf{p}_4) \tag{6.30}$$

$$\mathbf{u} = \frac{1}{4}(2\mathbf{p}_1 + \mathbf{p}_2 + \mathbf{p}_4 + \mathbf{p}_5 - \mathbf{p}_7). \tag{6.31}$$

The position of the nodes $\mathbf{p}_1 \ldots \mathbf{p}_8$ are as seen in Figure 4.2.

As the subproblem in the finite element is constantly moving, further constraints are necessary in order to stabilize the coupling. As the atoms in the subbox are also fluctuating the atoms can jump between opposing sides within the PBC box. This results in force jumps with previously unseen free atoms and kicks free atoms out of the atomic lattice. Additional constraints are:

- The average position of the atoms in the box must remain in the center of the PBC box

- Atoms can move freely within the PBC box, but can not move outside of the box or jump to the other side. If they touch the boundary, they can move no further and the speed is set to zero.

- The force interaction between two bound atoms inside the same box also works over the periodic boundary condition.

Even taking these limitations into account, free atoms at the boundary may still be kicked out of the lattice due to thermal stimulation (see also Chapter 7). This might be mitigated by letting the free atoms interact with time-averaged positions of the bound atoms but due to time constraints, this is not implemented in this work.

Another challenge arises when the shape of the finite element cells is deviating from a rectangular shape. In this case, two neighboring parallelepipeds may overlap with

each other or create a cavity between them. This effect can be reduced by appropriate meshing and small angle changes in deformation. The problem is visualized in Figure 6.8.
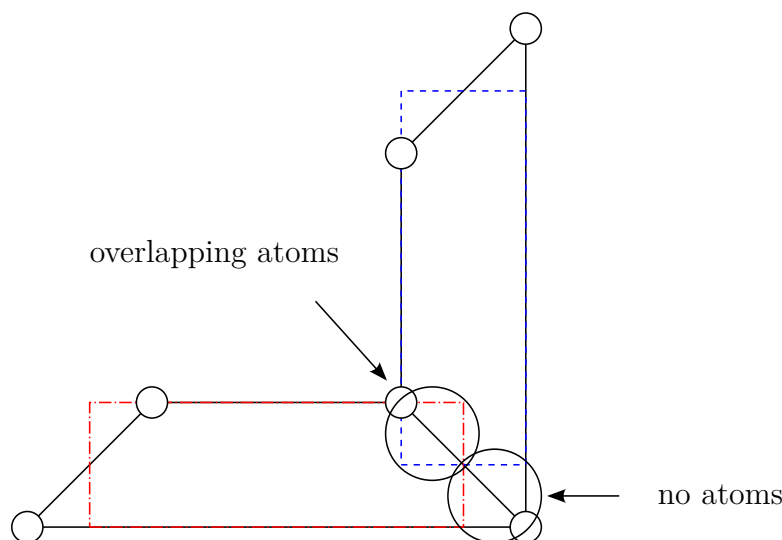
Figure 6.8: Two finite elements (black) and their best fit subboxes. On one side an empty space is created, while on the other side, the two boxes overlap.

As an atom in the subproblem only sees other atoms in its own subproblem, this is not a problem for the subproblems themselves. However, outside atoms may be pressed into the cavity or pressed out of position, because of more than one subproblem occupying the same space.

6.3.5 Distribution of atom forces to finite element nodes

The forces on the bound atoms must be distributed to the finite element nodes of the element they are bound to. This can be done with the shape functions of the finite element. However, just using all standard shape functions will result in forces being added to nodes that are not at the interface between FE and MD. These forces will lead to wrong stress results in the element. In Figure 6.9 it can be seen that in a 1D case the forces F_1 and F_2 lead to a force on both finite element nodes.

In other words, it is desirable to limit the forces to the finite elements at the interface. These nodes are marked in *red* in Figure 6.5. In order to distribute the forces to a limited set of nodes, modified shape functions can be used. This is possible by simply rearranging the equations. Consider a simple 2D element with four shape functions. We
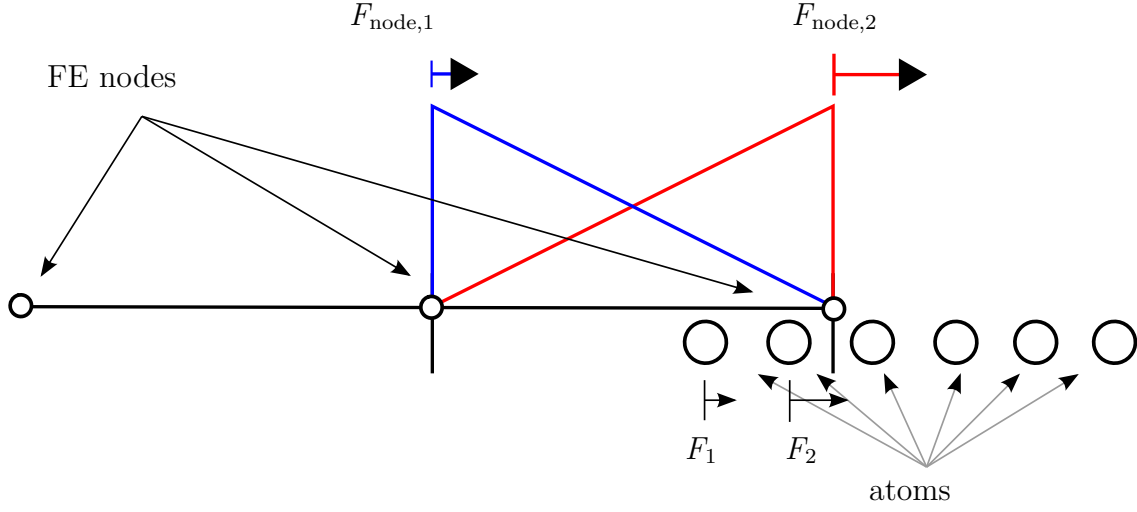
Figure 6.9: Atom forces on finite element nodes

want to eliminate the fourth shape function

$$N_1 + N_2 + N_3 + N_4 = 1 \quad (6.32)$$

$$N_1 + N_2 + N_3 + N_4 \underbrace{(N_1 + N_2 + N_3 + N_4)}_{=1} = 1 \quad (6.33)$$

$$N_1 + N_1 N_4 + N_2 + N_2 N_4 + N_3 + N_3 N_4 + N_4^2 = 1 \quad (6.34)$$

$$N_1 + N_1 N_4 + N_2 + N_2 N_4 + N_3 + N_3 N_4 + N_4^2(N_1 + N_2 + N_3 + N_4) = 1 \quad (6.35)$$

$$N_1 + N_1 N_4 + N_1 N_4^2 + N_2 + N_2 N_4 + N_2 N_4^2 + N_3 + N_3 N_4 + N_3 N_4^2 + N_4^3 = 1 \quad (6.36)$$

$$N_1(1 + N_4 + N_4^2) + N_2(1 + N_4 + N_4^2) + N_3(1 + N_4 + N_4^2) + N_4^3 = 1 \quad (6.37)$$

If we repeat the procedure an infinite number of times, one arrives at

$$N_1 \left(\sum_{i=0}^{\infty} N_4^i \right) + N_2 \left(\sum_{i=0}^{\infty} N_4^i \right) + N_3 \left(\sum_{i=0}^{\infty} N_4^i \right) = 1. \quad (6.38)$$

Apart from node 4, $N_4 < 1$, therefore, the sum can be simplified to

$$\sum_{i=0}^{\infty} N_4^i = \frac{1}{1 - N_4}. \quad (6.39)$$

Now equation 6.38 can be simplified to

$$N_1 \frac{1}{1 - N_4} + N_2 \frac{1}{1 - N_4} + N_3 \frac{1}{1 - N_4} = 1 \tag{6.40}$$

$$\frac{N_1}{1 - N_4} + \frac{N_2}{1 - N_4} + \frac{N_3}{1 - N_4} = 1 \tag{6.41}$$

$$N_1' + N_2' + N_3' = 1 \tag{6.42}$$

As can be seen from equation (6.40) the starting equation (6.32) can be simplified in a much more simple way by moving N_4 to the right side and dividing by $1 - N_4$. However, the more complex derivation shows that the value of the fourth shape function is distributed to the other nodes in a weighted and understandable manner.

How do these modified shape functions look like? In the 1D example of the figure above, the shape functions N_1' and N_2' become

$$N_2' = \frac{N_1}{1 - N_2} = \frac{(1 - \xi)/2}{1 - (1 + \xi)/2} = \frac{(1 - \xi)/2}{(1 - \xi)/2} = 1 \tag{6.43}$$

$$N_1' = 1 - N_2' = 0. \tag{6.44}$$

In the case of a hexahedron, the resulting shape functions are more complex.

6.3.6 Implementation

The horizontal coupling is implemented into the NumPro software developed at the IBB. The flow chart can be seen in Figure 6.10. A typical loop starts by getting the finite element atom positions. If the Cauchy type coupling used, the bound atoms will be deformed according to the FE displacement. If the subboxes type coupling is selected, this step is ignored.

Next, the MPI data exchange is performed, if the molecular dynamics domain has been split into multiple domains. If this is not the case, this step can be omitted.

If the subboxes coupling has been chosen, the next step is the calculation of the atoms in the subboxes. The parallelepipeds are updated using the atom deformation and the forces on the atoms are calculated from the EAM potential. The thermostat is applied individually to each subbox. Finally, time integration is done and the periodic boundary conditions are enforced.

The next step is to update the free atoms. The free atoms are also interacting with the bound atoms in the finite elements. Once the electron density has been calculated, the density can be exchanged with neighboring domains if more than one MD domain

is present. This is followed by the calculation of the atom forces on free atoms and bound atoms. The forces on the bound atoms are recalculated to the FE nodes as described in Chapter 6.3.5 and sent to the finite element part of the code. Finally, atom velocities are adjusted with the thermostat and atom positions are updated with the verlet algorithm.

The molecular dynamics part is integrated into the code as a different branch that does not run on the same process as the finite element part as seen in Figure 6.11. The molecular dynamics part – consisting of one or more processes – is a separate part of the code that interacts with the finite element part via MPI messaging. Both FE and MD process run in parallel and exchange information in each iteration. The FE process sends information about the nodal displacement to the molecular dynamics process, which is used to update the position of the bound atoms. On the other side, the molecular dynamics part calculates the nodal forces for the finite elements and sends this information to the finite element process, where the nodal forces are added as an external force to the simulation.

Two boxes with a grey background are visible in the figure. On the left the finite element movement and on the right the movement of the atoms. The part about finite element movement, including the vertical coupling, was already shown in Figure 6.4. The MD subproblems of the vertical coupling are calculated in this thesis on the FE process, which is not very efficient from a speed perspective, but could not be improved due to time constraints. The atomic movement of the vertical coupling is shown in more detail in Figure 6.10.
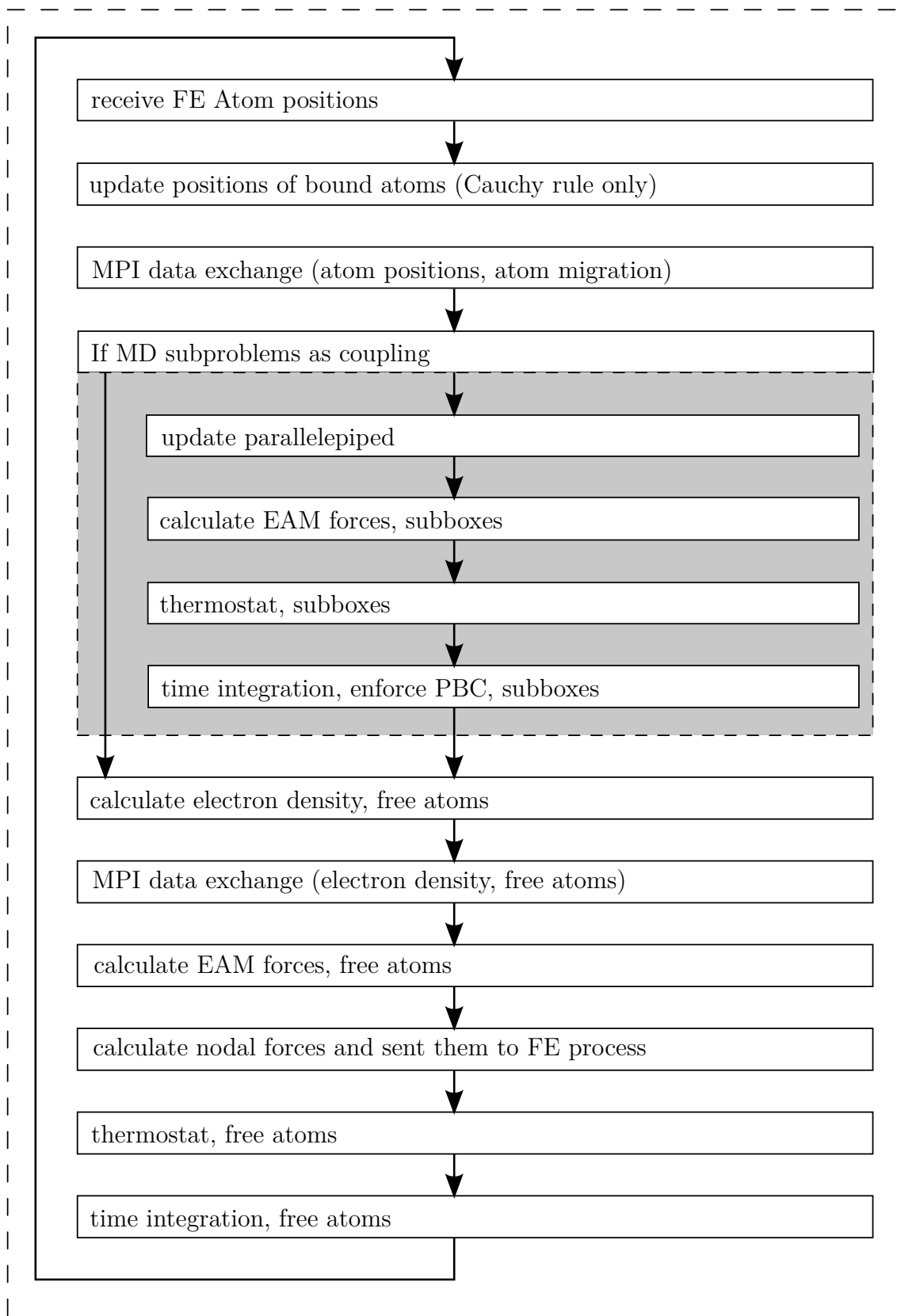
Figure 6.10: Flow chart of horizontal coupling
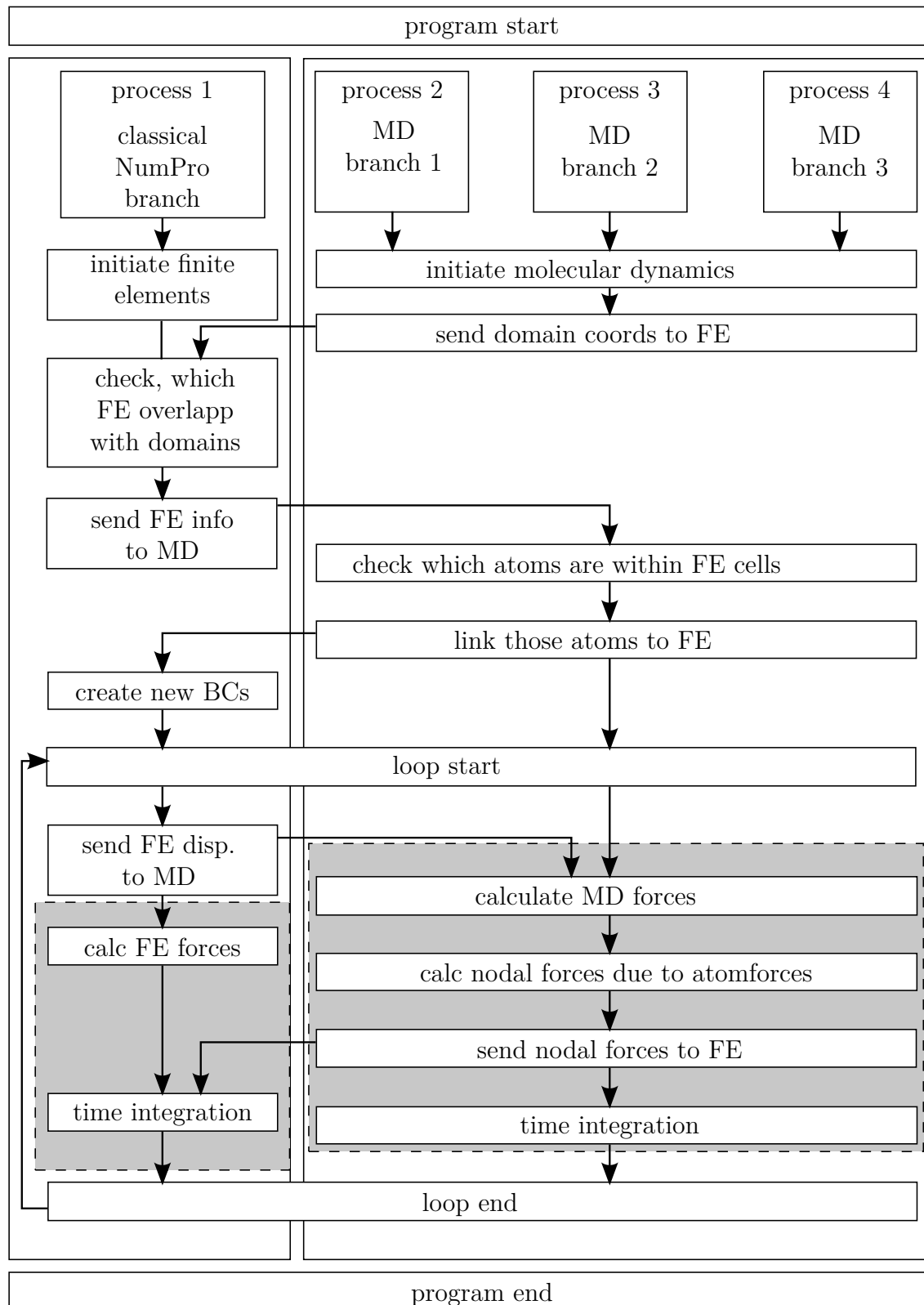
Figure 6.11: Flow chart of combined simulation

<div style="text-align: right; font-size: 4em; font-weight: bold;">7</div>

Multiscale test cases

7.1 Overview

The test cases are separated into three main categories. First, a tensile test and a bending test are performed to ensure the basic functionality of the method. Next, the vertical coupling is used to verify that phase transformation is possible for a single hexahedron. The phase transformations between BCC and FCC and between HCP and BCC are investigated in both directions. Finally the same phase transformations are investigated using both horizontal and vertical coupling simultaneously.

7.2 Tensile test

The first test case is a simple tensile test. This test is used to verify the basic functionality of the vertical and horizontal coupling methods. The problem description is shown in Figure 7.1. The problem is divided into two possible discretizations: Case A for vertical coupling only and Case B for both vertical and horizontal coupling.

A rod with quadratic cross section is pulled by a force on the right side. The rod has a length of $7l_0$, and a width of l_0 and a height of l_0. The values for the variables can be seen in Table 7.1. The material is modeled after the potential from MENDELEV ET AL. (2003). The elastic constants of the Mendelev potential at 300 K can be seen in Table 3.1.

The simulation is carried out for a total time of 0.2 nano seconds, divided into 50,000 time steps. Damping is used on the finite elements to converge to a quasi-static solution. The hexahedral elements use a finite element formulation with 8 nodes and trilinear shape functions as described in Chapter 4.
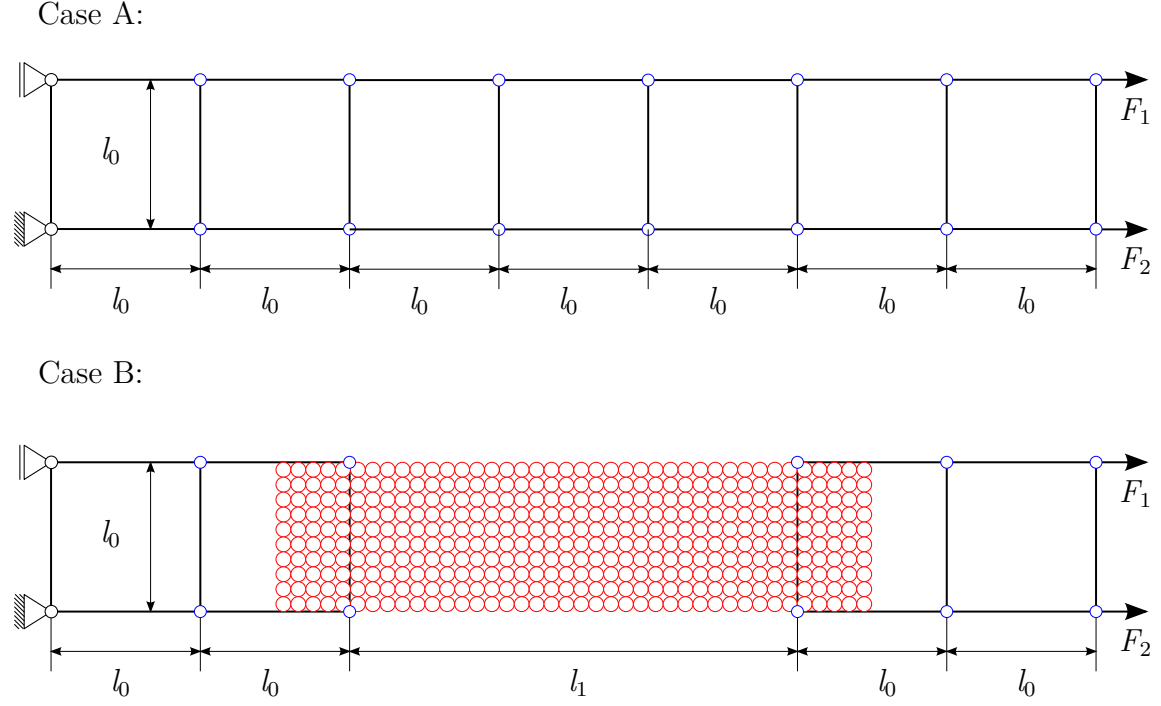
Case A:

Case B:

Figure 7.1: Top (Case A): A rod with quadratic cross section is meshed with seven hexahedron elements. The rod has a thickness of l_0.
Bottom (Case B): A rod partially meshed with finite elements. In the center, atoms are used as representation of the metal. The partially overlapping atoms are used for coupling

Quantity	value
C_{11}	233 GPa
C_{12}	136 GPa
C_{44}	118 GPa

Quantity	value
l_0	28.665 Å
l_1	$3l_0$
temperature	300 K

Table 7.1: General parameters of the test case

On the left side of the rod, all degrees of freedom of the finite elements are fixed. On the right side a force is pulling to the right. The force F equals $F_{\text{tot}} = 3\,\text{eV}/\text{Å}$. This yields a total force of $F = F_1 = F_2 = 12\,\text{eV}/\text{Å}$ or a pressure of

$$p = \frac{4F}{l_0^2} = 0.0146\,\frac{\text{eV}}{\text{Å}^3} = 2.34\,\text{GPa}. \tag{7.1}$$

7.2.1 Damping factor

In the dynamic simulation of a simple tensile test, the most important deformation mode is the first longitudinal vibration mode. This problem can be simplified by using

one finite bar element that has a force on the right and is fixed on the left. The critical damping ratio should be close to 1 from below in order to ensure fast convergence. The critical damping ratio should not be above 1 as in this case the solution is never reached.

A simple 1D rod with density ρ_m and stiffness k has the following differential equation.

$$\frac{\rho_m Al}{2} \begin{bmatrix} 1 & 0 \\ 0 & 1 \end{bmatrix} \ddot{\mathbf{d}} + \frac{EA}{l} \begin{bmatrix} 1 & -1 \\ -1 & 1 \end{bmatrix} \mathbf{d} = \mathbf{F}. \tag{7.2}$$

If the left side is fixed, the equation simplifies to

$$\frac{\rho_m Al}{2} \ddot{d_2} + \frac{EA}{l} d_2 = F. \tag{7.3}$$

This can be rearranged to

$$\ddot{d_2} + \frac{2E}{\rho_m l^2} d_2 = \frac{2F}{\rho_m Al}. \tag{7.4}$$

With this, the critical frequency is found as

$$\omega = \frac{1}{l} \sqrt{\frac{2E}{\rho_m}}. \tag{7.5}$$

From the matrix of elastic constants, the Young's modulus E can be derived as

$$E = \frac{C_{11}^2 + C_{11}C_{12} - 2C_{12}^2}{C_{11} + C_{22}} = 133 \, \text{GPa}. \tag{7.6}$$

The eigenfrequency ω is then equal to $\omega = 0.00296 \cdot (10.18 \, \text{fs})^{-1}$. With $c_K = 500$ being the critical damping ratio of this mode, using stiffness proportional damping, is $\zeta = \frac{\omega}{2} c_K = 0.74 < 1$.

7.2.2 Molecular dynamics solution

As a reference solution, a pure molecular dynamics solution is calculated. However, boundary effects are a problem and cannot be removed from the simulation. In other words, there might be a discrepancy in the molecular dynamics solution to be expected, compared to the multiscale solutions seen later. In addition to the boundary effects, another problem is that it was not possible to enter complex boundary conditions into an existing molecular dynamics program called IMD from another institute at the University of Stuttgart (ROTH ET AL. (2000)), that was planned to be used as a reference in this thesis. Therefore, the horizontal coupling from this thesis was used for the molecular dynamics solution. The problem setup is shown in Figure 7.2.
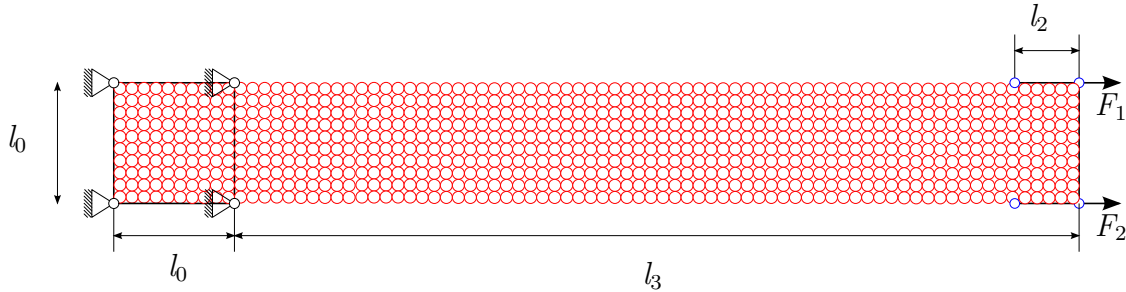
Figure 7.2: Tensile test case with (mostly) pure molecular dynamics. The boundary conditions have been applied with horizontal coupling.

On the left side, a finite element is filled with atoms that are coupled to the finite element via the Cauchy rule. As all finite element nodes are fixed, the bound atoms do not move. On the right side, there is also a finite element in order to apply the force boundary condition to the atoms. The lengths l_2 and l_3 are defined as $l_2 = l_0/2$ and $l_3 = 7l_0$. The simulation is run for a total of 2,000,000 time steps with $\Delta t = 2$ fs. The damping coefficients are $c_M = 0.001$ and $c_K = 1000$. Due to the strong vibrations of the atoms and the small/light finite element at the end of the beam, the damping was selected higher than the 500, assumed in the previous section for the stiffness proportional damping. The convergence is still undercritical, see Figure 7.7.

Figure 7.3 shows the atoms at the end of the simulation. The resulting displacement with molecular dynamics at the right side is 3.4 Å.

7.2.3 Case A

In Case A, two material laws are investigated. First, a constant material tensor $\mathbf{C}$ is assumed with the elastic constants of the iron potential by MENDELEV ET AL. (2003). The second material law is the vertical coupling with the same potential.
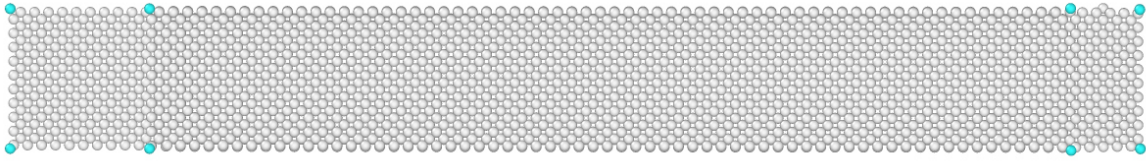
Figure 7.3: Results for the tensile test using (mostly) molecular dynamics

Cubic material law

All element edges align with the reference coordinate system. Therefore, no transformation of the elastic tensor is necessary for the cubic material law. The elasticity tensor is given as

$$
\mathbf{C} = \begin{bmatrix}
C_{11} & C_{12} & C_{12} & 0 & 0 & 0 \\
C_{12} & C_{11} & C_{12} & 0 & 0 & 0 \\
C_{12} & C_{12} & C_{11} & 0 & 0 & 0 \\
0 & 0 & 0 & C_{44} & 0 & 0 \\
0 & 0 & 0 & 0 & C_{44} & 0 \\
0 & 0 & 0 & 0 & 0 & C_{44}
\end{bmatrix}
\tag{7.7}
$$

with $C_{11} = 224$ GPa, $C_{11} = 126$ GPa and $C_{11} = 94$ GPa. The damping matrix is using the Rayleigh-damping definition $\mathbf{D} = c_M \mathbf{M} + c_K \mathbf{K}$ with $c_M = 0$ and $c_K = 500$. The simulation is performed with NumPro. The time step is 4 fs and 50,000 time steps are calculated.

Figure 7.4 shows the results for deformation and stress. The deformation in x-direction is 3.45 Å and stress is 0.0143 $\frac{\text{eV}}{\text{Å}^3}$. The stress field is almost homogeneous and the small deviations arise from numerical imperfections. In addition, the displacement field is linear as expected.

Vertical coupling

Next, the vertical coupling is investigated. Instead of using the material tensor with the three constants C_{11}, C_{12} and C_{44}, at each Gauss point, a molecular dynamics subproblem is used that returns the stress as a function of the strain $\mathbf{S} = \mathbf{S}(\mathbf{E})$. At each Gauss point, the molecular dynamics subproblem has a total of 128 atoms with a temperature of 300 K. The simulation is performed with NumPro. The runtime is 8800 seconds. The damping matrix is using the Rayleigh-damping definition $\mathbf{D} = c_M \mathbf{M} + c_K \mathbf{K}$ with $c_M = 0$ and $c_K = 500$. The time step is 2 fs and 50,000 time steps are calculated.
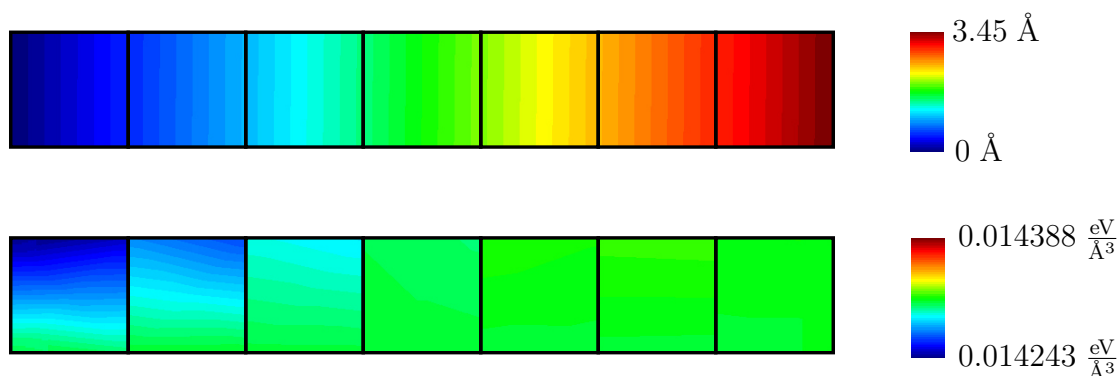
Figure 7.4: Results for the tensile test using only finite elements and the cubic material law. On the top, the horizontal deformation is seen and on the bottom, the second Piola-Kirchhoff stress S_{xx}
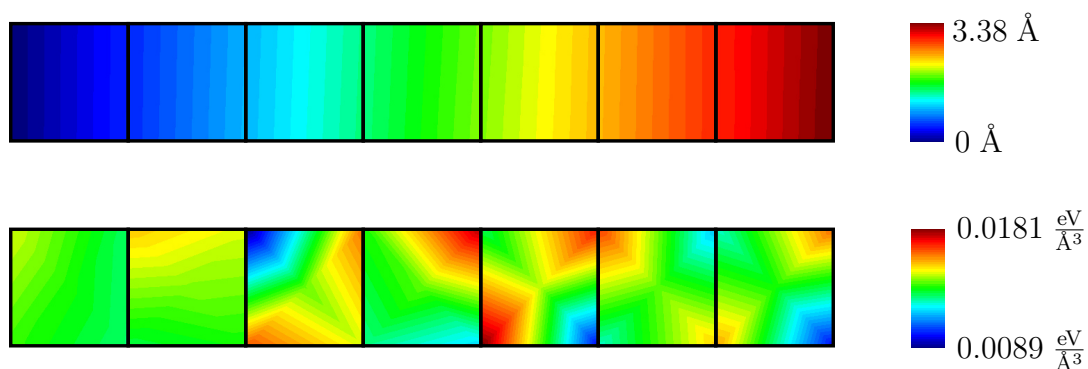
Figure 7.5: Results for the tensile test using only finite elements and the molecular dynamic subproblems at the Gauss points. On the top, the vertical deformation is seen and on the bottom, the second Piola-Kirchhoff stress S_{xx}

In Figure 7.5 the results are shown. They show good displacement results. However, the stress in the elements fluctuates by a factor of 1.5, which results from the stress fluctuations and the small problem size at each Gauss point. The displacement is 3.38 Å.

7.2.4 Case B

The second case consists of testing the horizontal coupling using either the Cauchy rule or the subboxes coupling. In addition, on the finite element level either the cubic material law is used or the vertical coupling. The damping matrix is using the Rayleigh-damping definition $\mathbf{D} = c_M \mathbf{M} + c_K \mathbf{K}$ with $c_M = 0$ and $c_K = 500$. The simulation is performed with NumPro. The time step is 4 fs and 100,000 time steps are calculated in case of the CML and 50,000 in case of the vertical coupling. The results of these four combinations are shown in Figure 7.6.
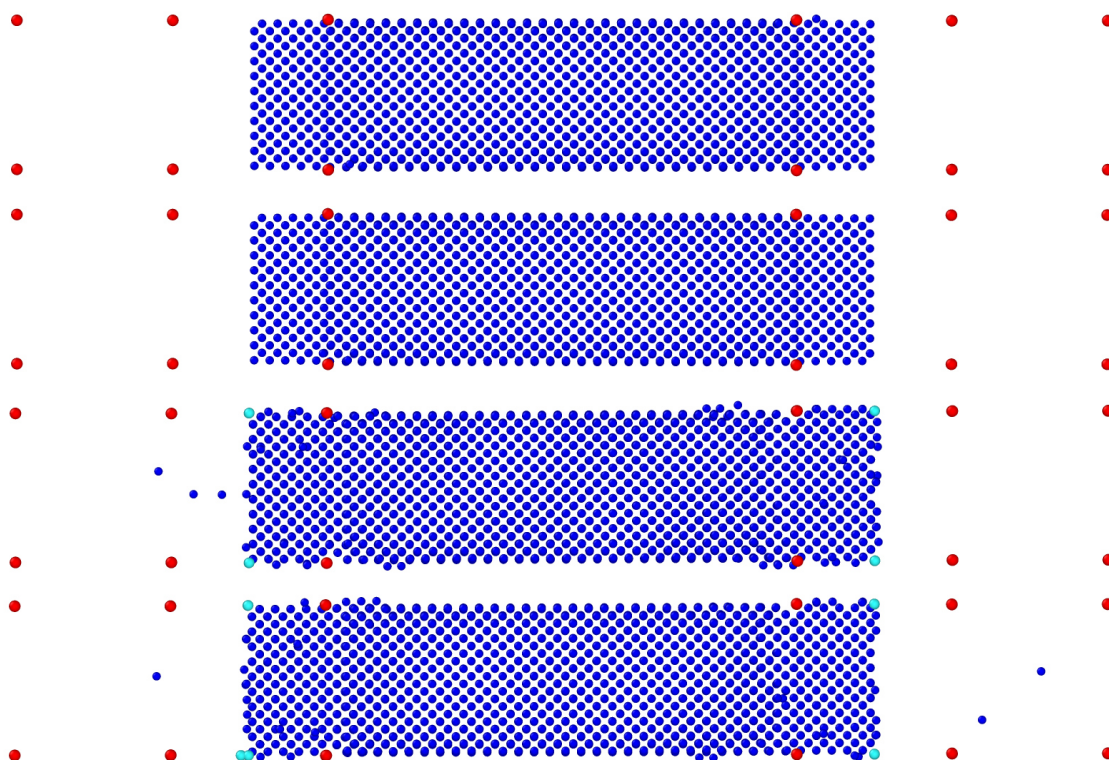
Figure 7.6: Deformation. Blue: atoms, red: finite element nodes, light blue: coupling subboxes corners. 1. row: Cauchy and cubic material law, 2. row: Cauchy and vertical coupling, 3. row: subboxes coupling and cubic material law, 4. row: subboxes coupling and vertical coupling

Clearly visible is that in the case of the subboxes coupling a few boundary atoms have changed position or lost contact with the surrounding atoms. The reason for that is that due to the subboxes, the free atoms are influenced by the vibration of the bound atoms but the reverse is not true, because the forces are redirected to the finite element nodes. Therefore, the free atoms are pumped with energy from the atoms from the subproblems. The thermostat cannot fully compensate for single atoms disturbing the temperature balance. This results in some atoms being kicked out of the system.

There are only small differences between 3.1 and 3.4 Å in displacement as seen in Figure 7.2. The x-displacement solution is 3.15 Å for the Cauchy rule with CML, 3.13 Å for the Cauchy rule with VC, 3.46 Å for the subboxes with CML and 3.40 Å for the subboxes with vertical coupling.

7.2.5 Discussion of results

In Figure 7.7 the convergence behavior of all previous 7 simulations is shown. The displacement is plotted as a function of the output steps. 100 samples where saved from each simulation and written to an output file. All methods converge. Case A and the subboxes coupling of Case B converge to the same value of approximately 3.4 Å, whereas the Cauchy type coupling converges to a displacement of 3.2 Å. The molecular dynamics is converging to approx 3.5 Å.
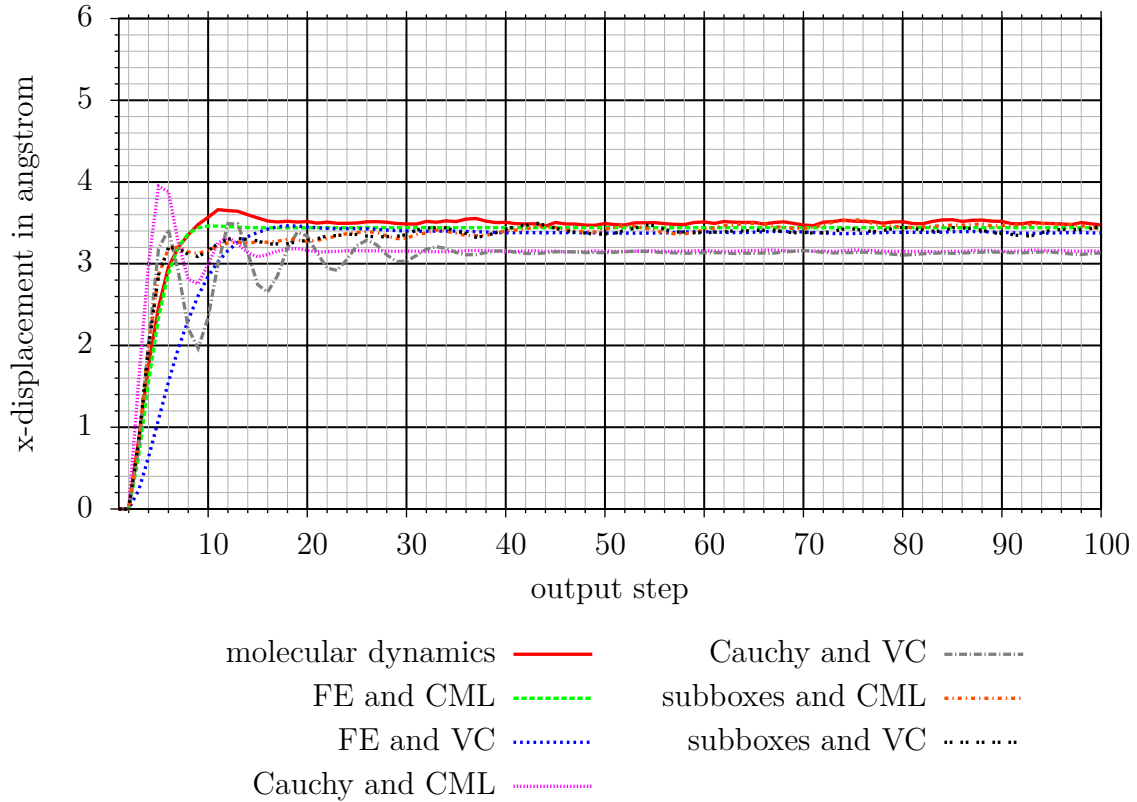
Figure 7.7: Convergence behavior tensile test, VC = vertical coupling, FE = finite elements, CML = cubic material law

The averaged values of the last 50 output steps can be seen in Table 7.2. The fixed Cauchy type coupling of molecular dynamics results in a higher stiffness than the coupling with subboxes which has the same displacement as the finite element solution with

the vertical coupling/cubic material law and is also very close to the molecular dynamics solution.

simulation	displacement value / Å	strain / percent
molecular dynamics	3.50	1.75
only FE & cubic material law	3.44	1.71
only FE & Vertical Coupling	3.38	1.68
Cauchy - cubic material law	3.15	1.57
Cauchy - Vertical Coupling	3.13	1.56
subboxes - cubic material law	3.46	1.72
subboxes - Vertical Coupling	3.40	1.70

Table 7.2: Tensile test case, displacement results

In the next chapter the pulling force will be replaced with a bending moment to simulate a bending problem with constant bending moment.

7.3 Bending test

The bending test has the same geometry as the tensile test described in the previous chapter. The forces are $F_1 = -F_2 = F = 0.6 \frac{\text{eV}}{\text{Å}}$, which is equivalent to a bending moment being applied to the right side of the beam. According to beam theory, this external bending moment should result in a constant bending moment throughout the beam. The hexahedron elements are using selective reduced integration of the nodal forces as described in Chapter 4.6.2 to avoid shear locking in the beam. The iron potential by MENDELEV ET AL. (2003) is used. The analytical solution of the vertical displacement at the end of the beam using a standard Euler-Bernoulli-beam formulation is

$$d_z = \frac{Ml^2}{2EI} = 14.7\,\text{Å}. \tag{7.8}$$

The Euler-Bernoulli solution is taken as a reference point.

7.3.1 Damping factor

In the dynamic simulation of a simple bending test, the question again arises to choose an appropriate damping factor. The relevant deformation frequencies can be estimated from an Euler-Bernoulli-Beam equation. This problem can be simplified by using one Euler-Bernoulli beam finite element that is fixed on the left. A simple 1D-Euler-Bernoulli beam with a density ρ_m, cross section A, length l and a stiffness EI has the following differential equation.

$$\frac{\rho_m Al}{420} \begin{bmatrix} 145 & 22l & 54 & -13l \\ 22l & 4l^2 & 13l & -3l^2 \\ 54 & 13l & 156 & -22l \\ -13l & -3l^2 & -22l & 4l^2 \end{bmatrix} \ddot{\mathbf{d}} + \frac{EI}{l^3} \begin{bmatrix} 12 & -6l & -12 & -6l \\ -6l & 4l^2 & 6l & 2l^2 \\ -12 & 6l & 12 & 6l \\ -6l & 2l^2 & 6l & 4l^2 \end{bmatrix} \mathbf{d} = \mathbf{F}. \tag{7.9}$$

If the left side of the beam is fixed, the equation simplifies to

$$\frac{\rho_m Al}{420} \begin{bmatrix} 156 & -22l \\ -22l & 4l^2 \end{bmatrix} \ddot{\mathbf{d}} + \frac{EI}{l^3} \begin{bmatrix} 12 & 6l \\ 6l & 4l^2 \end{bmatrix} \mathbf{d} = \mathbf{F}. \tag{7.10}$$

From this it can be derived that the eigenfrequencies are the square root of the eigenvalues of the expression

$$\frac{EI}{\rho_m Al^5} \begin{bmatrix} -252l & 192l^2 \\ -2016 & 1476l \end{bmatrix}. \tag{7.11}$$

With this, the lower eigenfrequency is found as

$$\omega = \sqrt{12(51 - 8\sqrt{39})\frac{EI}{\rho_m A l^4}}. \tag{7.12}$$

From the elastic constants matrix, Young's modulus E can be derived as $E = 133\,\text{GPa}$. The eigenfrequency ω is then equal to $\omega = 0.000305 \cdot (10.18\,\text{fs})^{-1}$. With $c_{\text{K}} = 1000$ the critical damping ratio of this mode using stiffness proportional damping only is $\zeta = \frac{\omega}{2}c_{\text{K}} = 0.15 < 1$.

7.3.2 Molecular dynamics solution

It was not possible to simulate a bending test with the molecular dynamics program IMD, because the solution did not converge to a static solution after a reasonable simulation time. Therefore, the horizontal coupling was used to simulate the bending problem with molecular dynamics. The dimensions of the problem are the same as in the tensile test. The damping coefficients are $c_M = 0.001$ and $c_K = 1000$. The simulation is performed with NumPro. The time step is 2 fs and 100,000 time steps are calculated. The problem is visualized in Figure 7.8.
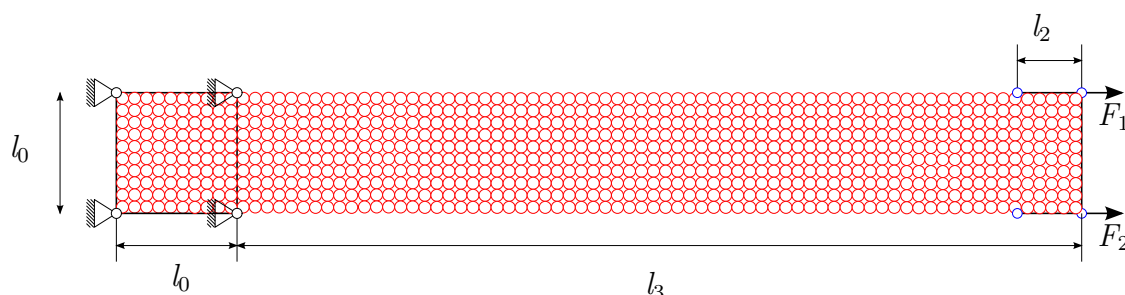
Figure 7.8: Bending test case with (mostly) pure molecular dynamics. The boundary conditions have been applied with horizontal coupling.
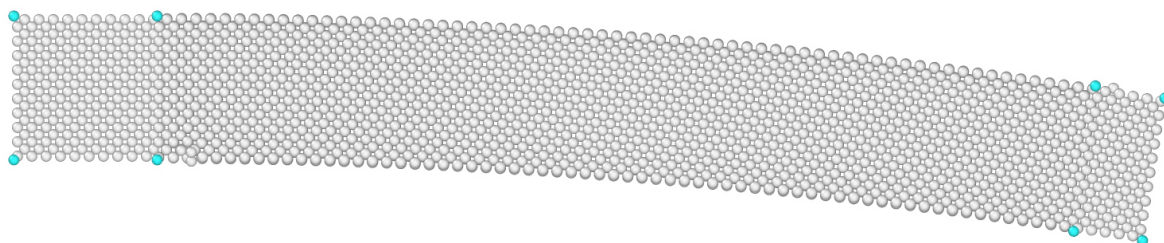
Figure 7.9: Results for the bending test using (mostly) molecular dynamics

The displacement on the lower right node with molecular dynamics is 16.1Å, the deformation is visible in Figure 7.9.

7.3.3 Case A

In Case A, two material laws as in the tensile test case are investigated. First a constant material tensor $\mathbf{C}$ is assumed with the elastic constants of the iron potential by MENDELEV ET AL. (2003). The second material law is the vertical coupling with the same potential.

Cubic material law

First case A is calculated. The material law is set to be the elastic tensor of the cubic material law of iron. All element edges align with the reference coordinate system. Therefore, no transformation of the elastic tensor is necessary. The elastic tensor is given as

$$
\mathbf{C} = \begin{bmatrix}
C_{11} & C_{12} & C_{12} & 0 & 0 & 0 \\
C_{12} & C_{11} & C_{12} & 0 & 0 & 0 \\
C_{12} & C_{12} & C_{11} & 0 & 0 & 0 \\
0 & 0 & 0 & C_{44} & 0 & 0 \\
0 & 0 & 0 & 0 & C_{44} & 0 \\
0 & 0 & 0 & 0 & 0 & C_{44}
\end{bmatrix}
\tag{7.13}
$$

with $C_{11} = 224$ GPa, $C_{11} = 126$ GPa and $C_{11} = 94$ GPa. The simulation is performed with NumPro. The damping coefficients are $c_M = 0$ and $c_K = 1000$. The time step is 2 fs and 200,000 time steps are calculated.

The deformation and stress are shown in Figure 7.10. The biggest deformation is 12.4 Å. The stress distribution is constant in horizontal direction and follows a linear profile in vertical direction with a maximum stress of $S_{xx} = 0.0088 \frac{\text{eV}}{\text{Å}^3}$.

Vertical coupling

Next, the vertical coupling is investigated. Instead of using the material tensor with the three constants C_{11}, C_{12} and C_{44}, at each Gauss point, a molecular dynamics subproblem is placed that returns the stress as a function of the strain $\mathbf{S} = \mathbf{S}(\mathbf{E})$. At each Gauss point, the molecular dynamics subproblem has a total of 128 atoms with a temperature of 300 K. The simulation is performed with NumPro. The damping coefficients are $c_M = 0$ and $c_K = 1000$. The simulation is performed with the NumPro code. The time step is 4 fs and 50,000 time steps are calculated.

0.14 Å

−12.4 Å

0.00886 $\frac{\text{eV}}{\text{Å}^3}$

−0.00869 $\frac{\text{eV}}{\text{Å}^3}$
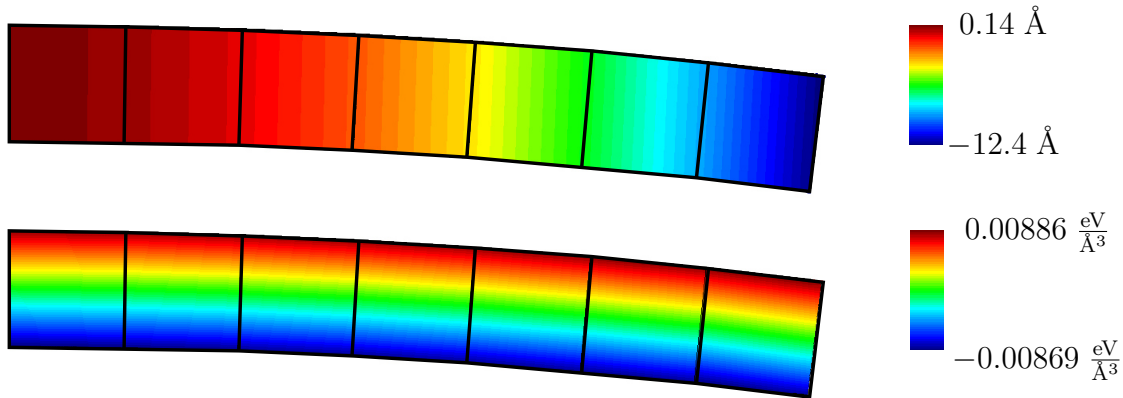
Figure 7.10: Results for the bending test using only finite elements and the cubic material law. On the top, the vertical deformation is seen and on the bottom, the second Piola-Kirchhoff stress S_{xx}

0.165 Å

−12.2 Å

0.00986 $\frac{\text{eV}}{\text{Å}^3}$

−0.00964 $\frac{\text{eV}}{\text{Å}^3}$
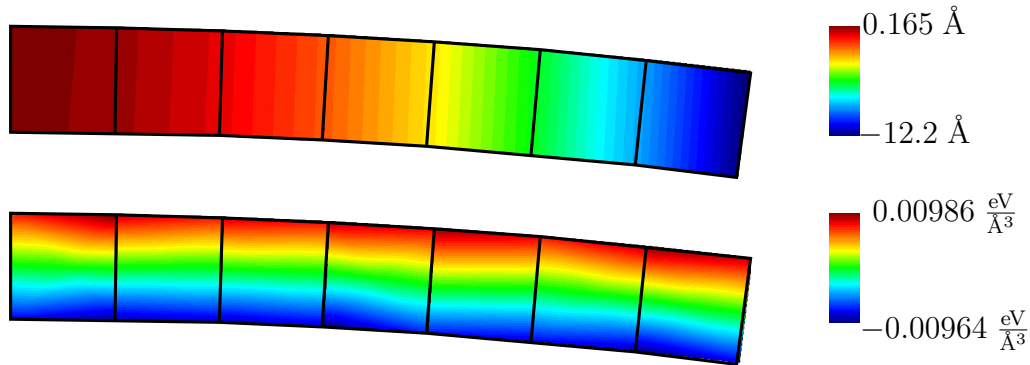
Figure 7.11: Results for the bending test using only finite elements and vertical coupling. On the top, the vertical deformation is seen and on the bottom, the second Piola-Kirchhoff stress S_{xx}

In Figure 7.11 the results are shown. In both cases, the deformation at the right end of the beam is nearly identical (-12.2 Å vs -12.4 Å). The simulation with the constant material matrix **C** shows a perfect stress distribution for the given load. In the case of the vertical coupling, small deviations are visible, but overall the stress is still very good. The stress values are 10 % higher in the case of the vertical coupling but this is believed to be caused by the fluctuating behavior of the stress in the subproblem. In fact, by taking into account the identical displacement, it can be deduced that the stress fluctuation is around 0.001 $\frac{\text{eV}}{\text{Å}^3}$ or 10% of the maximum stress value.

7.3.4 Case B

The second case consists of testing the horizontal coupling, using either the Cauchy rule or the subboxes coupling. In addition, on the finite element level either the cubic material law is used or the vertical coupling. The damping coefficients are $c_M = 0$ and $c_K = 1000$. The simulation is performed with NumPro. The time step is 4 fs and 100,000 time steps are calculated. Only in the last test case for subboxes and vertical coupling, a total of 400,000 time steps was computed to get to a quasi-static result.
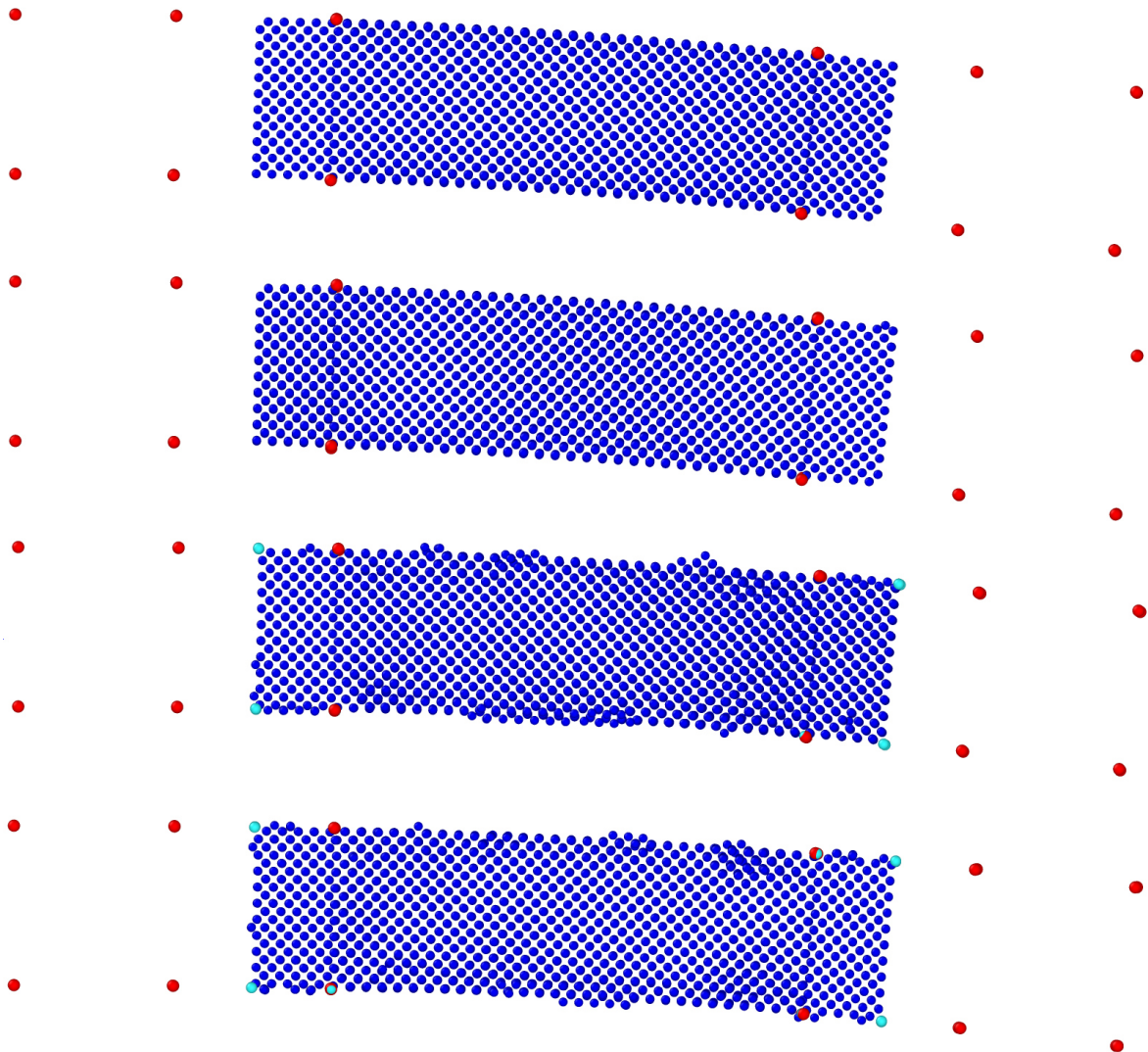
Figure 7.12: Bending deformation. Blue: atoms, red: finite element nodes, light blue: coupling subboxes corners. 1. row: Cauchy and cubic material law , 2. row: Cauchy and vertical coupling, 3. row: subboxes coupling and cubic material law, 4. row: subboxes coupling and vertical coupling

The results of these four combinations are shown in Figure 7.12. The two images at the top show a deformation behavior as expected. Noteworthy in the lower images are the atoms at the boundary that should not be there. These atoms are original from the interface between finite elements and molecular dynamics and are kicked out of position due to the thermal vibrations of the bound atoms in the subboxes coupling. The z-displacement solution at the end of the beam is -14.0 Å for the Cauchy rule with CML, -13.6 Å for the Cauchy rule with VC, -15.8 Å for the subboxes with CML and -10.4 Å for the subboxes with VC. The results are discussed in more detail in the next section.

7.3.5 Discussion of results

In Table 7.13 the convergence behavior is given. The displacement is plotted as a function of the output steps. 100 samples where saved from each simulation and written to an output file. All methods converge to a value, but not to the same value in all cases.
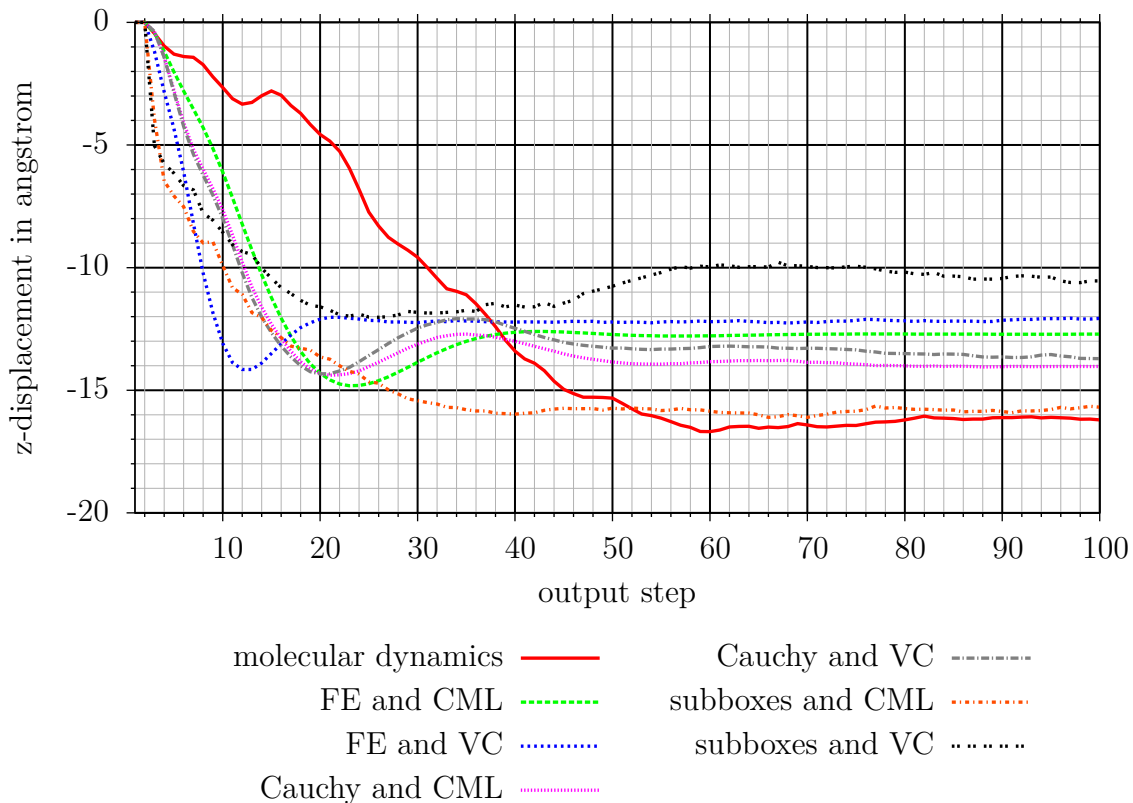
Figure 7.13: Convergence behavior bending test, VC = vertical coupling, FE = finite elements, CML = cubic material law

In Table 7.3 the results for all simulation runs are shown. In general it can be said that the vertical coupling has a higher stiffness than the constant material matrix. The solutions with finite elements only (Case A) show lower displacements and, therefore, a higher stiffness than the partitioned domain methods (Case B). The molecular dynamics solution has the highest displacement, which can be explained with the surface effects that reduce the stiffness of the beam. The subboxes with the cubic material law (CML) has a similar displacement to the molecular dynamics solution. However, this is believed to be a coincidence. It is more likely that a number of effects compensate each other. The finite elements have a higher stiffness compared to the pure MD solution as seen by Case A. This higher stiffness is probably compensated by the more flexible subboxes coupling type. In fact, it can be seen in figure 7.12 that some atoms are kicked out of position at the interface, resulting in a less stiff coupling. Whether this explains the complete stiffness loss must be further investigated. The Cauchy coupling does not lose atoms at the interface, resulting in a higher stiffness. In the case of the subboxes type coupling, used together with vertical coupling in the finite elements, the solution is very stiff and deviates significantly from the other solutions, especially the solution of the subboxes coupling with the cubic material law. The reason for this is unclear. As a great number of effects play an important role and the problem is calculated non-linear, this might be an effect of entering a different stability branch.

simulation	displacement value / Å
molecular dynamics	-16.1
only FE & cubic material law	-12.7
only FE & vertical coupling	-12.1
Cauchy - cubic material law	-14.0
Cauchy - vertical coupling	-13.6
subboxes - cubic material law	-15.8
subboxes - vertical coupling	-10.4

Table 7.3: Bending test case, displacement results

7.4 Phase transformation, single hexahedron

This example demonstrates phase transformation in a simple hexahedron as seen in Figure 7.14. The hexahedron is constrained at the bottom and has eight nodes. Vertical coupling is used to demonstrate phase transformation. There are eight integration points with eight subproblems. The simulation cube has dimensions of 10 x 10 x 10 mm. For each time step at the coarse scale there is a time step at the fine scale. The hexahedron uses full integration and not selective reduced integration. The force F_1 is applied to each of the four nodes on the top. In addition a second force F_2 is applied orthogonal to the the force F_1 on two sides of the cube, stretching the cube.

The simulation runs for a total of 6000 time steps. The time step is 0.00025 ms. The critical damping ratio is calculated as in the tensile test case and has a value of around $\zeta = 0.6$ for the deformation mode with the lowest frequency.
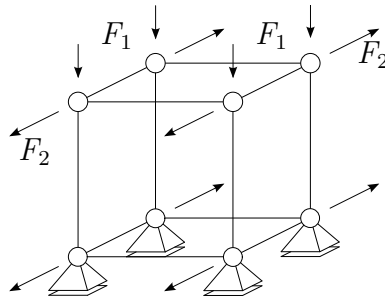
Figure 7.14: Stress free hexahedron

Phase transformation in both directions will be simulated with the potential for iron by MEYER AND ENTEL (1998) and the potential for titanium by MENDELEV ET AL. (2016).

7.4.1 Phase transformation from BCC to FCC

First, the transition from BCC to FCC is simulated. Figure 7.15 shows the atoms in BCC configuration. For the BCC configuration, the lattice constant at the start of the simulation is $a_{\mathrm{BCC}} = 2.85502\,\text{Å}$. It is important to note that the molecular dynamics lattice constants do not necessarily result in a stress free state at starting temperature. In this test case the starting temperature is 1600 Kelvin. The starting configurations for the molecular dynamics problems have 128 atoms each with a BCC lattice. The forces F_1 and F_2 are set to $F_1 = -12000$ N and $F_2 = 0$ N. The coefficients for the damping matrix are $c_M = 1.5$ and $c_K = 0.001$.
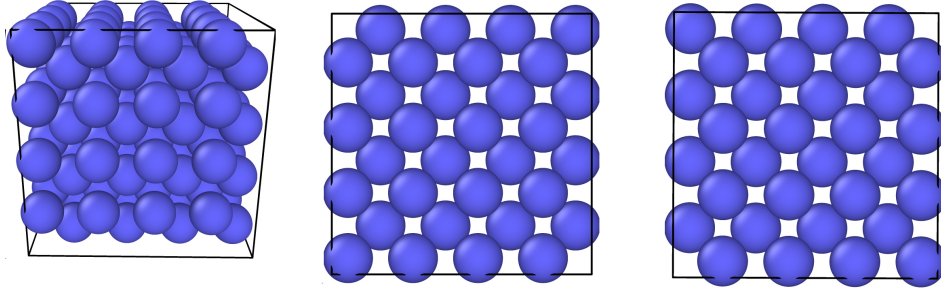
Figure 7.15: BCC lattice in starting configuration

Figure 7.16 shows the simulation results at the end of the simulation. The figure features eight rendered images of one MD subproblem each from the post-processing software Ovito. The color specifies the phase. Blue symbolizes BCC configuration, green FCC configuration and red HCP configuration. White atoms could not be associated with one of the previous lattice structures. The analysis is done using common neighbour analysis to identify atomic lattice structures, see FAKEN AND JÓNSSON (1994) for more details. The output atom positions are time averaged to increase the phase detection rate by the algorithm.

It can be seen that all subproblems changed to mainly green color, showing an excellent transformation result. A few atoms are still white, but this is due to the fact that the post processing software has problems analyzing atomic structure that has a non-perfect lattice because of thermal vibrations.

In Figure 7.17 the undeformed configuration (grey) and the deformed configuration (black) of the problem can be seen. The original length l_0 of the cube changed to the three side lengths l_1, l_2 and l_3.

The lengths are given in Table 7.4. The transition from BCC to FCC is a simple rescaling of axes. If the ratio of one length to the other two lengths changes from $1 : 1$ to $\sqrt{2} : 1$, the structure changes from BCC to FCC, as explained in Section 2.3. This can be observed from the values: $l_1/l_2 = l_1/l_3 = 1.43 \approx \sqrt{2}$. The difference to $\sqrt{2}$ might be explained by the fact that the problem is not unloaded after transition, so that a small elastic deformation is also present after transition. The volume increases by 13%, however, – as mentioned before – the volume at the initial configuration does not necessarily represent a stress free state, so the volume change is influenced by the starting configuration.
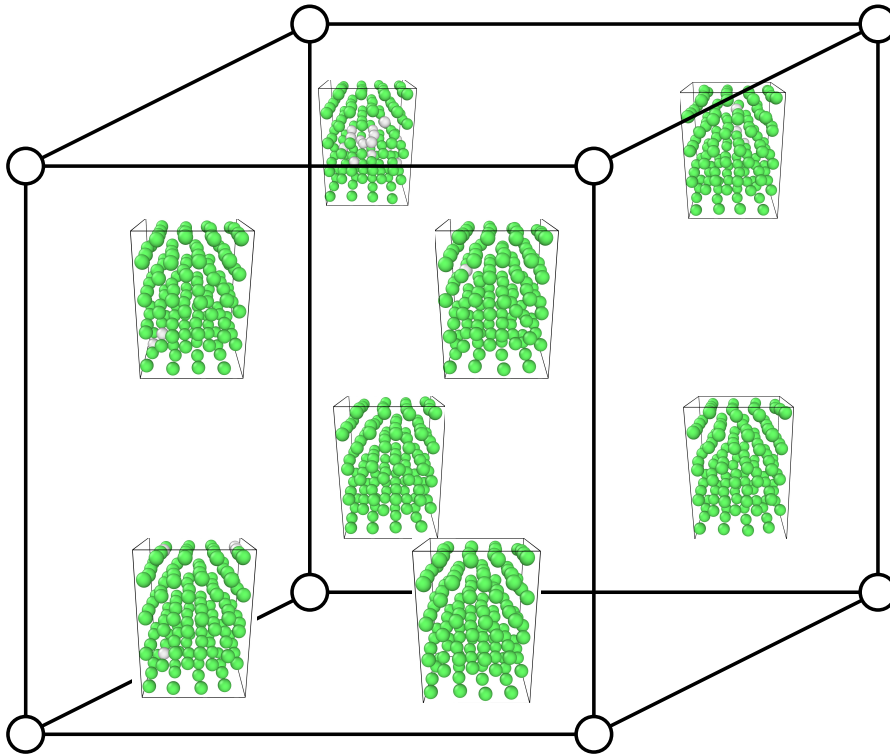
Figure 7.16: Stress free hexahedron, BCC to FCC, subproblems after transition
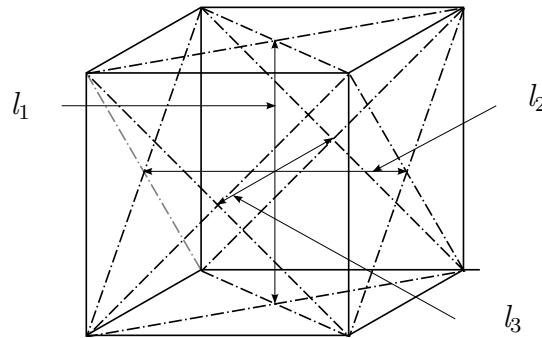
Figure 7.17: Simulation cube, results definition. l_1, l_2 and l_3 are always defined from the center of one side to the center of the opposite side.

length	result in mm
l_0	10
l_1	13.18
l_2	9.20
l_3	9.20

Table 7.4: Stress free hexahedron, BCC to FCC, deformation results

7.4.2 Phase transformation from FCC to BCC

Next, the transition from FCC to BCC is simulated. In this test case the starting temperature is 100 Kelvin. Figure 7.18 shows the atoms in FCC configuration. The FFC lattice constant is $a_{\text{FCC}} = 3.725$ Å. The molecular dynamics subproblems have 256 atoms each with a FCC lattice. Figure 7.18 shows the atoms of the subproblems in FCC starting configuration. A force F_1 is necessary in this case and is set to $F = 40,000$ N, which translates to a pressure of 1600 MPa. F_2 is not necessary and is set to $F_2 = 0$. The coefficients for the damping matrix are $c_M = 1.5$ and $c_K = 0.001$.
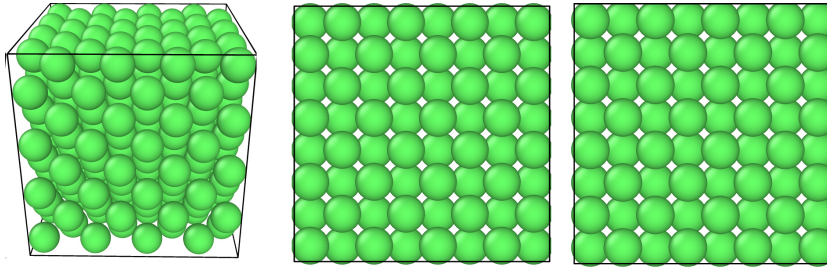

Figure 7.18: FCC lattice in starting configuration

Again, the results at the final time step are shown in figure 7.19. The color coding is th same as in the previous pictures with blue indicating BCC. As is clearly visible, all subproblems change to the BCC phase.

The length l_0 and three new lengths l_1, l_2 and l_3 are given in Table 7.5. The lengths are defined as in Figure 7.17. The transition from BCC to FCC is a simple scaling of axes. If the ratio of the axis changes from $1 : 1$ to $\sqrt{2} : 1$ the structure changes from BCC to FCC. This can be observed from the values. $l_1/l_2 \approx l_3/l_2 = 1.42 \approx \sqrt{2}$.

length	result in mm
l_0	10
l_1	11.04
l_2	7.80
l_3	11.05

Table 7.5: Stress free hexahedron, FCC to BCC, deformation results

Figure 7.19: Stress free hexahedron, FCC to BCC, subproblems after transition

7.4.3 Phase transformation from HCP to BCC

Next the transition from HCP to BCC is simulated with the titanium potential. In this test case the starting temperature is 1500 Kelvin. As starting configuration for the molecular dynamics subproblems a HCP lattice as seen in Figure 7.20 is selected. It consists of 216 atoms. The lattice constants for the HCP configuration of the potential are $a = 2.947$Å and $c/a = 1.597$. The forces are $F_1 = 0$ N and $F_2 = 70$ kN. The forces are unloaded after 600 time steps. The transition is initiated with pulling force in x-direction, otherwise the atoms do not change phase. Once in the BCC configuration, the lattice structure is stable again without boundary forces. The coefficients for the damping matrix are $c_M = 1000$ and $c_K = 1.0$.
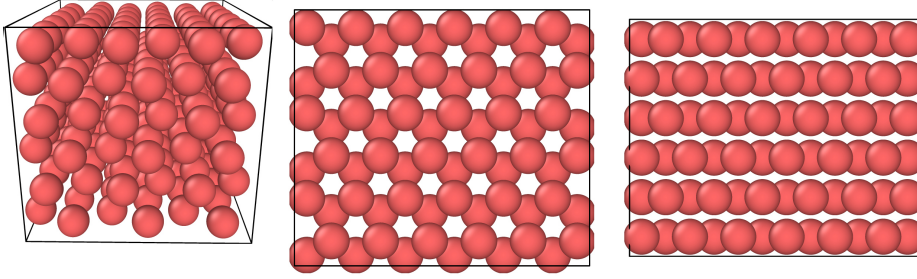
Figure 7.20: HCP in starting configuration

As can be seen in Figure 7.21, all subproblems change to a bcc structure. The subproblems have the same volume after transition with a lattice constant of $a = 3.29$ Å in bcc-phase.

length	result in mm
l_0	10
l_1	11.17
l_2	9.12
l_3	9.67

Table 7.6: Stress free hexahedron, HCP to BCC, deformation results

Table 7.6 shows the three new lengths l_1, l_2 and l_3. The lengths are defined just as in Figure 7.17. However, in this test case the ratio of initial lengths is different for the MD subproblems and for the finite element. Therefore, it is necessary to look at the deformation gradient $\mathbf{F}$. It can be seen that the deformation gradient of the problem after transformation is

$$\mathbf{F} = \begin{bmatrix} 1.117 & 0 & 0 \\ 0 & 0.9012 & 0 \\ 0 & 0 & 0.967 \end{bmatrix} \tag{7.14}$$
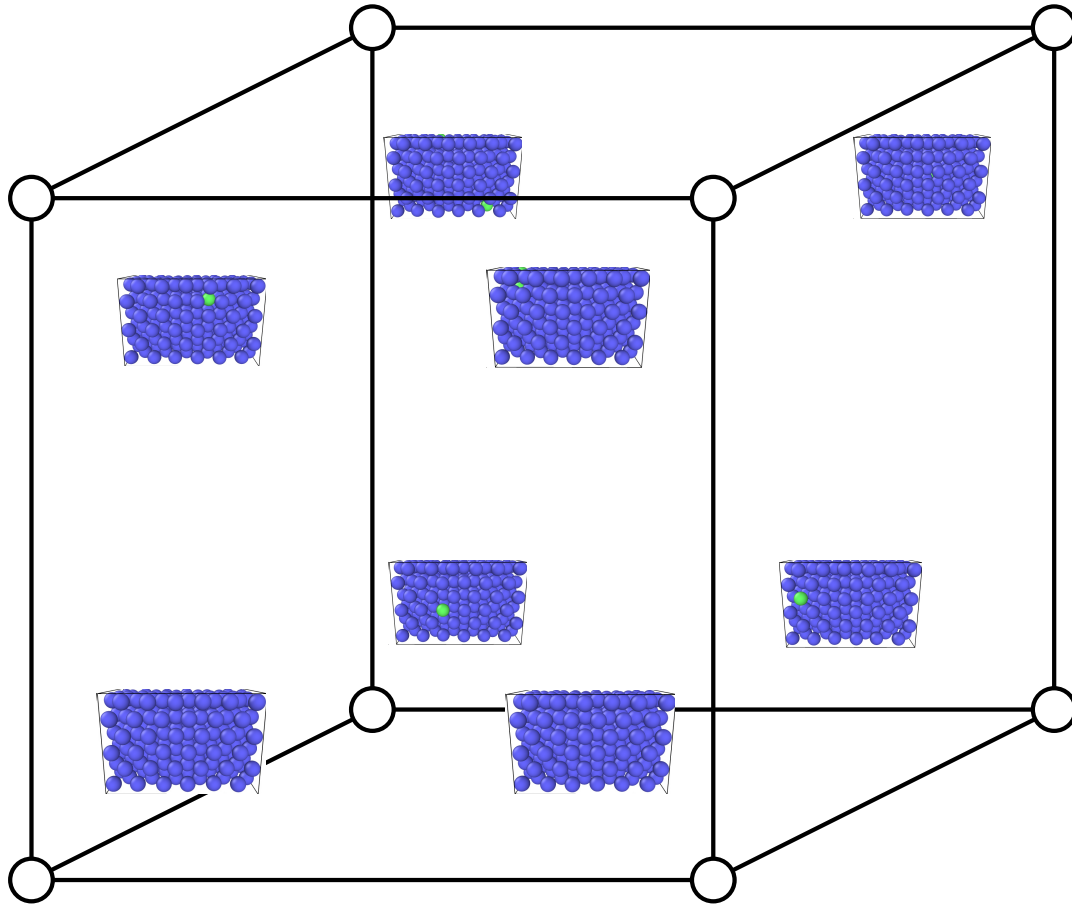
Figure 7.21: Stress free hexahedron, HCP to BCC, subproblems after transition

The initial lengths of the PBC box of MD subproblem are $\mathbf{L} = [35.364\,\text{Å} \quad 30.6261\,\text{Å} \quad 28.8746\,\text{Å}]^{\mathrm{T}}$. The deformed length is, therefore,

$$\mathbf{l} = \mathbf{F}\mathbf{L} = \begin{bmatrix} 39.49\text{Å} \\ 27.93\text{Å} \\ 27.92\text{Å} \end{bmatrix}. \tag{7.15}$$

Taking the ratio of the lengths, we arrive at $39.49\,\text{Å}/27.93\,\text{Å} = 1.414 \approx \sqrt{2}$, showing an excellent deformation result.

7.4.4 Phase transformation from BCC to HCP

Finally the transition from HCP to BCC shall be simulated. In this test case the starting temperature is 1000 Kelvin. As starting configuration for the molecular dynamics problems a BCC lattice, as seen in Figure 7.22, is selected. It consists of 432 atoms and a lattice constant $a = 3.29$ Å. The forces are unloaded after 600 time steps.
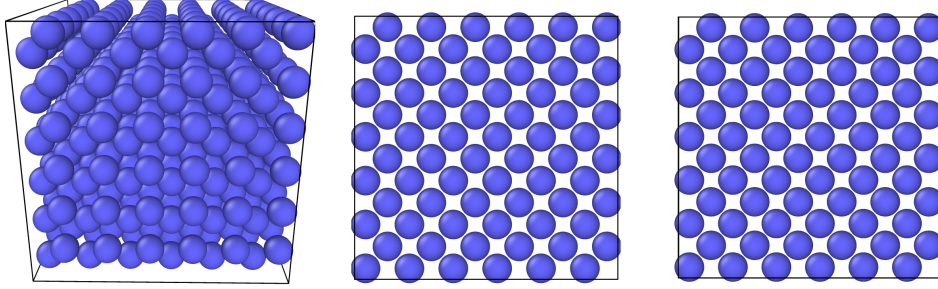
Figure 7.22: BCC in starting configuration

The transition is initiated with a compressive force in z-direction, $F_1 = -100$ kN and $F_2 = 0$ N. The coefficients for the damping matrix are $c_M = 1000$ and $c_K = 1.0$.

As can be seen in Figure 7.23, all subproblems change to a HCP structure. A few atoms are detected by the post processing software to be in the BCC phase but this is negligible.

vector	x-part	y-part	z-part
l_1	12.16	0	0
l_2	-1.15	12.11	0
l_3	0	0	10.25

Table 7.7: Stress free hexahedron, BCC to HCP, deformation results

Table 7.7 shows the three new lengths l_1, l_2 and l_3. The lengths are defined as in Figure 7.17. However, in this case they are interpreted as vectors in order to reflect the shear deformation. The box shows a small shear angle in the x-y-plane after the deformation. This has not been the case in previous phase transitions and is a result of the transition to HCP. The length l_z is proportional to the lattice constant a_{HCP} after transition, while the shorter diagonal in the x-y-plane is proportional to the layer distance c_{HCP}. This is due to the orientation of the lattice structure in the subproblem after transition. This can be seen in Figure 7.24. Therefore, it is possible to derive the ratio c/a from the coarse scale parameters.

$$\frac{c}{a} = \frac{\sqrt{(l_{1x} + l_{2x})^2 + l_{2y}^2}}{l_3} = 1.596. \tag{7.16}$$
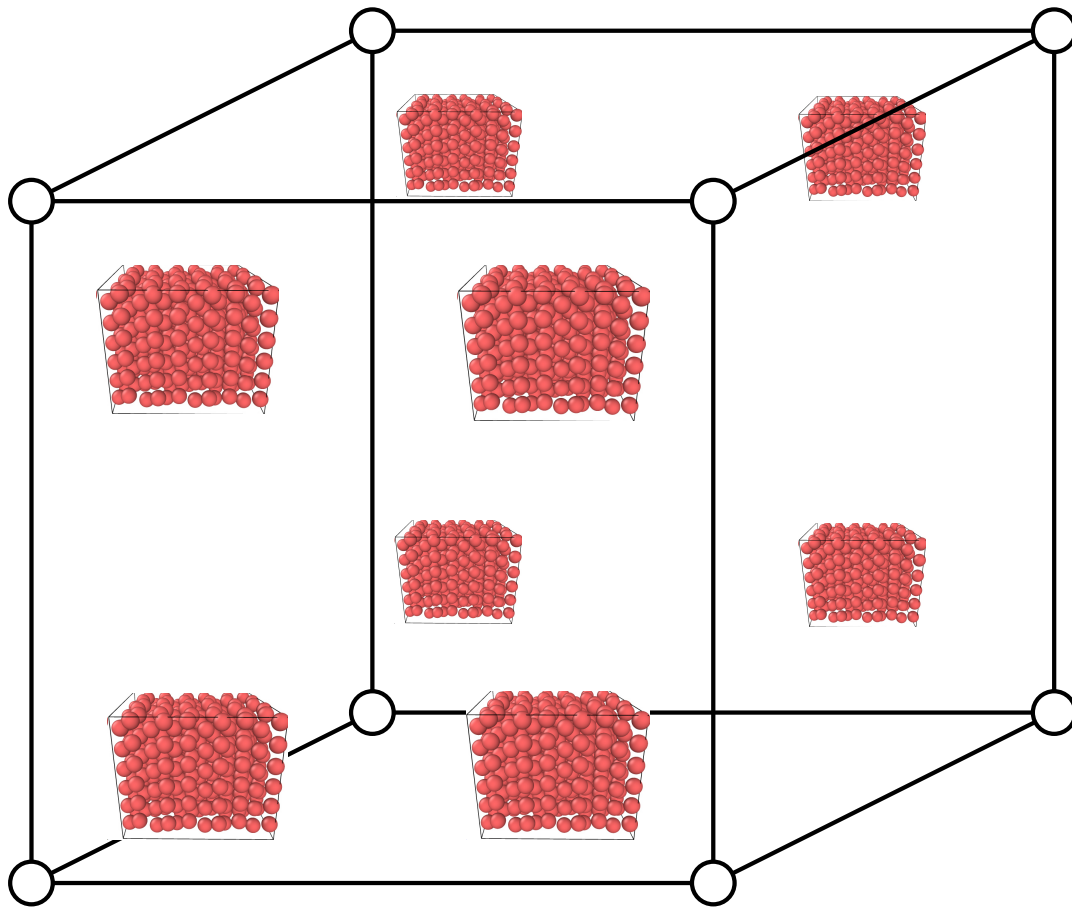
Figure 7.23: Stress free hexahedron, BCC to HCP, subproblems after transition
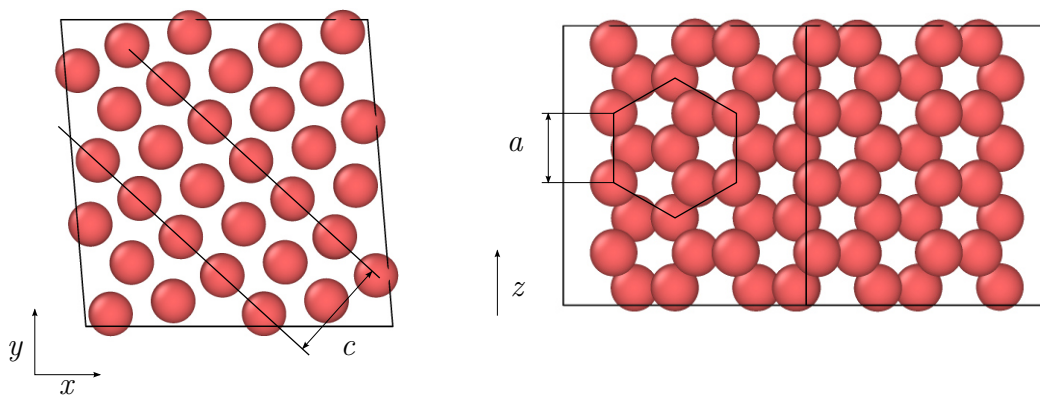
Figure 7.24: HCP subproblem orientation

This value is close to the theoretical value of 1.597 from MENDELEV ET AL. (2016).

7.4.5 Discussion of results

The phase transformation with the vertical coupling works well for a simple hexahedron. In all cases phase transformation takes place and the results show that all subproblems deform in the same manner. The post-processing software ovito recognizes nearly all atoms to be in the desired phase. The coarse scale deformation behavior of the hexahedron is in agreement with the subproblems. In addition the deformation is also in agreement with theoretical considerations, like the ratio of lengths discussed in Section 2.3.
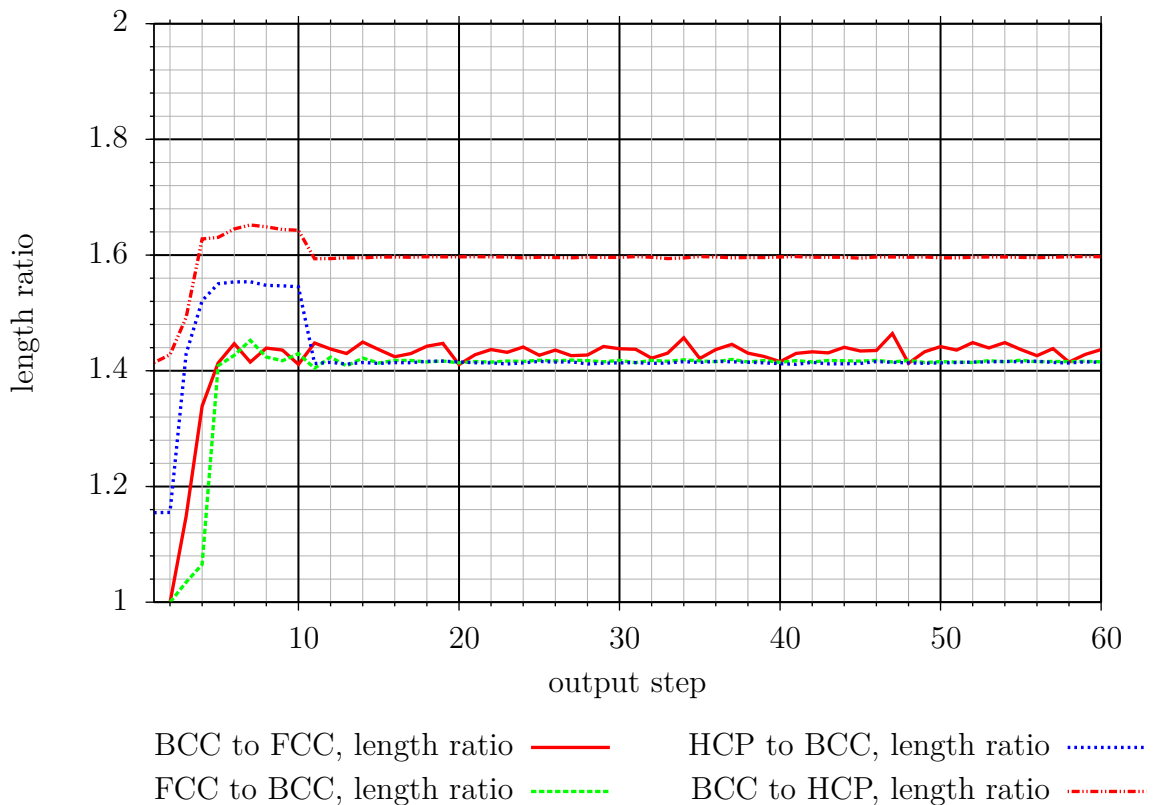
Figure 7.25: Convergence behavior, single hexahedron. In all transformations a fast convergence to the new lattice structure is visible.

Figure 7.25 shows the convergence behavior of the previous four simulations. In all cases a fast convergence behavior is visible. In the case of the BCC to FCC, FCC to BCC and HCP to BCC simulations, the ratio of the axis lengths of the box quickly converges to a value of approximately $\sqrt{2}$. The BCC to FCC value is a bit higher, because the simulation was not unloaded after initial transition. The BCC to HCP simulation converges to a value of 1.598, which is the ratio of the two lattice constants c/a of a HCP lattice.

A challenge remains due to the fact that the phase transformation could only be initiated by an initial force in some cases. However, this is believed to be an artefact of the EAM potentials and not caused by the proposed method.

In the following chapter all the phase transformation test cases are calculated again, this time however, in a combined simulation using both horizontal and vertical coupling.

7.5 Combined test case for phase transformation

In this test case both horizontal and vertical coupling are used to simulate phase transformation in a combined simulation. The problem setup can be seen in Figure 7.26. A box is discretized by 3x3x3 finite elements. The central finite element is removed and replaced by atoms as shown in the figure. On the left side of the figure an isometric 3D representation of the problem is seen, while on the right side a cut in the middle of the cube showing the x-y-plane is seen. In addition to the atoms in the center there are coupling atoms in the surrounding elements that are only shown in the right image for clarity.
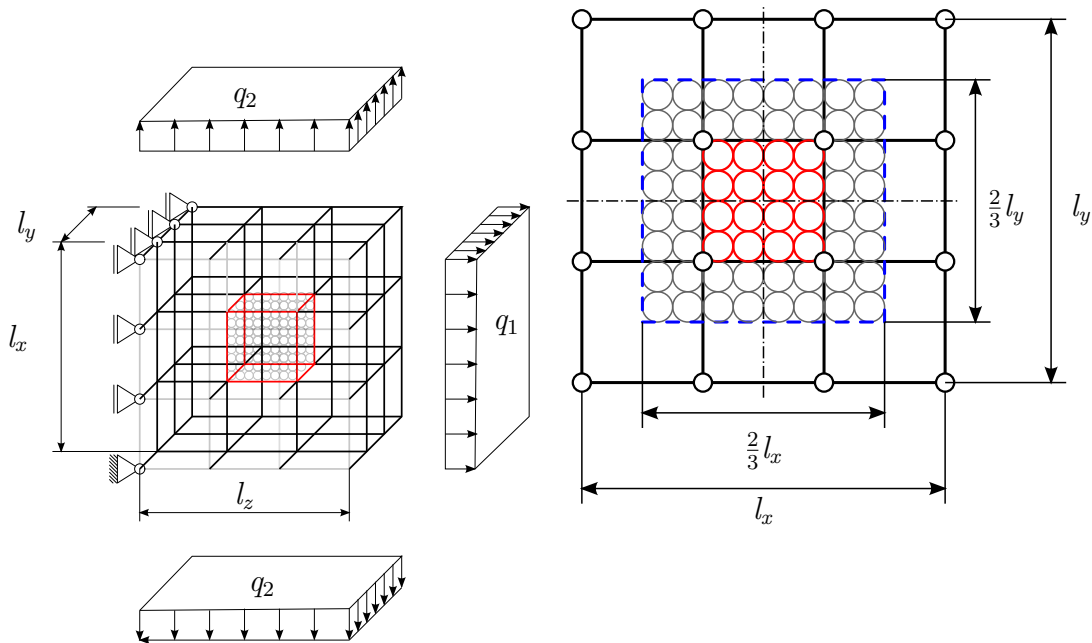
Figure 7.26: Combined test with 26 finite elements, center filled with atoms

The point of this problem setup is to exclude surface effects that play a significant role in molecular dynamics, but are unknown in continuum mechanics. By surrounding the atoms with finite elements the surface effects are eliminated.

The finite element mesh is constrained on the left side and is loaded on the right side with a distributed load q_1 and an additional load q_2 in x-direction. The loads are there to initialize or stabilize the phase transformation. In contrast to the previous test case, much higher loads are necessary to initiate the phase transformation in some simulations. The damping ratio ζ is calculated as in the tensile test case and $\zeta < 1$ for all simulations except for the HCP to BCC transformation, where it is above 1. However the damping does not prevent the phase transition.

The problems are run for a total of 10,000 time steps, if not specified differently. The time step is $\Delta t = 2$fs. The damping matrix has the coefficients c_M and c_K. The finite element used is the 8-node hexahedron. The density is $4.7 \frac{u}{Å^3}$ for iron and $2.8 \frac{u}{Å^3}$ for titanium. The cube has dimensions l_x x l_y x l_z. The corresponding values are different for each simulation.

The phase transformations that are simulated are the same ones as in the single hexahedron test case in Section 7.4 that used the vertical coupling only. However, this simulation is much more complex than in the previous cases. In addition, the calculation time is much higher due to the fact that in this simulation 26 finite elements with 8 subproblems per integration point must be simulated. These 208 subproblems require the majority of the calculation time. For this reason, the subproblems are chosen to be as small as possible. The MD subproblems are the same as in the previous test case with one hexahedron element only.

7.5.1 Phase transformation from BCC to FCC

The first transition to be simulated is the transition from BCC to FCC. The problem dimensions are as follows $l_x = 85.995$ Å, $l_y = 85.995$ Å and $l_z = 85.995$ Å. The loads are $q_1 = 0.03125 \frac{eV}{Å^3}$ and $q_2 = 0 \frac{eV}{Å^3}$. The damping coefficients are $c_M = 0.0001$ and $c_K = 0.01$.
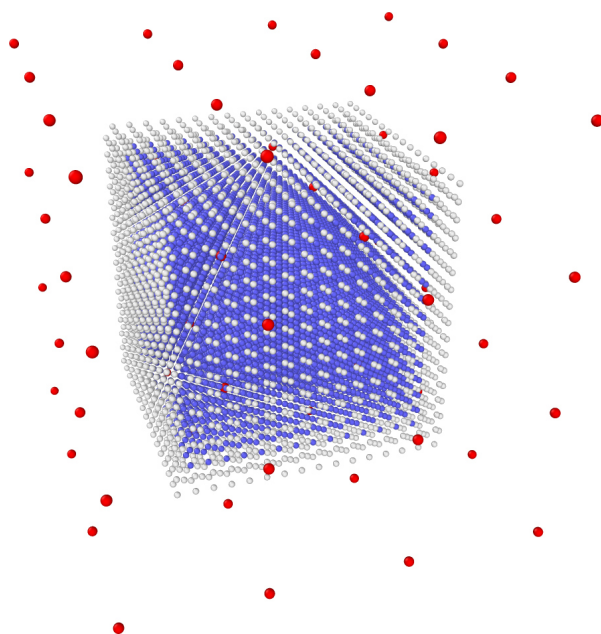
Figure 7.27: Finite element nodes (red) and atoms (blue and white). Atoms at the boundary are recognized by ovito to be in the BCC phase

The starting configuration can be seen in Figure 7.27. The simulation is run for a total of 20,000 time steps in the case of the Cauchy coupling and 50,000 time steps for the subboxes coupling. In the center there are 16,000 atoms with 2,000 being free atoms and the rest being the interface to the finite elements. Each finite element has a subproblem at each Gauss point with 256 atoms. The BCC lattice at the start has the same lattice constant both in the coupled atoms and in the subproblems. Therefore, the behavior of the material law in the finite elements is identical to the molecular dynamics.

The phase transformation from BCC to FCC shows excellent results in both methods. Figure 7.28 show the final configuration for the Cauchy rule and the subboxes respectively. In Table 7.8 the deformation results can be seen. The ratio of $106.2/74.9 = 1.42$

length	Cauchy	subboxes
l_0	85.995Å	85.995Å
l_1	74.6Å	74.9Å
l_2	74.6Å	74.9Å
l_3	105.4Å	106.2Å

Table 7.8: Combined test case, BCC to FCC, deformation results

and $105.4/74.6 = 1.41$ show good agreement with the expected length ratio of $\sqrt{2}$ for the FCC phase.

In Figure 7.28 the phases after transition are shown. All atoms (that are correctly recognized by ovito) are in the FCC phase. Due to the fact that the post-processing software does not recognize atoms at the boundary correctly, some atoms remain white. The numbers are shown in Table 7.9.

variable	initial	Cauchy	Subboxes
not recognized	27.1%	23.1%	23.4%
FCC	0%	77.0%	76.5%
HCP	0%	0%	0%
BCC	72.9%	0%	0%

Table 7.9: Combined test case, BCC to FCC, lattice structure distribution
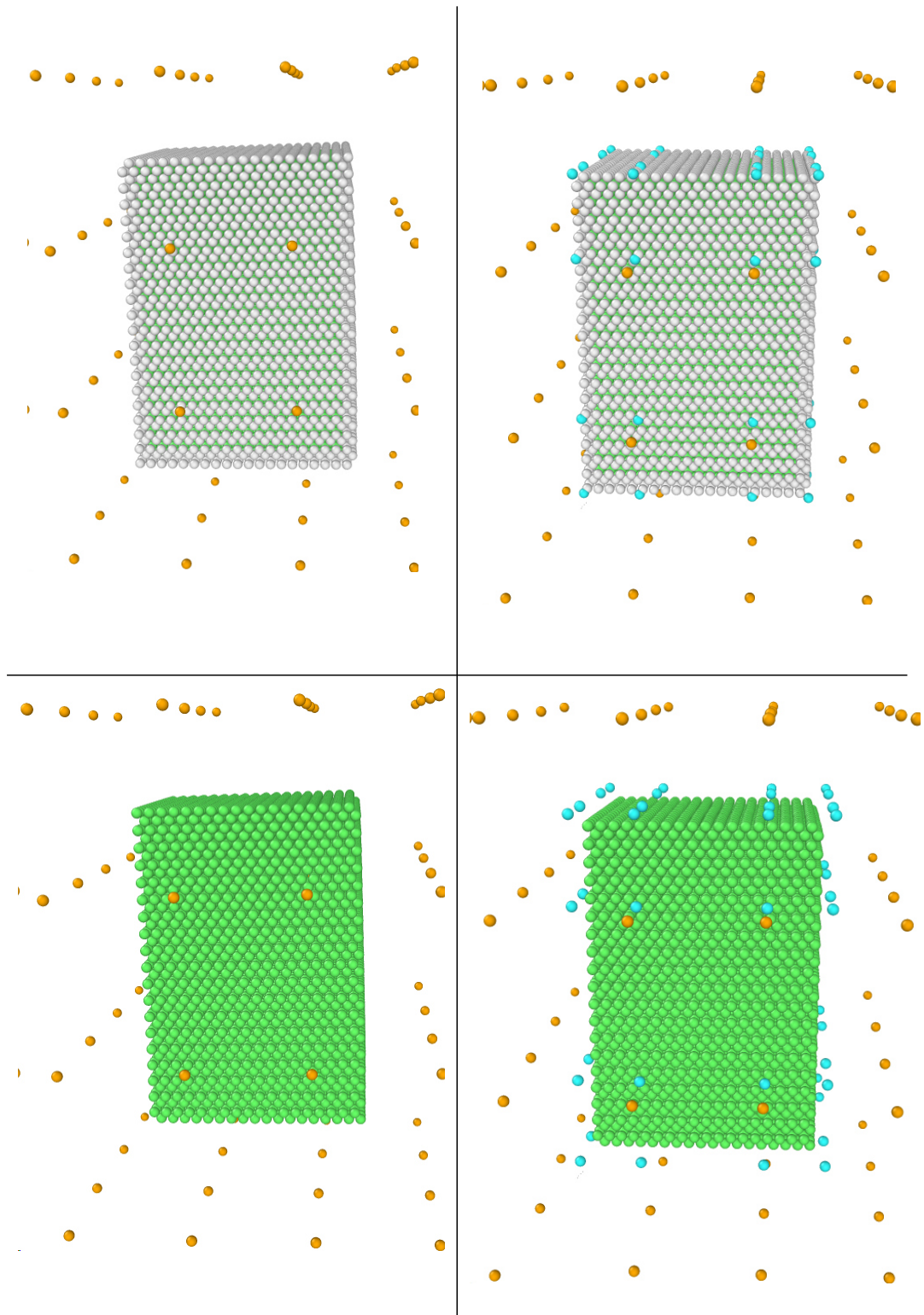
Figure 7.28: Results of the BCC to FCC transformation with the Cauchy rule on the left and the subboxes on the right. Visible are: FCC (green), not recognized (white), finite element nodes (yellow) and the subboxes nodes for horizontal coupling (light blue). Top row: all atoms, bottom row: FCC phase only. The MD subproblems from the vertical coupling are not visible in this picture.

7.5.2 Phase transformation from FCC to BCC

The second transition to be simulated is the transition from FCC to BCC. The problem dimensions are as follows: $l_x = 88.992\text{Å}$, $l_y = 88.992\text{Å}$ and $l_z = 88.992\text{Å}$. The loads are $q_1 = -0.003125\,\frac{\text{eV}}{\text{Å}^3}$ and $q_2 = 0\,\frac{\text{eV}}{\text{Å}^3}$. The damping coefficients are $c_M = 0.0001$ and $c_K = 0.01$.

The starting configuration can be seen in Figure 7.29. The simulation is run for a total of 10,000 time steps. In the center there are 16.384 atoms with 2.048 being free atoms and the rest being the interface to the finite elements. Each finite element has a subproblem at each Gauss point with 256 atoms. The FCC lattice at the start has the same lattice constant both in the coupled atoms and in the subproblems. Therefore, the material law in the finite elements is identical to the molecular dynamics.
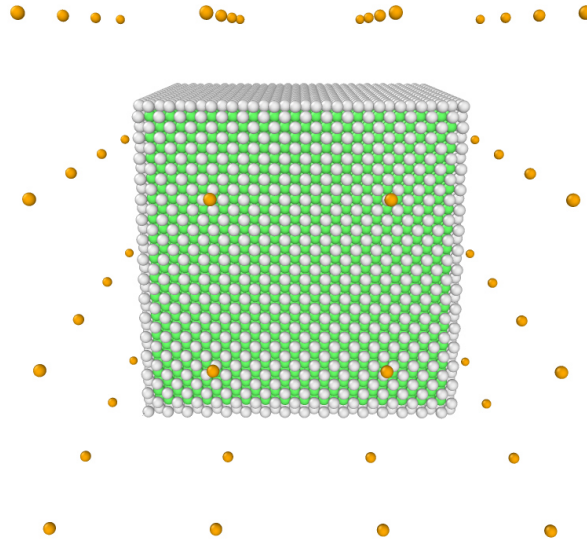
Figure 7.29: Finite element nodes (orange) and atoms (green and white). Atoms at the boundary are not recognized by ovito to be in the FCC phase

In Figure 7.30 the final configuration and the different phases can be seen. It is clearly visible that both simulations deliver a very good result. In the case of the Cauchy rule 76.9% of the atoms are recognized to be in the BCC phase and in the case of the subboxes as interface the deformation is nearly as good with 74.3% of the atoms. The numbers are shown in Table 7.11.

In Table 7.10 the final deformation results are shown. The length ratio after transition is $99.6\,\text{Å}/69.2\,\text{Å} = 1.44$ for the Cauchy coupling and $99.6\,\text{Å}/69.6\,\text{Å} = 1.42$ for the subboxes coupling. This fits with the visual interpretation of the lattice structure analysis in Figure 7.30. In both cases an excellent result is achieved for the transition. The small

length	Cauchy	Subboxes
l_0	88.992 Å	88.992 Å
l_1	99.6 Å	98.9 Å
l_2	99.6 Å	98.9 Å
l_3	69.2 Å	69.6 Å

Table 7.10: Combined test case, FCC to BCC, deformation results

difference to the exact value of $\sqrt{2}$ may be explained by the fact that the problem is not unloaded after transition.

variable	initial	Cauchy	Subboxes
not recognized	17.6%	23.1%	24.7%
FCC	82.4%	0%	0.7%
HCP	0%	0%	0.4%
BCC	0%	76.9%	74.3%

Table 7.11: Combined test case, FCC to BCC, lattice structure distribution
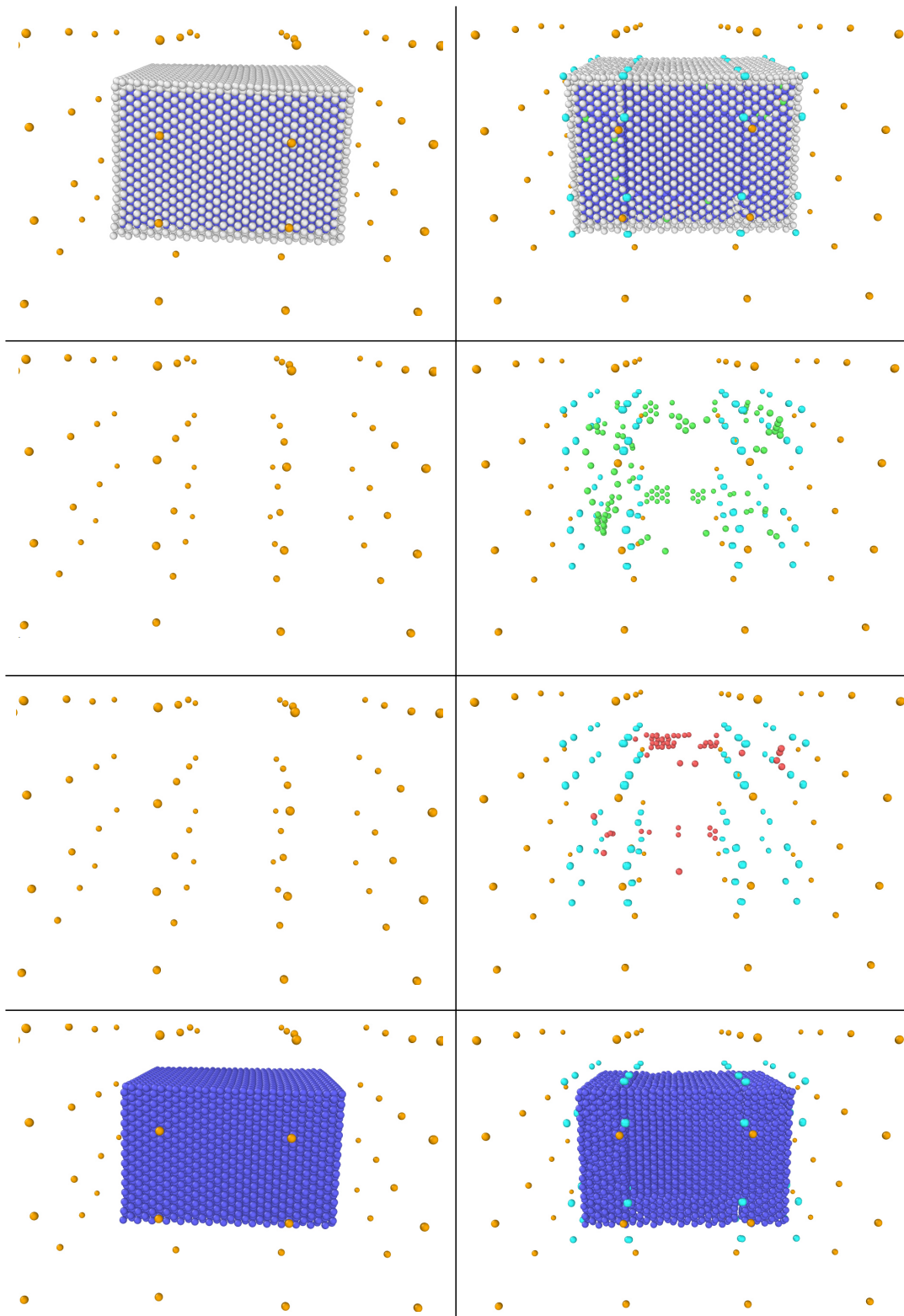
Figure 7.30: Results of the FCC to BCC transformation with the Cauchy rule on the left and the subboxes on the right. Visible are: BCC (dark blue), HCP (red), FCC (green), not recognized (white), finite element nodes (yellow) and the subboxes nodes for horizontal coupling (light blue). Top row: all atoms, second row: FCC only, third row: HCP only, fourth row: BCC only. The MD subproblems from the vertical coupling are not visible in this picture.

7.5.3 Phase transformation from HCP to BCC

The third transition to be simulated is the transition from FCC to BCC. The problem dimensions are as follows: $l_x = 106.092\,\text{Å}$, $l_y = 91.87848\,\text{Å}$ and $l_z = 86.62392\,\text{Å}$. The loads are $q_1 = 0\,\frac{\text{eV}}{\text{Å}^3}$ and $q_2 = 0.03125\,\frac{\text{eV}}{\text{Å}^3}$. A total of 50,000 time steps are simulated and the damping coefficients are $c_M = 0.05$ and $c_K = 0.5$. The titanium potential is used.

The starting configuration can be seen in Figure 7.31. In the center there are 13.824 atoms with 1.728 being free atoms and the rest being the interface to the finite elements. Each finite element has a subproblem at each Gauss point with 216 atoms. The FCC lattice at the start has the same lattice constant both in the coupled atoms and in the subproblems. Therefore, the material law in the finite elements is identical to the molecular dynamics.
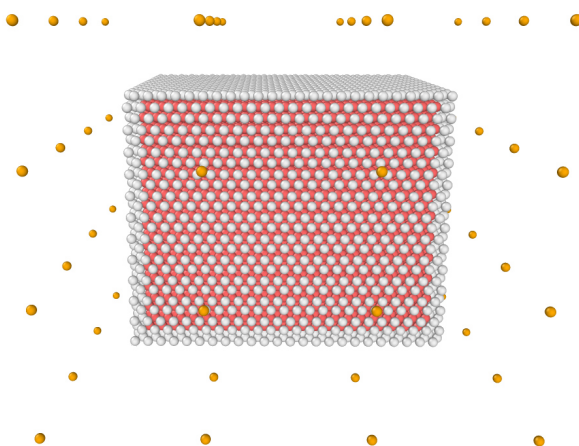
Figure 7.31: Finite element nodes (orange) and atoms (red and white). Atoms at the boundary are not recognized by ovito to be in the HCP phase

In Table 7.12 the deformation result is shown. In contrast to the transition with a single hexahedron only (see Section 7.4.3), in this case the ratio of lengths directly represents a BCC lattice that is rotated by 45along one of the main axes. Therefore, the ratio of the lengths directly correlates to $\sqrt{2}$. For the Cauchy rule $117.4\,\text{Å}/84.2\,\text{Å} = 1.39 \approx \sqrt{2}$ and for the subboxes $117.8\,\text{Å}/83.9\,\text{Å} = 1.40 \approx \sqrt{2}$. The lengths l_y and l_z should be the same, so a 3% error is visible in the simulation.

Table 7.13 shows the lattice structure results. The subboxes coupling enables also the coupling atoms to change phase as is clearly visible in Figure 7.32. The subboxes coupling has a slightly superior deformation result, but clearly the deformation is mostly dominated by the vertical coupling of the finite elements and the correct phase transformation of the coupling atoms plays only a small role in this case.
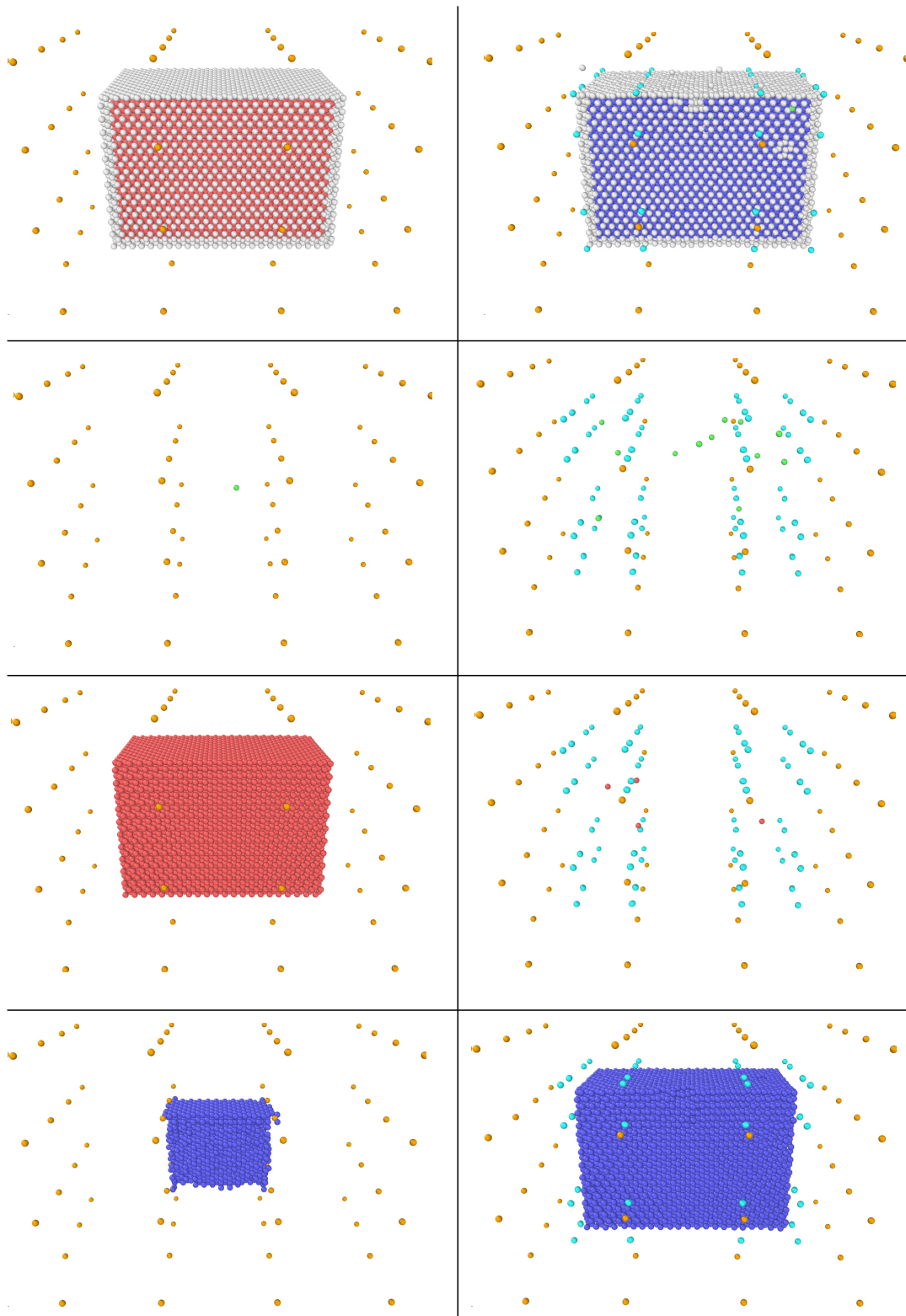
Figure 7.32: Results of the hcp to bcc transformation with the Cauchy rule on the left and the subboxes on the right. Visible are: BCC (dark blue), HCP (red), FCC (green), not recognized (white), finite element nodes (yellow) and the subboxes nodes for horizontal coupling (light blue). Top row: all atoms, second row: FCC only, third row: HCP only, fourth row: BCC only. The MD subproblems from the vertical coupling are not visible in this picture.

length	Cauchy	Subboxes
l_1	$117.4\,\text{Å}$	$117.8\,\text{Å}$
l_2	$84.2\,\text{Å}$	$83.9\,\text{Å}$
l_3	$86.1\,\text{Å}$	$86.0\,\text{Å}$

Table 7.12: Combined test case, HCP to BCC, deformation results

variable	initial	Cauchy	Subboxes
not recognized	23%	23.6%	26.3%
FCC	0%	0.0%	0.1%
HCP	0%	65.6%	0.0%
BCC	77%	10.8%	73.6%

Table 7.13: Combined test case, HCP to BCC, lattice structure distribution

7.5.4 Phase transformation from BCC to HCP

The last transition to be simulated is the transition from BCC to HCP. The problem dimensions are as follows: $l_x = 78\,\text{Å}$, $l_y = 78\,\text{Å}$ and $l_z = 78\,\text{Å}$. The loads are $q_1 = -0.025\,\frac{\text{eV}}{\text{Å}^3}$ and $q_2 = 0\,\frac{\text{eV}}{\text{Å}^3}$. The damping coefficients are $c_M = 0.0001$ and $c_K = 0.01$. The titanium potential is again used.

The starting configuration can be seen in Figure 7.33. The simulation is run for a total of 10,000 time steps. In the center there are 8.192 atoms with 1.024 being free atoms and the rest being the interface to the finite elements. Each finite element has a subproblem at each Gauss point with 256 atoms. The BCC lattice at the start has the same lattice constant both in the coupled atoms and in the subproblems. Therefore, the material law in the finite elements is identical to the molecular dynamics.
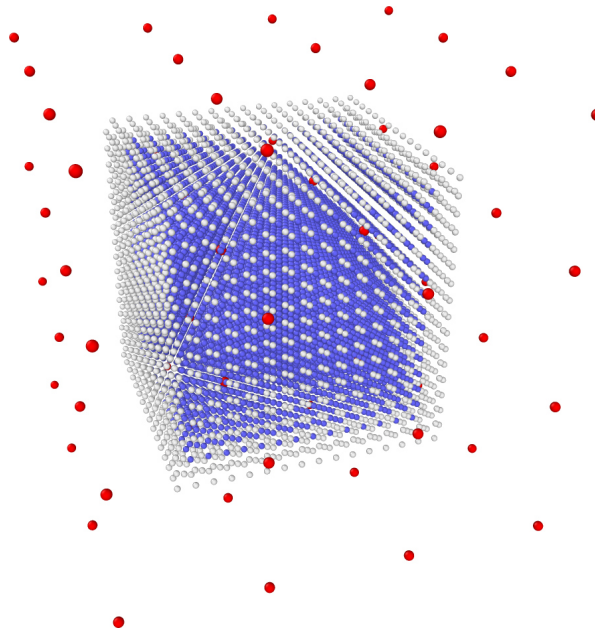
Figure 7.33: Finite element nodes (red) and atoms (blue and white). Atoms at the boundary are not recognized by ovito to be in the BCC phase

The results can be seen in Figure 7.34. The two cases clearly show a different deformation behavior. Only the subboxes coupling shows clear deformation to HCP. In the case of the Cauchy coupling, even the atoms in the center stay in the BCC phase and the deformation does not show a homogeneous result.

In the case of the Cauchy coupling only 0.1% of the atoms are detected to change phase to HCP, but 40.9% transform to the HCP phase for the subboxes coupling as in Table 7.14. A small percentage of FCC is also present. For the subboxes coupling only 0.9%
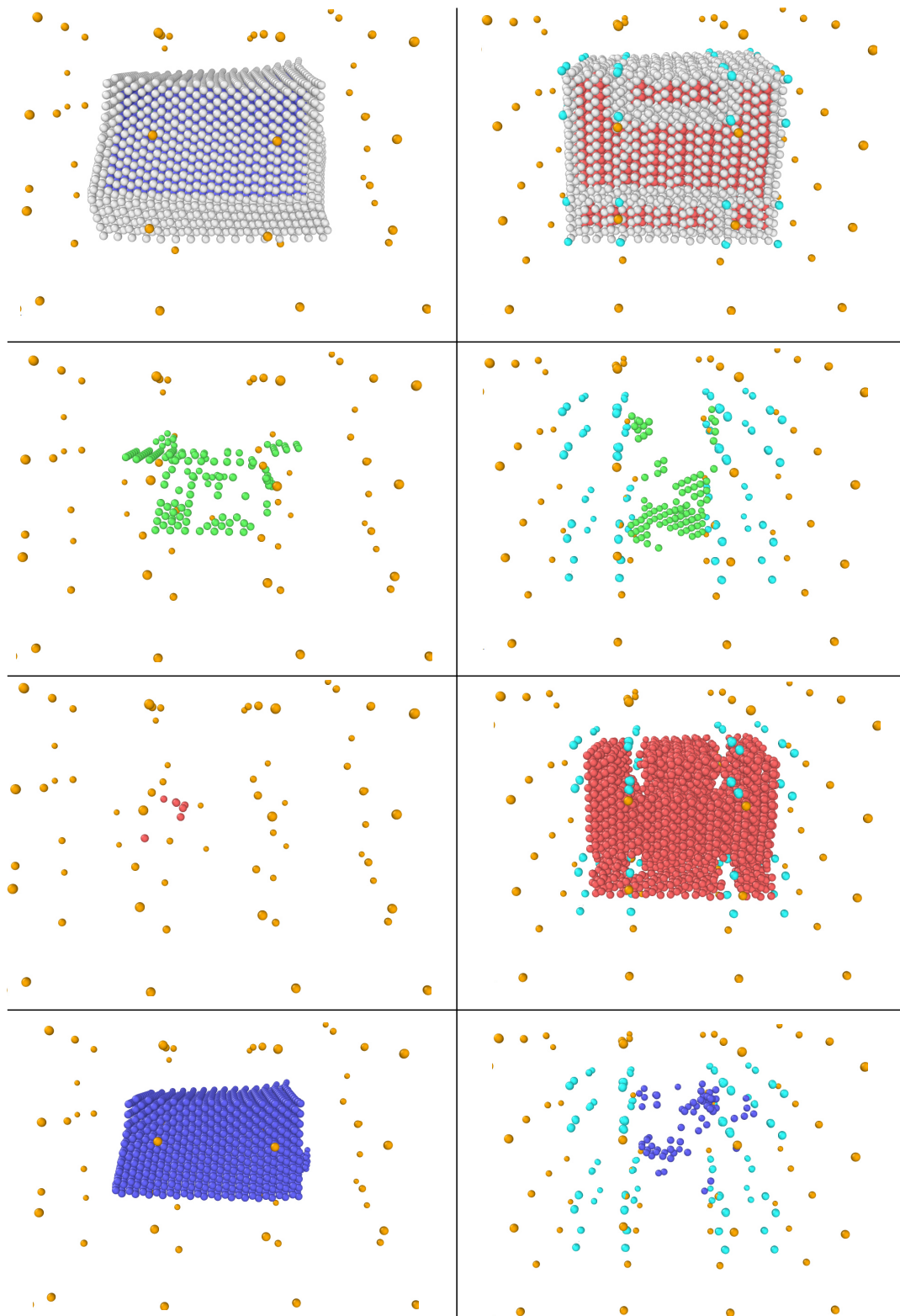
Figure 7.34: Results of the HCP to BCC transformation with the Cauchy rule on the left and the subboxes on the right. Visible are: BCC (dark blue), HCP (red), FCC (green), not recognized (white), finite element nodes (yellow) and the subboxes nodes for horizontal coupling (light blue). Top row: all atoms, second row: FCC only, third row: HCP only, fourth row: BCC only. The MD subproblems from the vertical coupling are not visible in this picture.

of the atoms remain in the BCC phase. As far as phase transformation is concerned, the subboxes coupling is by far superior.

variable	initial	Cauchy	Subboxes
not recognized	33%	69.4%	56.9%
FCC	0%	1.7%	1.2%
HCP	0%	0.1%	40.9%
BCC	67%	28.8%	0.9%

Table 7.14: Combined test case, BCC to HCP, lattice structure distribution

When looking at the deformation results, equation (7.16) from the single hexahedron test case should still hold true. However, in this case a slight shear deformation is not visible. The equation then becomes

$$\frac{c}{a} = \frac{\sqrt{l_x^2 + l_y^2}}{l_z}. \tag{7.17}$$

Entering the values of the table we arrive at 2.13 for the Cauchy coupling and 1.75 for the subboxes coupling. The expected value is 1.597. In both cases this value is not reached, however, the subboxes coupling is only 10% off, while the Cauchy coupling is 33% off and is still not a converged solution, as can be seen in Figure 7.35 in the next section.

length	Cauchy	Subboxes
l_0	78 Å	78 Å
l_x	90.8 Å	84.6 Å
l_y	89.9 Å	84.3 Å
l_z	60.1 Å	68.23 Å

Table 7.15: Combined test case, BCC to HCP, deformation results

7.5.5 Discussion of results

Figure 7.35 shows the convergence of the length ratio as a function of output steps of all eight simulation runs.
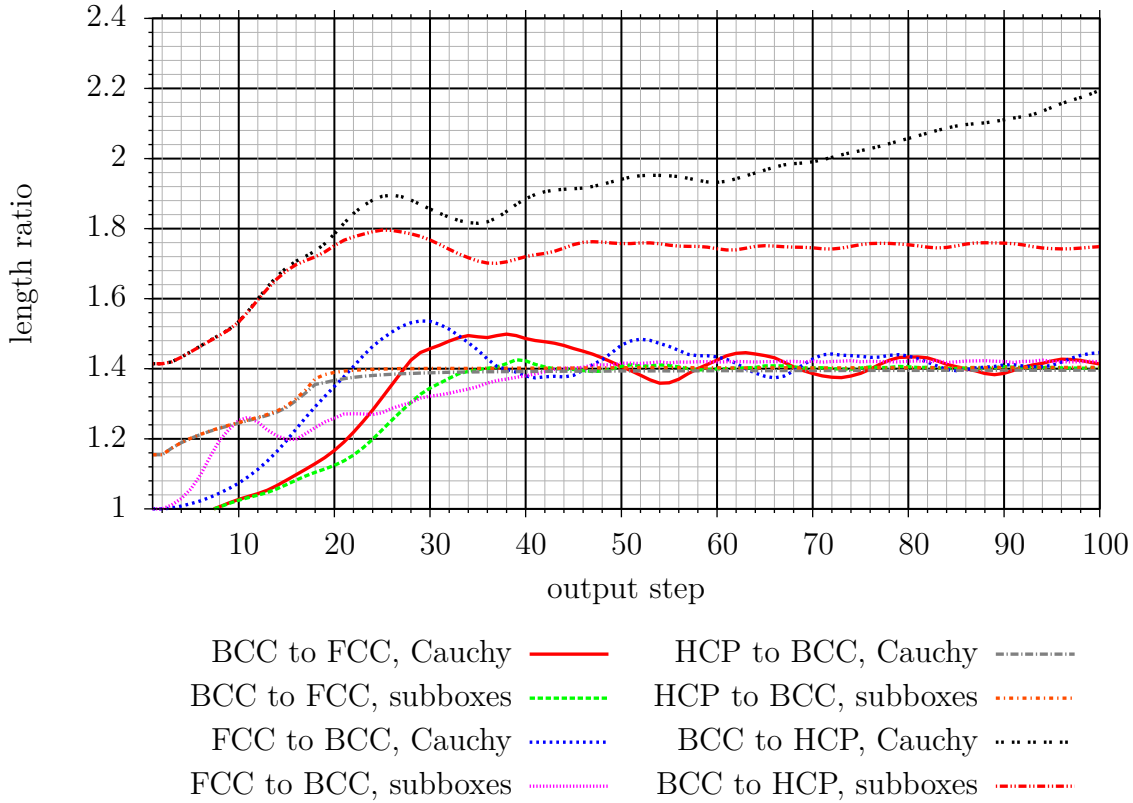
Figure 7.35: Convergence behavior combined test case

In the case of the BCC to FCC transition both Cauchy and subboxes coupling methods yield satisfactory results. All atoms change to FCC structure. The convergence of the length ratio to $\approx \sqrt{2}$ is clearly seen in the Figure 7.35.

In the case of the FCC to BCC transition, both coupling methods show very good results, converging to $\approx \sqrt{2}$. However, the convergence of the subboxes is a bit slower and more time steps are necessary to converge to the correct result.

In the case of the HCP to BCC transformation, both methods showed approximately the same deformation. However, in the case of the subboxes coupling the coupling atoms were also able to change phase, in the Cauchy case they stayed in the HCP phase. The length ratios of both simulations converge to a value close to $\sqrt{2}$. If the volume of the free atoms in the center is increased, there might be a bigger difference between the deformation of the two methods.

In the case of the BCC to HCP coupling, the subboxes coupling shows a far superior result. The Cauchy coupling does not show a homogeneous transformation and also only minimal HCP lattice structure is detected by the post-processing software. Although both length ratios do not converge to the expected result of 1.597, the subboxes coupling is much closer to the expected value with only a 10% difference. The Cauchy coupling does not converge.

7.6 Summary

In this chapter a total of four test cases were performed. The methods investigated were finite elements with a cubic material law, finite elements with the vertical coupling, the two horizontal coupling methods (Cauchy rule and subboxes) combined with either the cubic material law or the vertical coupling in the finite elements and of course a molecular dynamics solution. In the first case a simple tensile test was performed, where all methods show satisfactorily results. Apart from the Cauchy coupling, which shows a stiffer response, all other solutions are close to each other and in agreement with the cubic material solution, which is calculated with finite elements only and the material derived from the elastic constants. The Cauchy solution is off by about 9%. Still this is overall a good result.

In the case of the bending test case the same methods were compared as in the tensile test. However, results deviate much more from each other. First, it is important to note that a bending problem is much more difficult, even from an analytical point of view. Depending on the theory (e.g. Euler-Bernoulli or Timoshenko), the results can vary greatly. In addition, using finite elements, the solution can be difficult to compute due to locking effects. In this test case an additional challenge is the molecular nature of the problem, introducing boundary effects in the molecular dynamics solution, resulting in a larger displacement. Furthermore, the molecular dynamics solution is not computed with an external molecular dynamics code (like IMD) due to challenges with the boundary conditions and with the convergence to a quasi-static solution. Taking the molecular dynamics solution of $-16.1\,\text{Å}$ as the correct solution, the multiscale solutions deviate up to 35% compared to the molecular dynamics solution. Except for the subboxes coupling method, the difference between using the cubic material law and the vertical coupling in the finite elements is small. The subboxes combined with the vertical coupling shows the stiffest result and one might question, whether it is actually correct. A possible explanation might be, that the atomic vibrations from the vertical coupling influences the result, but this has to be further investigated. Using only finite elements the solutions is very stiff with the result deviating by 21-25% from the molecular dynamics solution. The Cauchy solution is less stiff, deviating only 13-16% from the molecular dynamics solution. The best solution is the subboxes type coupling with the cubic material law, resulting in only a 2% deviation from the molecular dynamics solution. However, this may also be a coincidence and more analysis is required.

Finally, phase transformation between BCC and FCC, FCC and BCC, HCP and BCC and BCC and HCP was simulated. The simulation was first done using only one hexahedron element and vertical coupling. Following this simulation, the phase transforma-

tions were simulated again using both vertical and horizontal coupling. In Figure 7.36 all transformation results are summarized.
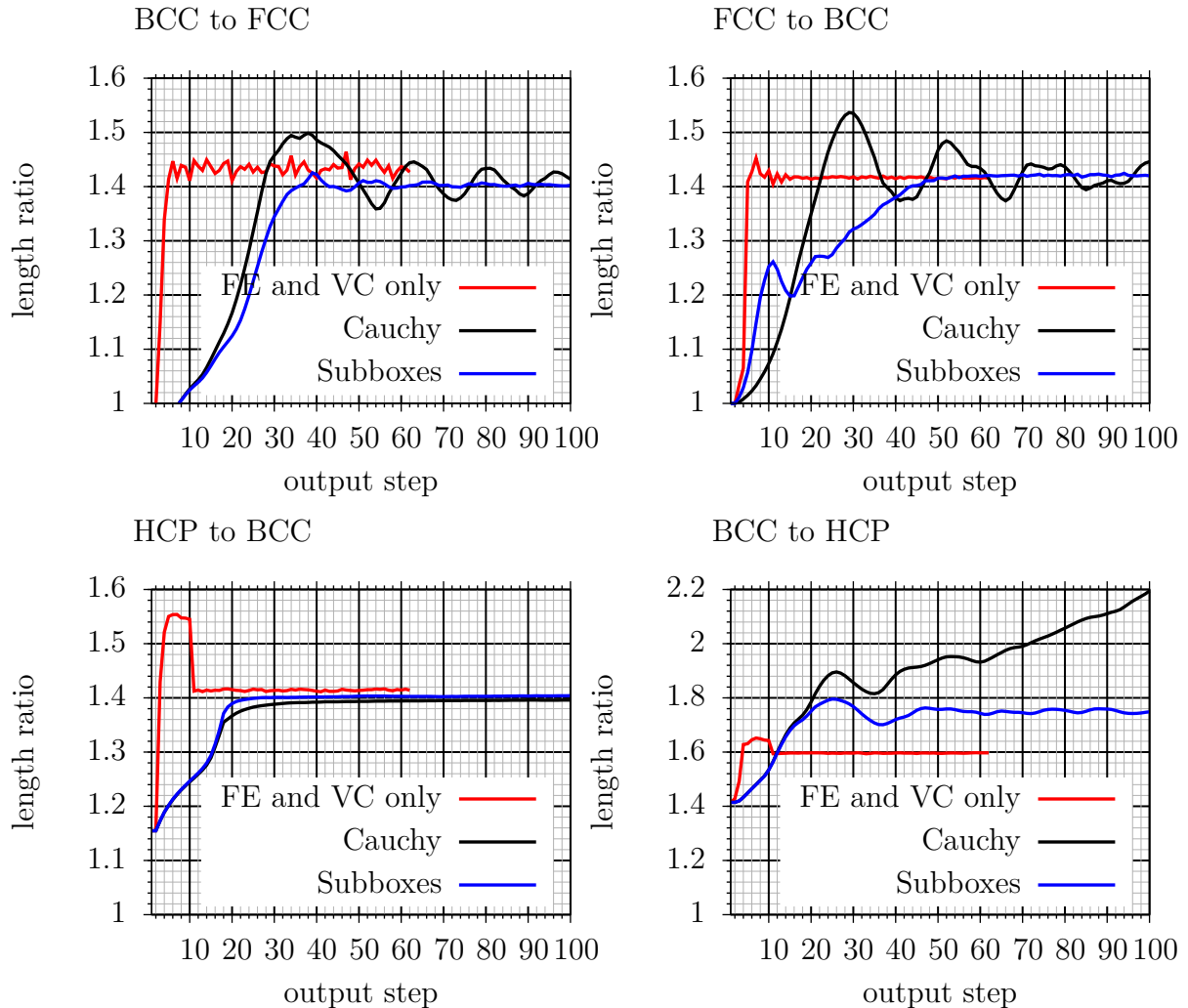
Figure 7.36: Comparison of the convergence of different methods sorted by transformation

In the case of the BCC to FCC transition, all simulations converge to the theoretically expected value of $\approx \sqrt{2}$, showing in general a very good transformation result. As the transition only involves a rescaling of the axis, the Cauchy coupling has no problems with this transition. The next transition is the transition from FCC to BCC. In this case, the single hexahedron with the vertical coupling transforms as expected, the length ratio converges to a value close to $\sqrt{2}$, as seen in the figure. The Cauchy and subboxes solution also transform as expected with nearly all atoms changing to BCC phase as seen in Figure 7.30. The last two transitions to be investigated were the transitions between HCP and BCC in titanium. In the case of HCP to BCC, the length ratio converges for

all simulation to a value close to $\sqrt{2}$. However, as seen in Figure 7.32, it is impossible for the bound atoms in the Cauchy coupling to change phase from HCP to BCC, because it requires a restructuring of the lattice structure. Nonetheless, the resulting displacement is only marginally influenced by this fact. In the subboxes simulation, nearly all atoms change phase to BCC. In the Cauchy simulation, it is only the free center atoms that are able to change phase. Finally, the last transition is the transition from BCC to HCP. In the single hexahedron test case a small shear transformation is identified, that is not present in this degree in the horizontal coupling test cases. The single hexahedron again deforms perfectly and the length ratio is very close to theoretical predictions. The Cauchy coupling struggles with this transition. The transformation does not happen at all and the deformation is very non-homogeneous. Convergence is not archieved. In contrast, the subboxes coupling performs much better in this case. The BCC structure changes to HCP and the length ratio converges. Nonetheless, due to the different orientations of the HCP lattices in the subboxes, a few incompatibilities are created that result in a partly non-homogeneous lattice structure throughout the problem. The resulting length ratio converges to a value of ≈ 1.75 instead of 1.597. While this is still an error of 10%, it is a big improvement compared to the Cauchy solution.

8

Conclusions and outlook

8.1 Conclusions

The goal of this thesis was to develop a multiscale method that works in a phase transformation context in metals. As is explained in Chapter 5, existing methods are mostly not suitable to simulate phase transformation, because the topology is very constrained in the coarse scale domain and in the interface area (if present). In order to overcome these challenges, a new method has been developed. In Section 1.2 four steps were identified that are necessary to complete this task. These are:

1. Phase transformation in molecular dynamics: identification of molecular dynamics potentials for iron and titanium that are suitable for phase transformation.

2. Phase transformation in finite elements: development of a hierarchic concept for coupling finite elements and molecular dynamics similar to the FE²-concept.

3. Phase transformation at the interface: development of a partitioned-domain concept for coupling finite elements and molecular dynamics that enables phase transformation at the interface.

4. Validation of the concept in a number of test cases.

Concerning step 1, two potentials were identified that enable phase transformation in the molecular dynamics simulation. Using the theories mentioned in Chapter 2, the potential by MEYER AND ENTEL (1998) for iron was reconstructed from references. Its implementation is in good agreement with literature values (see Table 3.5) and it was demonstrated to be able to model phase transformation between BCC and FCC. In addition, another potential by MENDELEV ET AL. (2016) for titanium was used for the simulation of phase change between HCP and BCC. The lattice constants are in agreement with the reference (see Table 3.6) and the plots of the potential functions

also agree with the publication by Mendelev et al. Phase change is demonstrated in Chapter 7.

Concerning step 2, a hierarchical method using finite elements and molecular dynamics was derived from the FE^2-concept by Feyel (2003) and described in Section 6.2. Using the theoretical explanations of finite element theory in Chapter 4, the internal nodal forces were modified to include a small molecular dynamics subproblem as material law. The implementation is similar to the work done by Ulz (2015), but also different regarding the solving of the balance equations. Ulz uses a nonlinear static approach, while in this work a non-linear dynamic approach is used. A damping matrix was introduced using stiffness proportional damping in order to minimize the thermal vibrations of the stress derived from molecular dynamics on the finite elements. In Chapter 7 it is shown, that the vertical coupling shows very good results with regard to phase transformation.

Concerning step 3, a partitioned-domain method – called horizontal coupling in this work – was introduced in Section 6.3 that is partially based on the AtC-method from Fish et al. (2007) with some modifications. A part of the atoms is fixed to the finite element movement. In contrast to the Cauchy coupling, where the atoms are moving according to the deformation gradient of the atoms, it is proposed to put the atoms into a box with periodic boundary conditions and link this box to the movement of the finite element. This box is limited in shape to a parallelepiped, so from the finite element nodal positions a good-fit parallelepiped is calculated as explained in Section 6.3.4. This has a number of advantages compared to the Cauchy coupling. The coupling atoms have internal degrees of freedom, enabling them to change phase. The results of this method are presented in Chapter 7 and most simulations deliver promising results.

Concerning step 4, in total 4 multiscale test cases were simulated in Chapter 7. These are a tensile test case, a bending test case, a test case with phase transformation in a single hexahedron using vertical coupling only and a test case using the combined hierarchic-partitioned-domain method described in Section 6. The tensile test case in Section 7.2 shows good results, with only the Cauchy coupling showing a slightly off error compared to the molecular dynamics solution. In the bending test case in Section 7.3, the results are more mixed. In general, all methods converge to a solution, showing that the coupling is stable and contact between atoms and finite elements is not lost. However, the displacement results differ by around 35% compared to the molecular dynamics solution with the highest beam tip displacement. Using vertical coupling with finite elements only, the coupling is, in general, stiffer than the partitioned-domain method. However, a number of effects play an important role and even in beam theory the results differ with different finite element formulations and anti-locking formulations. For more details, see Section 7.3 and the summary in Section 7.6. The phase transformations are

investigated for a single hexahedron element using the vertical coupling only in Section 7.4 and a combined test case in Section 7.5. For all transitions, BCC to FCC, FCC to BCC, HCP to BCC and BCC to HCP, the vertical coupling delivers a very good result, as is seen in Figure 7.36. In the combined simulation test case, the results are also promising. For the first phase transformation from BCC to FCC, both Cauchy coupling and the newly proposed subboxes coupling deliver good results. The Cauchy coupling is able to manage the BCC to FCC transition because only a scaling of the axes is involved. For this reason, the Cauchy coupling also performs very well in the FCC to BCC transition. The simulations using the subboxes coupling are also converging, but require a longer simulation time, because convergence is slower. In the HCP to BCC transition, the Cauchy coupling manages the deformation due to the vertical coupling in the finite elements, but the bound atoms do not change phase, which has only a small influence on the overall deformation behavior. The subboxes solution is marginally better. In the BCC to HCP transition however, the transition completely fails with the Cauchy type coupling and the subboxes coupling does not show a perfect, but much better result. It can, therefore, be concluded that the subboxes coupling, in general, delivers a better result than using a Cauchy type coupling in multiscale phase transformation simulation.

8.2 Outlook

Based on the work in this thesis, many future projects can be imagined. First of all, it might be desirable to find a molecular dynamics potential that can better describe phase transformation, for example without resorting to a force boundary condition in order to initiate the phase transformation. In order to achieve this, it might be necessary to change from the embedded atom method (EAM) to the modified embedded atom method (MEAM). This method does also include angular relationships between atoms and does provide a better representation of the material. As far as the vertical coupling is concerned, it is found in this thesis, that the computation of the MD subproblems is very time consuming and could be improved if a more simple finite element material law is derived from the (M)EAM potential, which also has the phase transformation characteristics, but does not require a full MD simulation. In that way, the vertical coupling would be no longer required or could be limited to areas, where it is undispensable.

When using the subboxes for the horizontal coupling, the free atoms at the interface to the finite elements receive kinetic energy from the atoms of the subboxes and are pushed out of position. A possible solution to this problem could be that the free atoms only interact with the time-averaged position of the bound atoms. In this way, the effect of the vibrations could be reduced. The number of steps used to average the positions

could be an interesting research topic. It might also be possible to include adaptivity into the method. Work on adaptivity as already performed at IBB in the past (Sorg (2014)).

Looking further ahead, it might be interesting to look at polycrystals and lattice defects in the atomistic domain, so that a true simulation of the formation of e.g. austenite might be realized. If combined with an adaptivity algorithm, it might be possible to simulate more challenging problems.

Bibliography

Amelang, J., Venturini, G., and Kochmann, D. (2015). Summation rules for a fully-nonlocal energy-based quasicontinuum method. *Journal of the Mechanics and Physics of Solids*, 82.

Argyris, J. (1960). *Energy Theorems and Structural Analysis.* Butterworth,.

Arndt, M. and Luskin, M. (2008). Error estimation and atomistic-continuum adaptivity for the quasicontinuum approximation of a frenkel–kontorova model. *Multiscale Modeling & Simulation*, 7(1):147–170.

Badia, S., Bochev, P., Lehoucq, R., Parks, M., Fish, J., Nuggehally, M. A., and Gunzburger, M. (2007). A force-based blending model foratomistic-to-continuum coupling. *International Journal for Multiscale Computational Engineering*, 5(5):387–406.

Bauman, P. T., Dhia, H. B., Elkhodja, N., Oden, J. T., and Prudhomme, S. (2008). On the application of the arlequin method to the coupling of particle and continuum models. *Computational Mechanics*, 42(4):511–530.

Belytschko, T., Liu, W., and Moran, B. (2000). *Nonlinear finite elements for continua and structures.* Wiley.

Born, M. (1923). *Atomtheorie des festen Zustandes (Dynamik der Kristallgitter).* Fortschritte der mathematischen Wissenschaften in Monographien. B.G. Teubner.

Born, M. and Huang, K. (1954). *Dynamical theory of crystal lattices.* International series of monographs on physics. Clarendon Press.

Cancès, E., Castella, F., Chartier, P., Faou, E., Le Bris, C., Legoll, F., and Turinici, G. (2004). High-order averaging schemes with error bounds for thermodynamical properties calculations by molecular dynamics simulations. *The Journal of Chemical Physics*, 121(21):10346–10355.

Cauchy, A.-L. (1828a). *De la pression ou tension dans un système de points matériels*, pages 213–236. Bure frères, libraires du Roi et de la Bibliothéque du Roi, Paris, France.

Cauchy, A.-L. (1828b). *Sur l'équilibre et le mouvement d'un système de points matériels sollicités par des forces d'attraction ou de répulsion mutuelle*, pages 188–212. Bure frères, libraires du Roi et de la Bibliothéque du Roi, Paris, France.

Clausius, R. (1870). Xvi. on a mechanical theorem applicable to heat. *The London, Edinburgh, and Dublin Philosophical Magazine and Journal of Science*, 40(265):122–127.

Clementi, E. and Roetti, C. (1974). Roothaan-hartree-fock atomic wavefunctions: Basis functions and their coefficients for ground and certain excited states of neutral and ionized atoms, z≤54. *Atomic Data and Nuclear Data Tables*, 14(3):177 – 478.

Daw, M. S. and Baskes, M. I. (1984). Embedded-atom method: Derivation and application to impurities, surfaces, and other defects in metals. *Phys. Rev. B*, 29:6443–6453.

Dupuy, L. M., Tadmor, E. B., Miller, R. E., and Phillips, R. (2005). Finite-temperature quasicontinuum: Molecular dynamics without all the atoms. *Phys. Rev. Lett.*, 95:060202.

E, W. and Engquist, B. (2003). The heterogeneous multiscale methods. *Commun. Math. Sci.*, 1(1):87–132.

Edgar, B. (1924). The nature of martensite. *Trans. Amer. Inst. Min. Metall. Eng.*, 70:25.

Eidel, B. and Stukowski, A. (2009). A variational formulation of the quasicontinuum method based on energy sampling in clusters. *Journal of the Mechanics and Physics of Solids*, 57(1):87 – 108.

Evans, D. J. and Holian, B. L. (1985). The nose–hoover thermostat. *The Journal of Chemical Physics*, 83(8):4069–4074.

Faken, D. and Jónsson, H. (1994). Systematic analysis of local atomic structure combined with 3d computer graphics. *Computational Materials Science*, 2(2):279 – 286.

Feyel, F. (2003). A multilevel finite element method (fe2) to describe the response of highly non-linear structures using generalized continua. *Computer Methods in Applied Mechanics and Engineering*, 192(28):3233 – 3244. Multiscale Computational Mechanics for Materials and Structures.

Fish, J., Nuggehally, M. A., Shephard, M. S., Picu, C. R., Badia, S., Parks, M. L., and Gunzburger, M. (2007). Concurrent atc coupling based on a blend of the continuum stress and the atomistic force. *Computer Methods in Applied Mechanics and Engineering*, 196(45):4548 – 4560.

Fock, V. (1930). Näherungsmethode zur lösung des quantenmechanischen mehrkörperproblems. *Zeitschrift für Physik*, 61(1):126–148.

Geers, M., Kouznetsova, V., and Brekelmans, W. (2010). Multi-scale computational homogenization: Trends and challenges. *Journal of Computational and Applied Mathematics*, 234(7):2175 – 2182. Fourth International Conference on Advanced COmputational Methods in ENgineering (ACOMEN 2008).

Govindjee, S. and Miehe, C. (2001). A multi-variant martensitic phase transformation model: formulation and numerical implementation. *Computer Methods in Applied Mechanics and Engineering*, 191(3):215 – 238.

Grabowski, W. W. and Smolarkiewicz, P. K. (2002). A multiscale anelastic model for meteorological research. *Mon. Weather Review*, 130(4):939–956.

Hartree, D. R. (1928). The wave mechanics of an atom with a non-coulomb central field. part i. theory and methods. *Mathematical Proceedings of the Cambridge Philosophical Society*, 24(1):89–110.

K. Datta, D., Catalin Picu, R., and S. Shephard, M. (2004). Composite grid atomistic continuum method: An adaptive approach to bridge continuum with atomistic analysis. *International Journal for Multiscale Computational Engineering - INT J MULTISCALE COMPUT ENG*, 2:401–420.

Knap, J. and Ortiz, M. (2001). An analysis of the quasicontinuum method. *Journal of the Mechanics and Physics of Solids*, 49(9):1899 – 1923. The JW Hutchinson and JR Rice 60th Anniversary Issue.

Kohlhoff, S., Gumbsch, P., and Fischmeister, H. F. (1991). Crack propagation in b.c.c. crystals studied with a combined finite-element and atomistic model. *Philosophical Magazine A*, 64(4):851–878.

Lu, Y. e. a. (2016). Dislocation "bubble-like-effect" and the ambient temperature superplastic elongation of body-centred cubic single crystalline molybdenum. *Sci. Rep.*, 6:22937.

Luan, B. Q., Hyun, S., Molinari, J. F., Bernstein, N., and Robbins, M. O. (2006). Multiscale modeling of two-dimensional contacts. *Phys. Rev. E*, 74:046710.

M. J. Turner, R. W. Clough, H. C. M. and Topp, L. C. (1956). Stiffness and deflection analysis of complex structures. *J. Aeronaut. Sci.*, 23(9):805 – 823, 854.

Mendelev, M. I., Han, S., Srolovitz, D. J., Ackland, G. J., Sun, D. Y., and Asta, M. (2003). Development of new interatomic potentials appropriate for crystalline and liquid iron. *Philosophical Magazine*, 83(35):3977–3994.

Mendelev, M. I., Underwood, T. L., and Ackland, G. J. (2016). Development of an interatomic potential for the simulation of defects, plasticity, and phase transformations in titanium. *The Journal of Chemical Physics*, 145(15):154102.

Meyer, R. and Entel, P. (1998). Martensite-austenite transition and phonon dispersion curves of $fe_{1-x}ni_x$ studied by molecular-dynamics simulations. *Physical Review B*, 57:5140–5147.

Parrinello, M. and Rahman, A. (1981). Polymorphic transitions in single crystals: A new molecular dynamics method. *Journal of Applied Physics*, 52(12):7182–7190.

Phillips, R. (2001). *Crystals, Defects and Microstructures: Modeling Across Scales.* Cambridge University Press.

Plimpton, S. (1995). Fast parallel algorithms for short-range molecular dynamics. *Journal of Computational Physics*, 117(1):1 – 19.

Qian, D., Wagner, G. J., and Liu, W. K. (2004). A multiscale projection method for the analysis of carbon nanotubes. *Computer Methods in Applied Mechanics and Engineering*, 193(17):1603 – 1632. Multiple Scale Methods for Nanoscale Mechanics and Materials.

Ray, J. R. and Rahman, A. (1985). Statistical ensembles and molecular dynamics studies of anisotropic solids. ii. *The Journal of Chemical Physics*, 82(9):4243–4247.

Rayleigh, L. (1877). *Theory of Sound (two volumes).* Dover Publications, New York, 1945 re-issue.

Roth, J., Stadler, J., Brunelli, M., Bunz, D., Gähler, F., Hahn, J., Hohl, M., Horn, C., Kaiser, J., Mikulla, R., Schaaf, G., Stelzer, J., and Trebin, H.-R. (2000). Imd — a massively parallel molecular dynamics package for classical simulations in condensed matter physics. In Krause, E. and Jäger, W., editors, *High Performance Computing in Science and Engineering '99*, pages 72–81, Berlin, Heidelberg. Springer Berlin Heidelberg.

Schmauder, S. and Schäfer, I. (2016). *Multiscale Materials Modeling - Approaches to Full Multiscaling.* Walter de Gruyter GmbH, Berlin/Boston.

Schrödinger, E. (1926). An undulatory theory of the mechanics of atoms and molecules. *Phys. Rev.*, 28:1049–1070.

Shilkrot, L., Miller, R. E., and Curtin, W. A. (2004). Multiscale plasticity modeling: coupled atomistics and discrete dislocation mechanics. *Journal of the Mechanics and Physics of Solids*, 52(4):755 – 787.

Shilkrot, L. E., Miller, R. E., and Curtin, W. A. (2002). Coupled atomistic and discrete dislocation plasticity. *Phys. Rev. Lett.*, 89:025501.

Sorg, A. (2014). *Adaptive diskret-kontinuierliche Modellierung von Materialien mit Mikrostruktur*. PhD thesis, University of Stuttgart.

Subramaniyan, A. K. and Sun, C. (2008). Continuum interpretation of virial stress in molecular simulations. *International Journal of Solids and Structures*, 45(14):4340 – 4346.

Tadmor, E. and Miller, R. (2011). *Modeling Materials: Continuum, Atomistic and Multiscale Techniques*. Cambridge University Press, Cambridge.

Tadmor, E., Phillips, R., and Ortiz, M. (2000). Hierarchical modeling in the mechanics of materials. *International Journal of Solids and Structures*, 37:379–389.

Tadmor, E. B. and Miller, R. E. (2017). Benchmarking, validation and reproducibility of concurrent multiscale methods are still needed. *Modelling and Simulation in Materials Science and Engineering*, 25(7):071001.

Tadmor, E. B., Ortiz, M., and Phillips, R. (1996). Quasicontinuum analysis of defects in solids. *Philosophical Magazine A*, 73(6):1529–1563.

Ulz, M. H. (2015). Coupling the finite element method and molecular dynamics in the framework of the heterogeneous multiscale method for quasi-static isothermal problems. *Journal of Mechanics Physics of Solids*, 74:1–18.

Verlet, L. (1967). Computer "experiments" on classical fluids. i. thermodynamical properties of lennard-jones molecules. *Phys. Rev.*, 159:98–103.

Wagner, G., Jones, R., Templeton, J., and Parks, M. (2008). An atomistic-to-continuum coupling method for heat transfer in solids. *Computer Methods in Applied Mechanics and Engineering*, 197(41):3351 – 3365. Recent Advances in Computational Study of Nanostructures.

Wagner, G. J. and Liu, W. K. (2003). Coupling of atomistic and continuum simulations using a bridging scale decomposition. *Journal of Computational Physics*, 190(1):249 – 274.

Wang, B. and Urbassek, H. M. (2013). Phase transitions in an Fe system containing a bcc/fcc phase boundary: An atomistic study. *Physical Review B*, 87(10):104108.

Xiao, S. and Belytschko, T. (2004). A bridging domain method for coupling continua with molecular dynamics. *Computer Methods in Applied Mechanics and Engineering*, 193(17):1645 – 1669. Multiple Scale Methods for Nanoscale Mechanics and Materials.

Zienkiewicz, O. C., Taylor, R. L., and Too, J. M. (1971). Reduced integration technique in general analysis of plates and shells. *International Journal for Numerical Methods in Engineering*, 3(2):275–290.

Curriculum vitae

Personal data:

Name:	Tobias Emanuel Willerding
Date of birth:	March 10, 1988
Place of birth:	Bonn-Bad Godesberg

School education:

08/1998 – 06/2007	Aloisiuskolleg, Bonn

University education:

10/2007 – 09/2008	Physics at the University of Bonn
10/2008 – 12/2013	Aerospace engineering at the University of Stuttgart
12/2013	Diploma degree in aerospace engineering
since 02/2014	PhD student at the Institute for Structural Mechanics, University of Stuttgart

Berichte des Instituts für Baustatik und Baudynamik der Universität Stuttgart

1 (1983) **P. Osterrieder:**
Traglastberechnung von räumlichen Stabwerken bei großen Verformungen mit finiten Elementen.

2 (1983) **T. A. Kompfner:**
Ein finites Elementmodell für die geometrisch und physikalisch nichtlineare Berechnung von Stahlbetonschalen.

3 (1983) **A. Diack:**
Beitrag zur Stabilität diskret längsversteifter Kreiszylinderschalen unter Axialdruck.

4 (1984) **A. Burmeister, F.W. Bornscheuer, E. Ramm:**
Traglasten von Kugelbehältern mit Stutzen und Formabweichungen unter Innendruck und Stützenlängskraft.

5 (1985) **H. Stegmüller:**
Grenzlastberechnungen flüssigkeitsgefüllter Schalen mit „degenerierten" Schalenelementen.

6 (1987) **A. Burmeister:**
Dynamische Stabilität nach der Methode der finiten Elemente mit Anwendungen auf Kugelschalen.

7 (1987) **G. Kammler:**
Ein finites Elementmodell zur Berechnung von Trägern und Stützen mit offenem, dünnwandigem Querschnitt unter Berücksichtigung der Interaktion zwischen globalem und lokalem Versagen.

8 (1988) **A. Matzenmiller:**
Ein rationales Lösungskonzept für geometrisch und physikalisch nichtlineare Strukturberechnungen.

9 (1989) **D. Tao:**
Die Technik der reduzierten Basis bei nichtlinearen finiten Element-Berechnungen.

10 (1989) K. M. Weimar:
Ein nichtlineares Balkenelement mit Anwendung als Längssteifen axialbelasteter Kreiszylinder.

11 (1990) K.-U. Bletzinger:
Formoptimierung von Flächentragwerken.

12 (1990) S. Kimmich:
Strukturoptimierung und Sensibilitätsanalyse mit finiten Elementen.

13 (1991) U. Andelfinger:
Untersuchungen zur Zuverlässigkeit hybrid-gemischter Finiter Elemente für Flächentragwerke.

14 (1992) N. Büchter:
Zusammenführung von Degenerationskonzept und Schalentheorie bei endlichen Rotationen.

15 (1992) T. J. Hofmann:
Beitrag zur verfeinerten Balkentheorie.

16 (1994) D. de Mesquita Roehl:
Zur Berechnung von großen elastoplastischen Deformationen bei Flächentragwerken und Kontinua.

17 (1994) R. Reitinger:
Stabilität und Optimierung imperfektionsempfindlicher Tragwerke.

18 (1995) R. L. M. Suanno:
Ein dreidimensionales Simulationsmodell für Stahlbeton mit Plastizität und Schädigung.

19 (1995) M. Braun:
Nichtlineare Analysen von geschichteten, elastischen Flächentragwerken.

20 (1996) N. Rehle:
Adaptive Finite Element Verfahren bei der Analyse von Flächentragwerken.

21 **(1996)** **C. Haußer:**
Effiziente Dreieckselemente für Flächentragwerke.

22 **(1996)** **D. Kuhl:**
Stabile Zeitintegrationsalgorithmen in der nichtlinearen Elastodynamik dünnwandiger Tragwerke.

23 **(1998)** **H. Schmidts:**
Zur effizienten Modellierung und Analyse von Hochhaustragwerken.

24 **(1998)** **H. Wang:**
Interaktion des lokalen und globalen Stabilitätsverhaltens dünnwandiger Stäbe.

25 **(1998)** **K. Maute:**
Topologie- und Formoptimierung von dünnwandigen Tragwerken.

26 **(1998)** **B. Maurer:**
Karl Culmann und die graphische Statik.

27 **(1998)** **F. Cirak:**
Adaptive Finite-Element-Methoden bei der nichtlinearen Analyse von Flächentragwerken.

28 **(1998)** **M. Trautz:**
Zur Entwicklung von Form und Struktur historischer Gewölbe aus der Sicht der Statik.

29 **(1999)** **H. Menrath:**
Numerische Simulation des nichtlinearen Tragverhaltens von Stahlverbundträgern.

30 **(1999)** **M. Bischoff:**
Theorie und Numerik einer dreidimensionalen Schalenformulierung.

31 **(1999)** **W. A. Wall:**
Fluid-Struktur-Interaktion mit stabilisierten Finiten Elementen.

32 **(2000)** **E. Kuhl:**
Numerische Modelle für kohäsive Reibungsmaterialien.

33 **(2001)** **A. Maute:**
Fehlerkontrolle bei Finite-Element-Methoden in der linearen Struktur-
dynamik.

34 **(2001)** **S. Schwarz:**
Sensitivitätsanalyse und Optimierung bei nichtlinearem Strukturver-
halten.

35 **(2001)** **A. Haufe:**
Dreidimensionale Simulation bewehrter Flächentragwerke aus Beton
mit der Plastizitätstheorie.

36 **(2001)** **D. P. Mok:**
Partitionierte Lösungsansätze in der Strukturdynamik und der Fluid-
Struktur-Interaktion.

37 **(2002)** **H. Steeb:**
Fehlerschätzer für FE-Berechnungen bei entfestigenden Materialien.

38 **(2002)** **K. Krausz:**
Tragverhalten gemauerter Tonnengewölbe mit Stichkappen.

39 **(2002)** **M. Hörmann:**
Nichtlineare Versagensanalyse von Faserverbundstrukturen.

40 **(2003)** **V. Gravemeier:**
The Variational Multiscale Method for Laminar and Turbulent Incom-
pressible Flow.

41 **(2004)** **R. Kemmler:**
Stabilität und große Verschiebungen in der Topologie- und Form-
optimierung.

42 **(2004)** **G. A. D'Addetta:**
Discrete Models for Cohesive Frictional Materials.

43 **(2004)** **M. Gee:**
Effiziente Lösungsstrategien in der nichtlinearen Schalenmechanik.

44 (2004) T. Erhart:
Strategien zur numerischen Modellierung transienter Impaktvorgänge bei nichtlinearem Materialverhalten.

45 (2005) M. Leukart:
Kombinierte anisotrope Schädigung und Plastizität bei kohäsiven Reibungsmaterialien.

46 (2006) F. Huber:
Nichtlineare dreidimensionale Modellierung von Beton- und Stahlbetontragwerken.

47 (2007) A. Lipka:
Verbesserter Materialeinsatz innovativer Werkstoffe durch die Topologieoptimierung.

48 (2007) A. S. Hund:
Hierarchische Mehrskalenmodellierung des Versagens von Werkstoffen mit Mikrostruktur.

49 (2007) S. Hartmann:
Kontaktanalyse dünnwandiger Strukturen bei großen Deformationen.

50 (2007) T. M. Hettich:
Diskontinuierliche Modellierung zur Versagensanalyse von Verbundmaterialien.

51 (2007) C. Förster:
Robust methods for fluid-structure interaction with stabilised finite elements.

52 (2009) M. von Scheven:
Effiziente Algorithmen für die Fluid-Struktur-Wechselwirkung.

53 (2010) J. Kato:
Material Optimization for Fiber Reinforced Composites applying a Damage Formulation.

54 **(2010)** **C. F. Hilchenbach:**
Optimierung von Mehrphasenstrukturen mit lokalem Schädigungsverhalten.

55 **(2011)** **I. Bruss:**
Dreidimensionale Schädigungsmodellierung heterogener Materialien.

56 **(2012)** **B. J. Schneider:**
Polygonale diskrete Elemente zur Modellierung heterogener Materialien.

57 **(2012)** **R. Etlender:**
Modellierung und Simulation der Wellenausbreitung in flexiblen hydraulischen Leitungen.

58 **(2012)** **T. Cichosz:**
Stabile und konsistente Kontaktmodellierung in Raum und Zeit.

59 **(2013)** **R. Echter:**
Isogeometric analysis of shells.

60 **(2013)** **A. Tkachuk:**
Variational methods for consistent singular and scaled mass matrices.

61 **(2013)** **J. Irslinger:**
Mechanische Grundlagen und Numerik dreidimensionaler Schalenelemente.

62 **(2014)** **T. E. Pohl:**
Adaptive Methoden zur Pfadverfolgung bei Entfestigung.

63 **(2014)** **A. Sorg:**
Adaptive diskret-kontinuierliche Modellierung von Materialien mit Mikrostruktur.

64 **(2015)** **M. E. Matzen:**
Isogeometrische Modellierung und Diskretisierung von Kontaktproblemen.

65 (2016) V. M. Effinger:
Finite nichtlinear viskoelastische Modellierung offenzelliger Polymer-schäume.

66 (2017) C. Wilking:
Effiziente Integration und verbesserte Kontaktspannungen für duale Mortar-Formulierungen.

67 (2018) B. Oesterle:
Intrinsisch lockingfreie Schalenformulierungen.

68 (2018) F. Neukamm:
Lokalisierung und Versagen von Blechstrukturen.

69 (2019) A.-K. Schäuble:
Variationally consistent inertia templates for speed-up and customization in explicit dynamics.

Tobias Willerding

This thesis is about multiscale simulation of phase transformation in metals. Multiscale simulation is the simultaneous use of two or more models in order to have phenomena of different length or time scale in one simulation. Phase transformation between different lattice structures plays an important role in the formation of metals, e.g. iron or titanium. It is, therefore, of interest to simulate phase transformation in a multiscale context. In this thesis, a multiscale method for the simulation of phase transformation in metals is developed. Continuum mechanics, represented by the finite element method, is coupled with atomistics, represented by molecular dynamics.

The goal is to simulate phase transformation in metals between different lattice structures such as body-centered cubic, face-centered cubic and hexagonal close-packed structure. As phase transformation requires an internal restructuring of the molecular structure, traditional multiscale methods cannot be used as these require fixed coupling at the interface between coarse scale and fine scale and very often also in the coarse scale by using the Cauchy(-Born) rule.

In order to overcome these problems, a combined hierarchic-partitioned-domain method is proposed that consists of two parts. On the finite element level, a hierarchic method based on the FE^2-method is used with molecular dynamics simulations as subproblems, one subproblem at each Gauss integration point. The partitioned-domain part of the method consists of dividing the domain into two parts: a molecular dynamics part and a finite element part. A part of the atoms are put into a box with the shape of a parallelepiped and with periodic boundary conditions. This box is linked to the movement of the finite element nodes.